Peculiar Velocities and Large Scale Flows as Probes of Gravity, ΛCDM and the Growth of Structure over Cosmic Time.

by

Stephen Turnbull

A thesis
presented to the University of Waterloo
in fulfillment of the
thesis requirement for the degree of
Master of Science
in
Physics

Waterloo, Ontario, Canada, 2012

© Stephen Turnbull 2012

I hereby declare that I am the sole author of this thesis. This is a true copy of the thesis, including any required final revisions, as accepted by my examiners.

I understand that my thesis may be made electronically available to the public.

Chapters 2 and 3 are excerpts and early version of collaboratively written papers.

Abstract

Peculiar velocities are possibly the most powerful probes of very large-scale mass density fluctuations in the nearby Universe. When coupled with a density field they also can constrain the growth factor of the universe by measuring the proportionality constant between observed velocities and linear theory predicted velocities. In this thesis, I measure a bulk flow of SN within 20,000 km s^{-1} of 197 $\pm$ 56 km s^{-1} in direction $l = 295^\circ \pm 16^\circ$, $b = 11^\circ \pm 14^\circ$, which is consistent with predictions of ΛCDM for large scale mass density fluctuations. Using the IRAS Point Source Catalog Redshift survey (PSCz) galaxy density field and the SNe peculiar velocities I calculated $\Omega_m^{0.55}\sigma_{8,\mathrm{lin}}$ to be 0.40 $\pm$ 0.07 which is in excellent agreement with the results of WMAP7 [1]: $\Omega_m^{0.55}\sigma_{8,\mathrm{lin}} = 0.39 \pm 0.04$. By combining my measured value of β with results from other studies, I measure the growth factor γ to be $= 0.621 \pm 0.08$ which is consistent with ΛCDM's prediction of 0.55. I conclude by exploring some of the systematic errors that could have affected my measurements of β. I find that when β is measured using a reconstruction method the result can be underestimated by between 7 and 15 %.

Acknowledgements

I wish to give thanks to Mike Hudson for clarity of vision; my supervisory committee, Niayesh Afshordi and Brian McNamara, for compelling me to keep on track; Guilhem Lavaux for his simulations and expertise at pointing out inconsistencies and likely bugs; and my family and friends for keeping me sane (ish).

I acknowledge the financial support of NSERC and OGS.

I extend my thanks for copy editing to Caroline J. Karubin, Morgan McCormic, Mike Hudson and Dana Kayes.

Dedication

This text is dedicated to the bureaucracies of formal learning, to which it owes its existence, and to the few brave souls who shall ever read it.

Table of Contents

List of Tables

List of Figures

Chapter 1

Introduction to Cosmic Flows

1.1 Testing Gravity and ΛCDM with Peculiar Velocities and the Growth of Structure

The universe is not perfectly uniform. Some regions are packed densely with planets, stars, galaxies and black holes and others so sparse that volumes the size of breadboxes can be reasonably said to contain no atoms at all. This difference in density is driven by and drives gravitational collapse. Regions with even the slightest advantage in density pull matter from less dense regions around them. This added mass then compounds the density differences and thus accelerates the rate at which mass drains out of the voids into the denser regions. On small scales (atoms, people, planets, and galaxies) velocities of objects can be affected by countless factors and many conflicting forces, while on large scales only two forces are thought to be significant: the expansion of the universe and gravitational collapse towards massive structures. The understanding and the models of the universe allow for predictions of what these velocities should be at these larger and simpler scales. The study provides the opportunity to test this understanding and these models by measuring large scale velocities and comparing the predictions to observations.

Given that the universe is isotropic and is thought to be homogeneous on the largest scales, the average velocity of sampled volumes on the largest scales should be 0. However, the root mean square (rms) of the velocity distribution need not be be zero, but it should trend towards zero for larger volumes. In ΛCDM, one of the things that can be can predicted for a volume of a given shape is the rms that would be observed if one sampled the average velocity of many such volumes independently. Given a defined volume ΛCDM can be used to calculate the probability that all objects contained within that volume would have a given mean velocity. Conversely, if the mean velocity of objects in a given volume is known, then ΛCDM can be tested by calculating the associated probability of finding a volume moving at that minimum velocity. If the resulting probability were very low, that would suggest some component of the ΛCDM models could be in conflict with reality.

The tests of gravity and the growth of structure are slightly more complicated. The part of large scale velocity that comes from gravitational collapse depends not only on gravity, but also on the differences between the densities of the regions involved and how long those differences have been established. A very strong contrast in density between regions would establish the same resulting velocity considerably faster than a smaller contrast would. This ambiguity between 'slow' and 'quickly growing' contrasts and velocities cannot be resolved easily by looking at the contrast and velocities at one snapshot in time. Instead, the change in the relationship between large scale velocities density contrasts over cosmic time must be studied. If gravity where to differ at large scales from the relationship known at smaller scales, then this it could be revealed by the study of the growth of structure and the change in this velocity-density contrast relation.

1.2 Large Scale Structure (LSS) Definition

While the universe is thought to be close to uniform at the very largest scales, it certainly is not uniform on the scale of people, planes and planets. Between these two extremes is

Table 1.1: Features of large scale structure.

Structure name	mass range ($M_\odot$)	size range (Mpc)	Additional Notes
Galaxies	$10^{12} - 10^{13}$	$10^{-3} - 10^{-1}$	lower limit for LSS
Groups	$\simeq 10^{13}$	$\ll 1$	Contain up to ∼50 galaxies
Clusters	$10^{14} - 10^{15}$	$1- \ll 10$	Between ∼50 and ∼1000 galaxies
Super-clusters	up to 10^{15}	$10 - 50$	Not gravitationally bound

a large host of structurally self-similar features, such as galaxies, galaxy groups, clusters, Super-clusters and voids. The units most frequently used in the discussion of Large Scale Structure (LSS) are the solar mass (1 $M_\odot$ being the mass of the Sun, $\simeq 2 \times 10^{30} kg$) and the Megaparsec (1 Mpc $\simeq 3 \times 10^{22}$ meters). Velocities are measured in km/s. Table 1.1 gives the names, mass ranges, and sizes for an assortment of structures which populate the universe between the scales of planes and people, and the universe as a whole. In addition to the listed structures, are: 'filaments' which extend between super-clusters and range between 50 and 110 Mpc long, 'sheets' which extend between 'filaments', and 'voids' which can extend between 5.8 and 16 h^{-1} Mpc in radius[1].

1.2.1 ΛCDM, Matter, and Gravitational Collapse

The standard model of Cosmology today is the ΛCDM cosmological model. According to ΛCDM the universe is populated with: regular matter and radiation, which can be

[1]Where a void is defined as a region containing no halos with masses larger than of 5×10^{12} solar masses [6]. Note: the size of a 'typical void' depends on the threshold mass of halos that a void is defined to contain no halos larger than that limit. [6] quote void sizes for different halo mass thresholds, I report at 5×10^{12}, both because it is close to the middle or the range of masses which I worked with in this thesis, and simultaneously because that is the in the range of the typical masses of the tracers used in observations.

seen; dark matter and dark energy, which can be only detected via their effects on matter and radiation. While there are many interesting and complicated questions and interplays between the features of the model in general, the scope of relevant features decreases dramatically when one focuses on large scale velocities.

It has been observed that the visible matter in the universe is not uniform, and the degree of this contrast between high and low density regions can be measured. The matter which can be seen is not all the matter that exists. Measurements of virial theorem [7],the power spectrum [8], galactic rotation curves [9–12], strong and weak lensing [13, 14] amongst others clearly indicate that some additional matter, i.e. 'dark matter', exists and that there is more of it then visible matter.

For the purposes of this thesis I will make the simplifying assumption that fluctuations of matter map to fluctuations of observables such as galaxies in a linear relationship ($\delta_{\rm tr} = b_{\rm tr}\delta_{\rm m}$ where $\delta_{\rm m}$ is the density perturbations of matter, $\delta_{\rm tr}$ is the density perturbations of given observable tracer such as galaxies, and $b_{\rm tr}$ assumed linear bias between the two)[15]. It is important to note that this is a relationship between the fluctuations (or deviations from uniformity) as measured by a given tracer and the fluctuations as measured in all density. It is expected that this relationship would break down where either $\delta_{\rm tr}$ or $\delta_{\rm m}$ approach 1 or -1, and the relationship is expected to be more accurate at larger scales because of that.

For the purposes of large scale flows, the most important feature of dark matter is that it gravitates in the same way as regular matter. The remainder of the universe is filled with a substance which is simply called 'dark energy'. This 'dark energy' causes the universe to expand at an increasingly rapid rate [16], but since the observed expansion is consistent with uniform expansion, its effect on velocity is well understood. Any more complicated effects of dark energy are beyond the scope of this thesis.

Perturbation Theory

For the study of large scale velocities the sensitivity to physics, relevant in this thesis, comes in the interplay between the measurable fluctuations in the density contrast and the velocities which result from gravitational collapse from low density regions into high density regions. First order (linear) perturbation theory gives a relationship between velocity and density. A full treatment of perturbation theory for cosmology is outside of the scope of this investigation; for a more detailed review beyond the summary contained here refer to any intermediate or higher level cosmology text.

The zeroth order perfectly uniform density field has only trivial expanding and contracting velocity field solutions. Since I am examining the non - uniform behaviors I define a perturbation parameter $\delta_{\rm m}$ (which I write as δ where it can not easily be confused with $\delta_{\rm tr}$) as the perturbations about uniformity in matter density

$$\delta = (\rho - \bar{\rho})/\bar{\rho} \tag{1.1}$$

Taking the standard equations of force, gravitation, and conservation of matter in an expanding universe and expanding those equations to first order in δ, dropping the zeroth order terms, and substituting the results into each other leaves the equation

$$\frac{\partial^2\delta}{\partial t^2} + \frac{2\dot{a}}{a}\frac{\partial\delta}{\partial t} = 4\pi G\rho_o\delta \tag{1.2}$$

where $a(t)$ is the scale factor of the universe, G is the gravitational constant, and ρ_o is the uniform density being perturbed. The equation is a second order temporal differential equation with a drag term $\frac{2\dot{a}}{a}\frac{\partial\delta}{\partial t}$. However, only one of the two resulting solutions is relevant, given that the other one is a decaying mode and is therefore negligible. Substituting the growing mode solution ($D(t)$) back into the first order version of the continuity equation yields

$$\nabla \cdot v = -a\delta\frac{\dot{D}(t)}{D(t)} \tag{1.3}$$

where $\nabla \cdot v$ comes from the mass continuity equation $\frac{\partial\rho}{\partial t} + \nabla\cdot(\rho v) = 0$ as the scalar divergence of the velocity field. Simplifying $\frac{\dot{D(t)}}{D(t)}$ to $H_0\frac{d\ln D(t)}{d\ln a}$ and expressing it as $H_0 f$

where

$$f = \frac{d \ln D(t)}{d \ln a} \simeq \Omega_m^{\gamma} \tag{1.4}$$

where the approximation $f \simeq \Omega_m^{\gamma}$ comes from [17] and is valid for flat ΛCDM models, in such models $\gamma = 0.55$.

Re-inspecting 1.3, it is apparent that this is a divergence of a vector field driven by a scaler field, which is perfectly analogous to gravitational acceleration, i.e.

$$\mathbf{v}(\mathbf{r}) = \frac{H_0 f}{4\pi} \int_0^{\infty} \frac{\delta(\mathbf{r}')(\mathbf{r}' \hat{-} \mathbf{r}) d^3\mathbf{r}'}{(\mathbf{r}' - \mathbf{r})^2} \tag{1.5}$$

1.2.2 Peculiar Velocities and the Peculiar Velocity Field

In section 1.2.1, I dropped the zeroth order term which corresponds to the uniform expansion or contraction of the universe; which I will examine in slightly more detail in subsection 1.3.1. The first order solution corresponds to a means of transforming a known density field into a predicted velocity field. This predicted field is called the peculiar velocity field and represents the velocities relative to the 'co-moving' frame of reference of the zeroth order solution [2], hence 'peculiar' in this case meaning individual. The resulting velocity field is populated with flows that direct outwards from under-dense regions and towards over-dense regions, from which the name 'gravitation collapse' originates.

The resulting peculiar velocity field can being derived from a background density field which on the largest scales is thought to be very close to uniform, and must itself trend towards uniformity, specifically zero, as it is smoothed over larger and larger areas [3]. This provides one of the principle tests of ΛCDM which I present in Chapter 2; if the average peculiar velocity of a volume or the bulk flow of that volume is measured, then it can be compared to the analytically derived rms average velocities for volumes of that size and

[2] The frame is referred to as the co-moving frame because it is expanding with the universe

[3] The expectation velocity of would always be zero, but the rms around zero also tends to zero as you average over larger volumes in a manner which is predictable using ΛCDM

shape. Previous studies have explored testing ΛCDM with this approach, specifically this segment of my research is an extension of the works of [3].

1.2.3 Sensitivity to Cosmological Parameters

The real $\delta_{\rm m}$ is unmeasurable. Only $\delta_{\rm tr}$, the density perturbations of some tracer, which will be biased as discussed in 1.2.1, can be measured. Given $\delta_{\rm tr} = b_{\rm tr}\delta_{\rm m}$ equation 1.5 becomes

$$\mathbf{v}(\mathbf{r}) = \frac{H_0 f}{b_{\rm tr} 4\pi} \int_0^\infty \frac{\delta_{\rm tr}(\mathbf{r}')(\mathbf{r}' - \mathbf{r}) d^3\mathbf{r}'}{|\mathbf{r}' - \mathbf{r}|^3} \tag{1.6}$$

$b_{\rm tr}$ is not necessarily compatible between experiments since it is dependent upon the tracer used, which can differ between surveys. To resolve this I extend the analysis one step further by noting that if the tracer density is linearly biased then a larger scale average of that density field will be similarly biased, i.e.

$$\sigma_{8,\rm tr} = b_{\rm tr}\sigma_8 \tag{1.7}$$

where σ_8 is the r.m.s. fluctuation of density in an 8 h^{-1} Mpc top hat sphere, which is one of the fundamental constants of cosmology; and $\sigma_{8,\rm tr}$ is similar for any given tracer used in the survey, which can be directly measured. Given that substitution I then define

$$\beta = \frac{f}{b} = \frac{f\sigma_8}{\sigma_{8,\rm tr}} = \frac{\Omega_m^\gamma \sigma_8}{\sigma_{8,\rm tr}} \tag{1.8}$$

β is thus a parameter composed of a degenerate coupling of three cosmological parameters Ω_m, γ and σ_8 and one measurable parameter from each respective survey. The three cosmological parameters can be measured in other surveys and with other techniques for comparisons.

1.3 Observables

1.3.1 Redshifts

In subsection 1.2.2, I introduced peculiar velocities and the peculiar velocity field. Unfortunately these full velocities are not directly observable for objects outside the Galaxy. The reason is that velocities that are transverse to the line of sight are much to small too cause detectable displacements even given thousands of years. Only the component of the velocity which is directly towards or away from an observer can be detected. This radial component of the velocity is detected by comparing the frequency of observed spectral lines to their rest-frame frequencies. If the object is receding from the observer, then the observed spectral lines will be Doppler shifted to redder frequencies (redshift) when compared to their rest frame frequencies (conversely, approaching motions result in shifts to bluer frequencies or blue-shifts). In addition, each object picks up a redshift or a radial velocity from the zeroth order term of the linear perturbation expansion, as explained in section 1.2.1. The universal expanding or contracting solution results in the Hubble law, $\mathbf{v} = H_0\mathbf{r}$. [4] The Hubble law is very useful because it allows for the distance to an object to be determined by simply measuring its redshift (its velocity) if that object has no radial peculiar velocity. The two sources of redshift combine when measuring the redshift of an object in the universe. The peculiar velocity signal mixes with the distance signal slightly obscuring both which results in

$$cz = H_0 r + v_{\rm pec} \tag{1.9}$$

where z is the redshift, c is the speed of light, thus cz is a distance measured in km s^{-1}, $H_0 r$ is the velocity induced by the expansion of the universe, and $v_{\rm pec}$ is the radial component (from the observer) of the real space velocity of the observed object. In order to break the degeneracy between Hubble distance and peculiar velocity, one needs to independently measure the distance to a given object. This is the subject of the next section.

[4] At very large distances H changes as one goes back before Λ domination and the law must be adjusted, but for this work the large distance effects can be neglected.

1.3.2 Distance Indicators

Given that distance cannot be determined from redshift alone other methods must be found. The current best alternatives are standard candles and standard rulers. The basic idea behind standard candles and rulers is more fully explained in [18], however in summary:

A standard candle gives off a known luminosity which in a flat universe would be spread uniformly over the surface of concentric spheres centred at the source. When observing a standard candle, or a standardized candle with a source luminosity that can be derived from some other feature, one need only measure the observed flux to derive the distance to the source, since the observed flux drops off as the square of the distance over modest distances. However, additional complications arise over cosmological distances where the travel time is sufficient that the universe has changed over the duration between emission and absorption. Specifically, as the universe expands: every photon contained within it is stretched, resulting in a loss of energy; and the distance between successive photons increases, further decreasing the observed flux. Finally if the universe is not completely flat, more or less of the flux will be directed to a distant observer. Both of first two complications contributed a factor of $\frac{1}{(1+z)}$ where z is the redshift to the observed standard candle to the observed flux and needs to be taken into account for modestly large z. In principle the universe could be closed, which would result in the light being diluted over a smaller volume in the real sphere than predicted in a flat universe, or conversely large volume than predicted if the cosmology were open. However, the universe is known to be quite flat and thus the third complication does not contribute significantly[8].

In contrast, a standard ruler is an object of known size. If the object is observed to extend a given angular separation, simple trigonometry can reveal its distance from the observer. As with the standard candle, complications can arise with cosmological distances. If the universe is not flat, again the curvature contributes. Similarly, if the universe has significantly expanded since emission, then the standard ruler took up a larger fraction of the whole sky at the time of emission. This complication contributes a factor of $1 + z$ which must be taken into account for distant sources.

Supernovae (SN)

Supernovae are amongst the largest explosive forces in the universe and they can be more luminous than their host galaxies. They occur when the central core of a star collapses catastrophically under its own gravitational attraction. This occurs when either a massive star expends the last of its fuel and cools until it can no longer support its mass, or when an otherwise stable, cooled, late life star accretes sufficient mass to undergo heavy element fusion, specifically carbon fusion.

This second cause of supernovae occur under very specific circumstances and thus have very self consistent luminosities. This type of supernovae is called a Type Ia supernova and it occurs in binary star systems where a white dwarf slowly strips gases and mass off of its companion until it reaches the Chandrasekhar mass limit of about 1.38 solar masses (see Fig 1.1). When this mass limit is reached, then the pressure provided by electrons of the stellar plasma can no longer compete with gravitation and the star collapses. The pressures and temperatures inside the star quickly mount and become high enough to fuse carbon within the core of the star. The rapid conversion of a large quantity of carbon releases a staggering quantity of energy, some of which gets converted into light. The mass limit at which this occurs is consistent from supernova to supernova, resulting in luminosities which are also consistent. Some variation does exist which is why Type Ia supernovae are referred to as 'standardizeable'. For this reason Type Ia supernovae are the primary distance indicators used in this thesis.

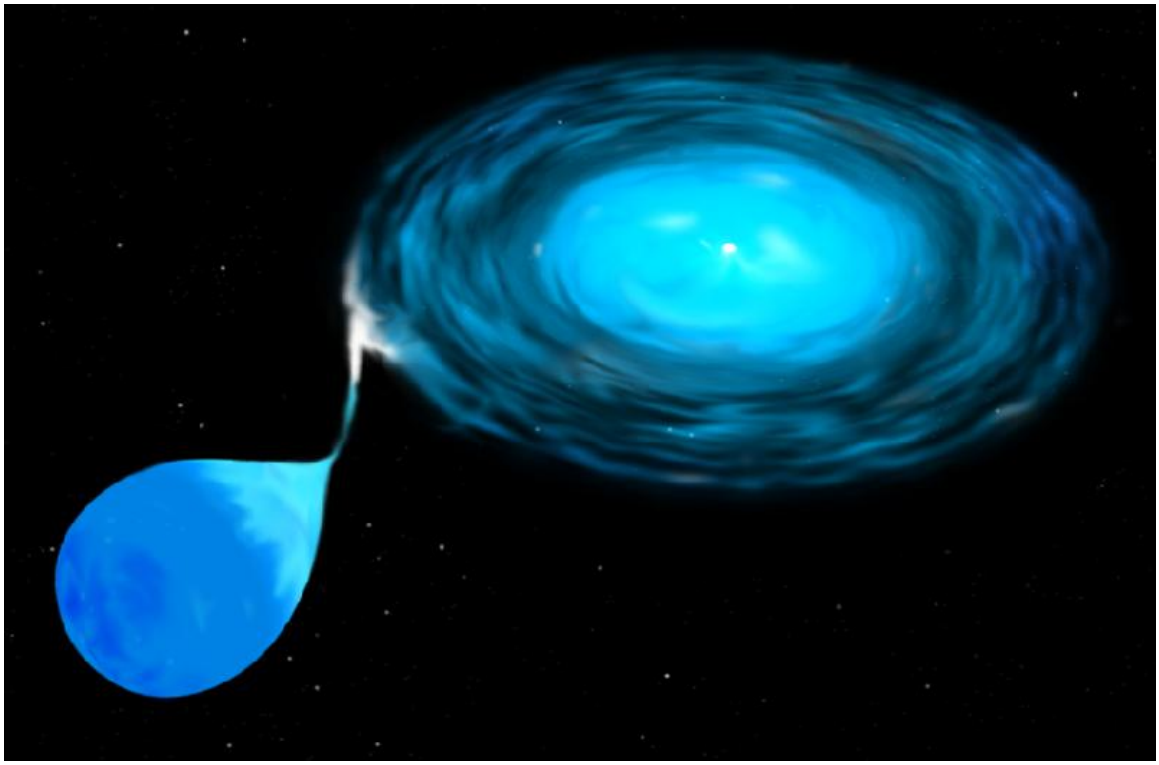

Figure 1.1: Artistic rendition of a binary star pair where gas is stripped from the one stellar body to its more compact partner. Image credit NASA sourced from Wikipedia

A full explanation of the standardization methods for Type Ia supernova would be beyond the scope of this thesis and a detailed methodology can be found in [19]. In general, Type Ia SN take ∼17 days to reach full intensity and reach an absolute luminosity of approximately -19.6 mag in the B band [20]. The primary goal in Type Ia SN fitting is to identify the time of maximum luminosity and the value of the maximum luminosity. One additional important feature is the 'decline rate' (the change in magnitude over 15 days) usually measured in the B band which correlates well with peak luminosity. The primary challenges of SN fitting is finding them in time and correcting for the host galaxy. Finding the SN before the peak luminosity requires frequently checking and rechecking of galaxies to look for sudden luminosity changes. Even if a SN is detected after peak luminosity, light

curve templates can be fit to the observed data to extract good estimates for the missed max flux, and such light curve fitting methods can be applied for data collected starting as late as one week after the peak [19]. The host galaxy continues to give off luminosity while the SN shines, thus it is important to have a baseline template to subtract off the observed luminosity. Also the host galaxy can contain dust which absorbs and re-radiates the SN's radiation causing frequency shifts to lower frequency bands. In many new SN observations, enough data is taken at a variety of wavelengths to estimate this host galaxy reddening. The effect of this host galaxy reddening is further explored in Section 2.3.

Tully Fisher and Fundamental plane

There are other distance indicators which work on galaxies such as, Tully Fisher for spirals, and fundamental plane for ellipticals. The resulting distance is less precisely determined for each sample than with SN, but significantly more samples can be made without waiting for hundreds of years for a sufficient number density of local SN to occur.

The Tully Fisher relation exploits the fact that both the luminosity of a spiral galaxy and its rotation velocity are relatively monotonic functions of mass. Thus by measuring the rotational velocity of a spiral galaxy one can predict its rest frame luminosity and use that as a standard candle. The fundamental equation for the Tully Fisher relation is $L(V_{\rm rot})\alpha V_{\rm rot}^{\alpha}$ where, $L()$ is the luminosity $V_{\rm rot}$ is the rotational velocity of the spiral and α is in the range $\sim$ (2-4), depending on how the rotational velocity was measured[20].

The fundamental plane is a three part relation where the effective radius R_e is a function of the surface brightness within that radius I_e and velocity dispersion σ_e

$$R_e = \sigma_e^{\alpha} I_e^{\beta} \tag{1.10}$$

where $\alpha \sim 1.4$ and $\beta \sim 0.9$ [20]. Here the relation uses velocity dispersion as a proxy for mass which in turn determines how the galaxy's stars will be distributed, which then allows elliptical galaxies to be used as standard rulers.

1.4 Constraints on the Cosmic Parameters

1.4.1 Bulk Flow

In section 1.2, I introduced δ and σ_8 as the density function and a smoothed measure of fluctuations of the density function. The variance of these quantities can be related to another important function in cosmology known as the power spectrum of fluctuation. The power spectrum is the Fourier space expansion of the distribution of matter and is measurable from Cosmic Microwave Background experiments.

The variance of δ can be calculated from the power spectrum by

$$\langle \delta^2 \rangle = V \int \frac{P(k) k^2 dk}{2\pi^2} \tag{1.11}$$

where V is the assumed periodic box with which the Fourier modes are contained, and P(k) is the power spectrum.

The variance of σ_8 can be similarly derived as

$$\langle \sigma_8^2 \rangle = V \int \frac{P(k) |W(k)^2| k^2 dk}{2\pi^2} \tag{1.12}$$

where $W(k)^2$ is the smoothing filter which for a 8 h^{-1} Mpc top hat sphere is

$$W(k) = 3 \left(\frac{\sin(kr_s)}{(kr_s)^3} - \frac{\cos(kr_s)}{(kr_s)^2} \right) \tag{1.13}$$

where r_s is the radius of the sphere or 8 h^{-1} Mpc.

It is notable that the observable σ_8 is mainly sensitive to fluctuations with a wavelength $\sim$ 8 Mpcs.

However if one looks at the relationship between velocities and density fluctuations

$$v_k = \frac{-iHfa\delta_k}{k} \tag{1.14}$$

Table 1.2: A short list of recent bulk flow measurements.

Size	Flow (km/s)	Galactic Direction (l,b)	Data source	Ref
50 h^{-1} Mpc	533 ± 263	(324 ± 27,-7 ± 17)	kSZ of CMB	1
$\sim$ 500 h^{-1} Mpc	less than 470	Not given	kSZ of CMB	1
$\sim$ 100 h^{-1} Mpc	416 ± 78	(282 ± 11,6 ± 6)	TF FP SN and other	2
$\sim$ 170 h^{-1} Mpc	$\sim$ 120	Not given	SDSS Galaxy groups	3
$\sim$ 150 h^{-1} Mpc	188 ± 100	(290 ± 30,20 ± 30)	SN	4
$<$ 150 h^{-1} Mpc	0	Not given	SN	4
$\sim$ 800 h^{-1} Mpc	600 to 1000	(283 ± 14,12 ± 14)	kSZ of CMB	5

(1) [21]; (2) [22]; (3) [23]; (4) [24]; (5) [4]

it can be seen that the variation of velocities in a given volume, equation 1.15, becomes

$$\langle \sigma_{v,8}^2 \rangle = V \frac{H_0^2 f^2 a^2}{2\pi^2} \int P(k)|W(k)^2|dk \tag{1.15}$$

The main difference being two powers of k are removed, thus significantly greater sensitivity to smaller k or longer wavelength fluctuations.

I present a summarized list of recent bulk flow measurements in Table 1.2.

1.4.2 Introducing β

In section 1.2.3, I outlined what β is and how it is derived. In brief, it is the free normalization parameter between observed peculiar velocities and the linear theory predictions. The measured value of β cannot be directly compared between surveys because β depends on the bias of the tracers used to map out the density field. I fit β and make comparisons to other published results in Chapter 2.

Table 1.3: A short list of recent γ measurements.

γ	σ_γ	Data source	Ref
0.547	0.088	6dfGS + WMAP7	1
0.661	$^{0.302}_{-0.203}$	SN +CMB +BAO +linear growth factors	2
0.653	$^{0.372}_{-0.363}$	Same as above + Gamma-Ray Bursts	2
0.64	0.05	CMASS anisotropic clustering + CMB	3
0.546	$^{0.072}_{-0.071}$	ROSAT + Chandra + CMB + Wigglez + 6dFGS + SDSS	4
0.586	$^{0.079}_{-0.074}$	6dF + WiggleZ	5

(1) [25]; (2) [26]; (3) [27]; (4) [28]; (5) [29]

1.4.3 Introducing γ

I concluded section 1.2.3 by demonstrating that β is a degenerate coupling of Ω_m, γ and σ_8. In the paper upon which Chapter 3 is based, the degeneracy between all three of these parameters is partially resolved, however in this thesis I focus on the extraction of the value of γ. γ itself was proposed as a model independent parametrization of growth[17]. The full expression is $\gamma = 0.55 + 0.05[1 + w(z = 1)]$[17], where w is the equation of state parameter of dark energy, and the parametrization is equivalent to within 1% of the analytical exact growth solution (as long as Ω_m is larger than 0.01 and $w(z) = -1$) for all z, as such a significant deviation from $\gamma = 0.55$ would in turn imply a significant deviation from established cosmology. I present a brief list of some recent γ measurements in Table 1.3.

1.5 Outline of primary topics

In Chapter 2, I present my first paper from my work at Waterloo. The resulting paper is [30]. I also present a comparison between data sets, various bulk flows which can be

extracted from the data, and finally a measurement of β. In Chapter 3, I present a shortened version of [31], a paper of which I was a co-author. I further present constraints made on the growth factor γ. Chapter 4 is the precursor of a third paper which I am currently writing. Here I present the application of N-body results to test the processes that are applied in the measuring of β from redshift surveys, specifically the process of reconstructing real space locations for tracers (such as galaxies) from their redshift space locations. I also present measurements of bias as a function of chosen tracers, the smoothing length applied to those tracers, mass threshold cuts, and the β value that can be extracted from and N-body halo catalog when converting between redshift space and real space iteratively (assuming perfect knowledge of real space halo positions and velocities). In Chapter 5, I will draw conclusions.

1.6 Statement of Contributions

Chapter 2 of this thesis is a reproduction of [30], a paper published in Monthly Notices of the Royal Astronomical Society, of which I was the first author. For this paper Mike Hudson provided a base list of SN list with distances, redshifts, peculiar velocities, and uncertainties to which I added the supernovae from [19]. I completed the top hat sphere bulk flow tests for all of the data sets. The Minimum Variance results were computed by Hume Feldman. The predicted peculiar velocities used in the measuring of β were provided by Hudson. The computation of β was completed by myself.

Chapter 3 of this thesis is based heavily upon the first draft of a paper published in The Astrophysical Journal Letters. The first draft was written by myself, although some of the paper was re-written by Mike Hudson, before being published as Hudson and Turnbull 2012. The results presented in this thesis are not the full results of the paper but rather the results that were generated by myself.

Chapter 4 is based upon my completed works since the completion of the second paper. Guilhem Lavaux provided the N-body results, the remainder of the results are my own.

The remaining Chapters are my original works.

Chapter 2

Cosmic flows in the nearby universe from Type Ia Supernovae.

Peculiar velocities are one of the only probes of very large-scale mass density fluctuations in the nearby Universe. I present new "minimal variance" bulk flow measurements based upon the "First Amendment" compilation of 245 Type Ia supernovae (SNe) peculiar velocities and find a bulk flow of 197 ± 56 km s^{-1} in direction $l = 295^\circ \pm 16^\circ$, $b = 11^\circ \pm 14^\circ$. The SNe bulk flow is consistent with the expectations of ΛCDM. However, it is also marginally consistent with the bulk flow of a larger compilation of non-SNe peculiar velocities [3]. By comparing the SNe peculiar velocities to predictions of the IRAS Point Source Catalog Redshift survey (PSCz) galaxy density field, I find $\Omega_m^{0.55}\sigma_{8,\mathrm{lin}} = 0.40 \pm 0.07$, which is in agreement with ΛCDM. However, I also show that the PSCz density field fails to account for 150 ± 43 km s^{-1} of the SNe bulk motion.

2.1 Introduction

In the standard cosmological model, gravitational instability causes the growth of structure and peculiar velocities. In the regime where the perturbations are linear, there is a simple

relationship between density and peculiar velocity [32]

$$\mathbf{v}(\mathbf{r}) = \frac{f}{4\pi} \int_0^\infty d^3\mathbf{r}' \delta(\mathbf{r}') \frac{\mathbf{r}' - \mathbf{r}}{\mid \mathbf{r}' - \mathbf{r} \mid^3} \tag{2.1}$$

where the growth factor f is equal to $\Omega_m^{0.55}$ in flat ΛCDM models [17], δ is the normalized mass density fluctuation field, $\delta = (\rho - \bar{\rho})/\bar{\rho}$, and $\mathbf{r}$ are coordinates in units of km s^{-1}. A brief derivation can be found leading up to eq. 1.5.

Given set of peculiar velocities, one can define a bulk flow as their average velocity; ideally the peculiar velocity tracers are dense and numerous enough that the resulting average is representative of the velocity of the volume. The bulk flow is then primarily due to structures on scales larger than the volume over which the bulk flow is measured (see Appendix A of [33] for a derivation). Hence, bulk flows are probes of the large-scale power spectrum of *matter* density fluctuations.

The ΛCDM model, once normalized by WMAP7 [1] observations of the Cosmic Microwave Background (CMB), fully specifies the r.m.s. fluctuations of δ on all scales, and hence the cosmic r.m.s. of bulk flows [3]. While most studies of bulk flows agree on the general direction of the flow, there is some disagreement as to the amplitude and scale. [3] applied a "Minimal Variance" (MV) weighting scheme to a compilation of 4481 peculiar velocity measurements. Their results correspond to a sample with an effective Gaussian window of 50 h^{-1} Mpc and show a bulk flow of 407 ± 81 km s^{-1} towards $l = 287° \pm 9°$, $b = 8° \pm 6°$, which is in conflict with ΛCDM + WMAP7 at the 98 percent confidence level. The most controversial bulk flow result is the kinetic Sunyaev-Zeldovich flow dipole reported by [4], who found a bulk flow on the order of 1000 km s^{-1} in the direction of $l = 296° \pm 28°$, $b = 39° \pm 14°$ over a scale of at least 800 h^{-1}Mpc. If correct, this result would strongly conflict with ΛCDM + WMAP7.

Another approach to understanding large-scale motions is to try to reconstruct the motion of the LG with respect to the CMB [627 ± 22 km s^{-1} towards $l = 276° \pm 3°$, $b = 30° \pm 2°$; 34] by measuring the distribution of galaxies and calculating the peculiar velocity of the Local Group (LG) using Eq. (2.1). Given the gravitational instability model

of linear theory, the predicted velocity should converge to the measured CMB dipole for a sufficiently large survey volume. The application of Eq. (2.1) is difficult in practice because there are few redshift surveys that are both all-sky and deep. For example, [35] found that the predicted dipole from the IRAS Point Source Catalog Redshift survey [36, hereafter PSCz] converged to 13.4 degrees of the CMB dipole by 30,000 km s^{-1}. However, [37] reanalyzed the same data set and found that significant power was required on large scales, which was missed by the original analysis. Other studies have been based on the Two Micron All-Sky Survey Redshift Survey [38, hereafter 2MRS]: [39] and found probable convergence, but [40] concluded that convergence was not obtained by 12,000 km s^{-1}, and may not be until well beyond 20,000 km s^{-1}. In another study, using only the infrared fluxes [41] concluded that even at an effective distance $\sim 300h^{-1}$ Mpc ($K_s < 13.5$) the flux dipole had not converged.

In this paper, I use Type Ia SNe for peculiar velocity tracers. SNe have also been used as peculiar velocity probes by a number of authors [24, 42–49].

An outline of this chapter is as follows: In section 2, I introduce the data sets that I used. Section 3 presents the bulk flow of the SNe, using both simple weighting schemes as well as the "Minimal Variance" scheme of [3]. Section 4 compares individual SNe peculiar velocities to the predictions of the IRAS PSCz density field. I discuss the implications of these results in Section 5, and present these conclusions in Section 6. Throughout, I adopt $\Omega_m = 0.3$, $\Omega_\Lambda = 0.7$, and quote distances in units of km s^{-1}.

2.2 Data and Calibration

In this study, three primary data sets of nearby SNe (with distances less than 20,000km s^{-1}) are combined.

I refer to the first of these data sets as the 'Old' sample and it contains 106 SN the youngest being from 2002, drawn from two sources: [50] and [2]. Of the SNe in the 'Old' sample, 34 are from [50]. The remaining 72 SN in 'Old' are from [2]. The second data set,

which I refer to as 'Hicken', contains the remaining 113 SNe from [2] after cutting objects at distances larger than 20,000 km s^{-1} and cutting two more objects (sn2007bz and sn2007ba) because they deviated by more than 3σ after the first round of fitting (as described below). The last set is the recently released data set from 'The Carnegie Supernova Project' [19, hereafter CSP], containing 28 SNe. Two of these objects were discarded due to the 20,000 km s^{-1} distance cut, leaving 26 usable SNe. The CSP's reported uncertainties only reflected the derived distance modulus residual spread. A second intrinsic uncertainty (σ_{SN}) in the magnitude of the SNe was added in quadrature by fitting a flow model and reducing the reduced chi-squared fit to 1.00. The intrinsic uncertainty was found to be 0.107 mag (slightly smaller than the 0.12 mag found by the CSP due to cuts and the additional free parameters of bulk flow). For further discussion of the light curve fitting, and consequences there of, for the 'Old' and 'Hicken' data sets see Section 2.3.

I combine these three sets to create a new sample, that I dub the 'First Amendment' (A1) compilation which I consider to be an extension to the 'Constitution' data set[1].

Where the observed SNe in the data sets were known to be contained within a cluster of galaxies, the redshift of the cluster was used for the observed velocity distance rather than the redshift of the supernova itself. Substituting cluster velocities for supernova velocities removes a significant source of thermal noise as objects in clusters can have a velocity rms of thousands of km s^{-1} . This process was applied to all three data sets. For galaxies not in clusters, the redshift of the host galaxy was used if the host galaxy redshift was recorded in NED, which occurred in all but two cases. For the remaining two cases I used the redshifts of the SNe. Galactic longitudes and latitudes for the Carnegie set were also taken from NED.

The A1 data set has a characteristic or uncertainty-weighted depth of 58 h^{-1}Mpc, where

[1]The 'Old' and 'Hicken' sets combined resemble very closely the 'Constitution' set from [2] in terms of which supernovae are included. The light curve fitter used here (MLCS2k2) differs from that of the 'Constitution' data set (SALT2).

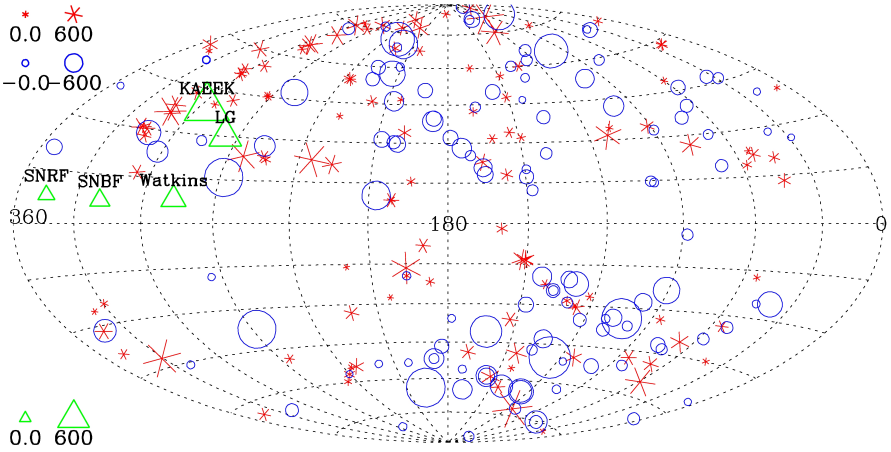

Figure 2.1: An Aitoff projection of the data with circles (asterisks) representing SNe with peculiar velocities towards (away from) the LG. Larger symbols represent larger peculiar velocities in accordance with the scale shown top and bottom left. Also plotted in triangles are the direction motion of the LG with respect to the CMB, the [3] bulk flow direction, the kinetic Sunyaev-Zel'dovich bulk flow direction of [4, labeled KAEEK], and the new results (labeled SNBF for the bulk flow results from Section 3 and SNRF for the residual flow discussed in Section 4).

I define the characteristic depth to be

$$r_* = \frac{\Sigma\ \mathbf{r}/\sigma^2}{\Sigma\ 1/\sigma^2} \tag{2.2}$$

where σ is the total uncertainty in each SNe's peculiar velocity and $\mathbf{r}$ is the coordinates in units of km s^{-1}.

In Fig. 2.1, I present the results, the raw data, and the bulk flow directions that other surveys have found in an Aitoff projection. In Fig. 2.2, I present the A1 data set in a Hubble Diagram divided into its three subsets. For all three data sets the intrinsic uncertainty of SNe brightness is the dominant source of error. Thus, for all the SNe the percent error is approximately 6 percent of the measured distance, with the scatter for the 'Old' and 'Hicken' subsets being larger.

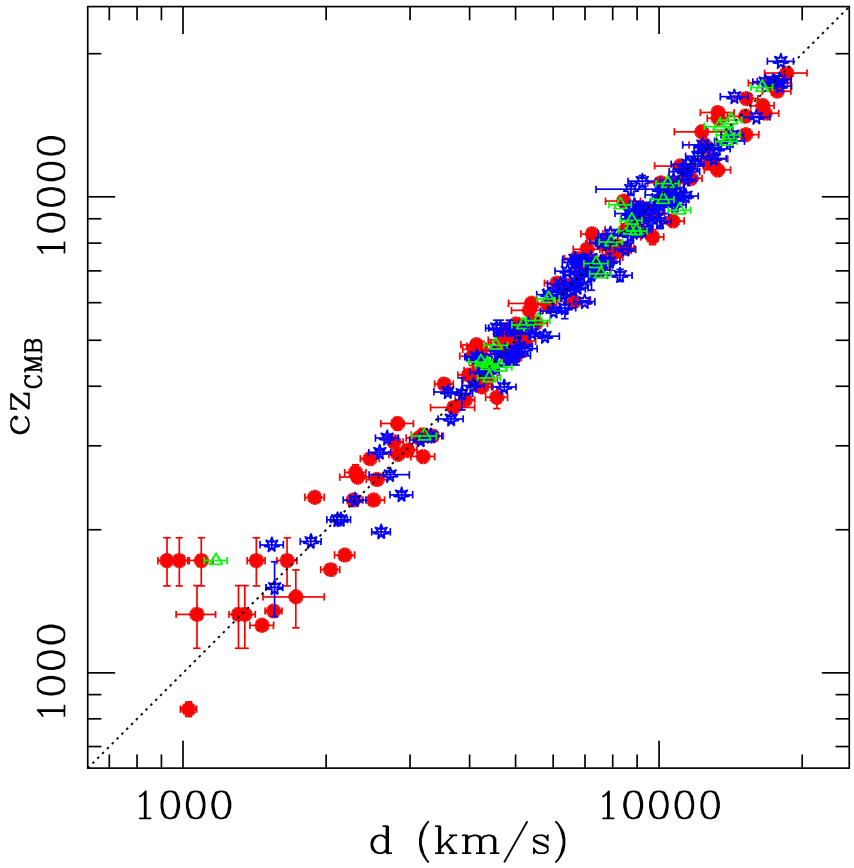

Figure 2.2: A Hubble diagram showing the three subsets that make up the A1 data set: 'Old' (red filled circles), 'Hicken' (Blue stars) and 'Carnegie' (green triangles). The error bars can be seen to be approximately constant in the log log diagram or increasing proportionally to the distance, as to be expected with the dominant error in most cases being the intrinsic uncertainty in the luminosity of SNe.

Table 2.1: Results for 162 SNe from [2] fit with the MLCS2k2 light curve fitter either with $R_V = 1.7$ or $R_V = 3.1$.

	Number	Mag	l°	b°	V_X	V_Y	V_Z
ML Thermal noise=250 km s^{-1}					km s^{-1}	km s^{-1}	km s^{-1}
$R_V = 1.7$	162	220±70	298±18	9±14	103±68	-191±73	35±52
$R_V = 3.1$	162	175±70	310±25	14±18	108±70	-131±75	43±53

2.3 Light curve parameter comparisons

The A1 data set is composed of three different SNe catalogs; this complicates the description of the light curve fitting procedures used because the catalogs used different methods. In the 'Old' sample are 34 SNe from [50], most of the SNe are fit using the MLCS2k2 light curve fitter with a reddening law parameter R_V of 3.1 (for SN with high extinction, R_V was a free fit parameter with a tight prior of 3.1). The remaining 72 SN in 'Old' are from [2] and are also fit using MLCS2k2, but with a reddening law parameter R_V of 1.7. The second data set, which I refer to as 'Hicken', contains the remaining 113 SNe from [2] and are all fit with MLCS2k2 with a reddening law parameter R_V of 1.7. The 'Carnegie' set containing 28 SNe were fit with a R_V as a free variable. The light curve fitter used for the 'Carnegie' set is described in detail in the original paper [36].

For SNe fit by [2], four distances were reported for each SN. I use the distances reported using the MLCS2k2 fitting procedure rather than either of the SALT procedures for multiple reason. To start the MLCS2k2 process determines host reddening on a case-by-case basis. Furthermore, of the two published MLCS2k2 methods I use the results with a reddening law parameter R_V of 1.7 instead of 3.1 since [2] show that the Hubble residuals for high-extinction SNIa's using R_V=3.1 are systematically negative, (suggesting that the extinction is overestimated). I study the effect the choice of R_V parameter has upon bulk flow measurements to explore systematics. [2] provide distances to 162 SNe using both R_V = 1.7 and R_V = 3.1.

I fit both of these data sets for bulk flows using the ML method to investigate the systematics. The results of this comparison can be seen in table 2.1. Although the results for the two light curve fitters agree to less than one σ in each of the 3 degrees of freedom, the data sets are fit to the same light curves, so they are not independent. This result highlights how large the systematic errors are for bulk flow surveys, in part reflected by the large σ_{SN}, which in most cases dominates the uncertainty budget for peculiar velocity surveys.

2.4 Bulk Flow

In this section, I discuss the bulk flow, which is the simplest statistic that can be derived from a peculiar velocity survey.

2.4.1 Methods

I use two methods to measure the bulk flow. The first is a Maximum Likelihood (ML) method that minimizes the measurement uncertainties. The ML method is the traditional method used and I apply it in order to compare new results with previous ML results. However, ML methods have the disadvantage of returning the bulk flow of a specific sparse *sample* of peculiar velocity tracers rather than the bulk flow of a regular *volume*. Comparisons between ML results are complicated by the different spatial sampling. Instead, what is of greater interest is the bulk flow of a standardized volume. To estimate this, a "minimum variance" (MV) bulk flow was calculated as first introduced by [3].

Maximum Likelihood

I fit a simple flow model (v_{pred}) to the SNIa peculiar velocity data. In the case of the bulk flow $\mathbf{V}$ in the CMB frame, this flow model reduces to the radial component of the bulk

flow vector for each SNe, i. e.

$$v_{\mathrm{pred},i} = (\mathbf{V} \cdot \hat{\mathbf{r}}_i) \tag{2.3}$$

where $\hat{\mathbf{r}}_i$ is the unit vector pointing to each supernova.

In the maximum likelihood method, the weights are simply determined by the total uncertainty on the peculiar velocity of each object. Uncertainties in the observed peculiar velocity can be approximated well by a Gaussian, in which case the Maximum-Likelihood solution can be approximated by the following χ^2

$$\chi^2 = \sum_i \frac{[cz_{obs,i} - (r_i + v_{\mathrm{pred},i})]^2}{\sigma_i^2} \tag{2.4}$$

where cz_{obs} is the observed redshift in km s^{-1}, $\mathbf{r}_i$ is the distance converted from the reported distance modulus in km s^{-1}, $\mathbf{v}_{\mathrm{pred},i}$ is the model velocity I am trying to measure, as predicted for SNe i, and σ_i is the total uncertainty on the peculiar velocity of object i in units of km s^{-1}. This total uncertainty is the quadrature sum of the measurement error $\sigma_{m,i}^2$, the intrinsic uncertainty on SNe magnitude σ_{SN} (both converted from magnitudes to km s^{-1}) and a "thermal noise" term (σ_{th}) in units of km s^{-1} due to uncertainties in the flow model, such that

$$\sigma_i^2 = \sigma_{m,i}^2 + \sigma_{SN}^2 + \sigma_{th}^2 \tag{2.5}$$

Note that since the σ_{SN}^2 term is converted from an uncertainty on magnitude, it is proportional to the distance to the SN. σ_{SN}^2 is often the dominant source of uncertainty since the thermal term is only important in nearby supernovae where the $\sigma_{m,i}^2$ and σ_{SN}^2 terms are small. The results are only weakly dependent upon the precise value chosen. Here, where the flow model is a simple bulk flow, I set the thermal noise to 250 km s^{-1}, which is consistent with previous work. The impact of this choice for the thermal noise is discussed in the results below.

I let each sub-sample of the A1 data set have a freely-varying independent Hubble term to identify degeneracies, to avoid underestimating final uncertainties, and to account for the fact that each subset may have slightly different calibration. None of the fits preferred

a Hubble value that varied by more than 1 percent from the value drawn from the original sources.

Minimum Variance Method

While the ML method described above is the best estimator of the bulk flow of a sparse sample, it is restricted in that it can only really characterize a particular survey, that will have its own errors and a specific and somewhat ill-defined geometry. The ML method is also, in a sense, density sampled, with higher density regions being more likely to contain a SN than voids. Most importantly, because the weights in the ML method are determined by the uncertainty on position in km s^{-1}, ML methods can be dominated by nearby SN that have smaller distance uncertainties.

To better approximate a *volume*-weighted bulk flow, the prescription described in [3] to estimate the volume flow was applied. Each SN is weighted so as to minimize the variance between the bulk flow measured in the real sample and the bulk flow as it would be measured in a perfectly-sampled 3D Gaussian. A Gaussian with an "ideal" radius of $R_I = 50h^{-1}$ Mpc was adopted. Effectively, weights are assigned to each SN based on their proximity to other SNe in the data set, and on how they compare with an ideal uniform sampling. This weighting scheme is specifically designed to maximize sensitivity to large scales. The MV weighting scheme has been tested using mock catalogs drawn from N-body simulations by Agarwal et al. (in preparation), who demonstrate that the recovered MV bulk flows are unbiased and have errors within the range expected from linear theory.

2.4.2 Consistency of SNe Subsamples

Before analysis of the combined SNe sample is undertaken, it is important to confirm that the data subsamples agree with one another. A χ^2 statistic for each pair of subsamples was calculated, following the analysis of [3], which accounts for sparse sampling effects. The

Table 2.2: χ^2 for 3 DoF for the surveys for $\Omega_m = 0.258$. If the χ^2 value is greater than 7.8, the two surveys disagree at a greater than 95% confidence level. The probabilities resported are the χ^2 test probability of agreement between the two.

	$R_I =$	$50h^{-1}$Mpc
Survey	χ^2	Probability
Old vs Hicken	0.173	98.2
Old vs Carnegie	2.293	51.4
Hicken vs Carnegie	1.369	71.3

χ^2 statistic used is given by the equation

$$\chi^2 = \sum_{i,j} (\Delta V_i)(C_{i,j})^{-1}(\Delta V_j). \tag{2.6}$$

where $\Delta\vec{V}$ is the bulk flow vector, and $\mathbf{C}$ is the covariance matrix taking into account the window functions of both surveys and the power spectrum, (see in equations 21 - 23 of [3]). The results are shown in Table 2.2. In summary, all three subsamples are found to be consistent with each other.

2.4.3 Results

In Table 2.3, I present a summary of the results from the bulk flow, subdivided by data set and by weighting scheme. The ML bulk flow for the A1 sample was found to be 197 $\pm$ 56 km s^{-1} in direction $l = 295^\circ \pm 16^\circ$, $b = 11^\circ \pm 14^\circ$. This is significantly different from zero at the 99.9% confidence level.

As discussed above, the ML method gives most weight to SNe with the lowest errors in units of km s^{-1}, i.e. the nearest SNe. In order to reduce the impact of these nearby SNe, it is interesting to redetermine the bulk flow excluding nearby objects. The middle section

of Table 2.3 shows the bulk flow using only SNe with 6000 km s^{-1} $< d <$ 20000 km s^{-1}. This subsample indicates a slightly higher amplitude flow, albeit with larger error bars: 330 ± 120 km s^{-1} towards $l = 321°$, $b = 20°$.

Finally, the MV results shown in the third section of Table 2.3 should give the most robust estimates of the flow of a Gaussian volume of radius 50 h^{-1}Mpc. For the entire A1 sample, the MV flow is 248 $\pm$ 87 km s^{-1} in the direction $l = 319° \pm 25°$, $b = 7° \pm 13°$.

These values are lower than the LG's motion in the CMB frame, indicating that some of the LG's motion must come from structures within the survey volume (such as the Virgo and Hydra-Centaurus superclusters).

To investigate the sensitivity of these results to the value of the thermal noise I adjusted it by $\pm$ 100 km s^{-1}; When so tested, the final magnitude of the A1 sample MV flow only changed by $\pm$ 31 km s^{-1}.

2.4.4 Bulk Flow: Cosmology and Comparisons

It is interesting to compare this ML bulk flow result to that of [48], who apply a maximum likelihood bulk flow fit to the Union2 catalogue of Type Ia SNe [51]. The Union2 catalogue contains 557 SNe, of which 165 are within 30,000 km s^{-1}. [48]'s analysis yields a bulk flow velocity of 260 $\pm$ 150 km s^{-1} based on SNe within 18000 km s^{-1}. The A1 sample yields a ML result of 196 $\pm$ 55 km s^{-1}, which is consistent with theirs. It must be noted that the agreement between these results is not as significant as might at first be assumed because there is significant overlap between the data sets. However, Union2 uses SALT2 rather than MLCS2k2 (R_V=1.7) to obtain SN distances from the light-curve data.

[24] also analyzed the Union2 catalog, spliting it into two subsets. They defined a nearby set with 132 SNe at $z < 0.05$ for which they found a bulk flow of 188^{+119}_{-103} km s^{-1} towards $l = 290^{+39}_{-31}°$, $b = 20^{+32}_{-32}°$ which also agrees well with these results. The remaining 425 high-z SNe show no significant bulk flow. This is expected since the peculiar velocity

Table 2.3: Bulk flow for all three SNIa data subsets and the combined First Amendment set. For comparison the MV50 result from [3] are also included. Note the uncertainties quoted for the ML method are the propagated uncertainties from measurements. The uncertainties for the MV method also include the additional noise due to non-uniform sampling.

	Number	Mag	l°	b°	V_X	V_Y	V_Z
ML Thermal noise=250 km s^{-1}					km s^{-1}	km s^{-1}	km s^{-1}
Old	106	226±76	307±21	4±15	136±76	-180±81	-35±59
Hicken	113	142±85	283±41	30±37	27±94	-120±96	71±78
Carnegie	26	260±140	330±170	76±38	54±182	-35±230	250±150
A1	245	196±55	300±17	15±14	94±55	-165±58	50±44
ML Thermal noise=250 km s^{-1}, $d > 6,000$ km s^{-1}							
Old	45	450±190	331±26	6±21	390±200	-210±190	44±160
Hicken	76	280±180	313±33	27±25	170±170	-180±190	130±110
Carnegie	15	1132±850	117±14	16±20	-490±540	970±810	310±300
A1	136	330±120	321±20	16±15	250±120	-200±130	94±84
MV Weighting $R_I = 50h^{-1}$ Mpc Thermal noise=250 km s^{-1}							
Old	113	240±110	318±26	-4±21	180±110	-160±110	-16±86
Hicken	113	250±110	310±25	5±20	160±110	-190±110	20±85
Carnegie	28	250±150	0±340	81±43	40±190	0±240	250±150
A1	**254**	**249±76**	**319±18**	**7±14**	**186±75**	**-162±77**	**32±59**
[3]	4481	407±81	287±9	8±6	114±49	-387±53	57±37

errors are typically 6% of the distance to the source, and for this distant sample the errors per SNe measured in km s^{-1} are extremely large.

Another interesting recent analysis of all peculiar velocities is by [3], who studied peculiar velocities mostly from Tully-Fisher, Fundamental Plane and SNe. They found that those subsamples had bulk flows consistent with each other[2]. They combined the individual peculiar velocity samples into a "Composite" sample of 4481 peculiar velocity tracers, which was found to have a MV50 bulk flow of 407 ± 81 km s^{-1} towards $l = 287^\circ \pm 9^\circ$, $b = 8^\circ \pm 6^\circ$. This result is inconsistent with ΛCDM at the 98% CL. However, their sample is not independent of ours. 103 of the 108 SNe which make up the "Old" subset of A1 are common to both A1 and Composite, although the latter takes SNe distances from [53]. When all SNe data are removed from the 'Composite' data set, the two surveys become completely independent, and can be compared using the same formalism described in Section 3 of this paper and Section 5.1 of [3]. it was found that the 'Composite excluding SNe' MV50 bulk flow and the A1 MV50 results are consistent with each other, although the agreement is marginal: χ^2 of 6.4 for 3 directional degrees of freedom yields a 9 percent probability that the two results are consistent.

Lastly, these results can be compared directly to the expectations for a ΛCDM universe. A plot showing the expectations of the one dimensional rms for perfectly sampled Gaussian sphere can be found in the top three plots of figure 5 from [22]. The expectation for the one dimensional rms for a perfect Gaussian is 80 km s^{-1}. When you take into account the sparse sampling of the real A1 data set, this rises slightly to 91.2 km s^{-1} assuming a σ_8 of 0.8 and Ω_m of 0.258.[3]. If you then include the propagation of measurement uncertainties the total expected rms for surveys equivalent to ours at different locations in space is 121 km s^{-1}. This prediction leads to χ^2 of 3.70 for 3 directional degrees of freedom yielding a 70 percent probability that the A1 data set is consistent with ΛCDM.

[2]Except for the BCG sample of [52], which was excluded from further analysis.

[3]In the rest of the paper, because SN distances are insensitive to the value of Ω_m I used $\Omega_m = 0.3$. The predicted one dimensional rms drops slightly to 88.4 if this slightly higher value of Ω_m is used in the prediction

2.5 Predicted gravity field

2.5.1 Introduction

The MV weighting scheme discussed above is designed to suppress the effects of small-scale flows that would otherwise "alias" power into the bulk-flow statistic. An alternate method for removing the effects of small-scale structure on flow measurements is to assume gravitational instability and linear perturbation theory Eq. (2.1) and to predict the peculiar velocities using a model of the density field (derived from an all-sky galaxy redshift survey). The result is a model-dependent correction to measured peculiar velocities which can separate local effects from large-scale density waves from outside the survey volume.

Consider an all-sky redshift survey that extends to a distance $R_{\rm max}$. The peculiar velocity of a given SN, located at position $\mathbf{r}$, can be modeled by setting $v_{{\rm pred},i}$ of Eq. (2.4) to a function with two terms

$$\mathbf{v}_{\rm pred}(\mathbf{r}) = \frac{\beta}{4\pi}\int_0^{R_{\rm max}} d^3\mathbf{r}'\delta_g(\mathbf{r}')\frac{\mathbf{r}'-\mathbf{r}}{\mid \mathbf{r}'-\mathbf{r} \mid^3} + \mathbf{U} \tag{2.7}$$

where $\beta = f/b$, b is the linear bias between galaxy density and mass density, $\mathbf{U}$ is the *residual* bulk flow of the volume being driven by mass structure beyond $R_{\rm max}$. In principle, the residual velocities have tidal (shear) and higher order terms. [22] measured the the tidal and higher order terms for the "Composite" sample of [3], but found them to be small. I neglect these terms here and model the residual as a simple bulk flow $\mathbf{U}$.

The first term of $v_{\rm pred}$ is the predicted peculiar velocity induced by structure within the redshift survey volume ($\mathbf{r} < R_{\rm max}$). The model is scaled by β to match the observed peculiar velocities of the SNe tracers. The peculiar velocity data therefore yields information about Ω_m and b. The residual bulk flow $\mathbf{U}$ is the additional velocity of the entire redshift survey volume in the CMB reference frame, and is presumably due to sources beyond $R_{\rm max}$. In an ideal survey, $\mathbf{U}$ would be completely independent of any structure within $R_{\rm max}$. This de-coupling of $\mathbf{U}$ from β means that $\mathbf{U}$ can be used to test consistency with ΛCDM + WMAP7 on large scales and β can do so on smaller scales.

2.5.2 Data and Method

The PSCz is both all-sky and deeper than, for example, the 2MRS [38]. Here the PSCz density field reconstructed by [54] was used. For this study I applied the same 20,000 km s^{-1} limit to the PSCz as was applied to the SNe. The PSCz density field in the Supergalactic Plane is shown in Fig. 2.3.

I fit the SNe data using the same method as in Section 2.4.1, but now with a new model as given by Eq. (2.7). Since the integral is specified by the PSCz density field, the free parameters are β and the three components of $\mathbf{U}$. Since the PSCz plus bulk flow is a better flow model than a simple bulk flow, I reduce the thermal component to 150 km s^{-1}, which is consistent with previous studies [55].

2.5.3 Results

The results of the fits to each subset are given in Table 2.4. I find that the results from independent subsets are consistent with each other. For the A1 sample, the magnitude of the residual bulk flow was found to be 150 ± 43 km s^{-1} in direction $l = 345^\circ \pm 20^\circ$, $b = 8^\circ \pm 13^\circ$. This is significantly different from 0 at the 99.6% CL.

The value of β was found to be 0.53 ± 0.08, and is shown in Fig. 2.4. The fit is sensitive to a single outlier, sn1992bh, for which the PSCz prediction is rather high (1719 km/s). Excluding this SN, I found $\beta = 0.57 \pm 0.08$.

Again I investigated the sensitivity of these results on the thermal noise term by changing it by $\pm$ 100 km s^{-1}. Again the magnitude off the flow only changed by $\pm$ 20 km s^{-1}, and the β changed by $\pm$ 0.03.

2.5.4 Gravity field: cosmology and comparisons

As noted above, the residual bulk flow $\mathbf{U}$ is significantly different from zero at the 99.6% confidence level. This means that there are structures not found in the PSCz catalogue

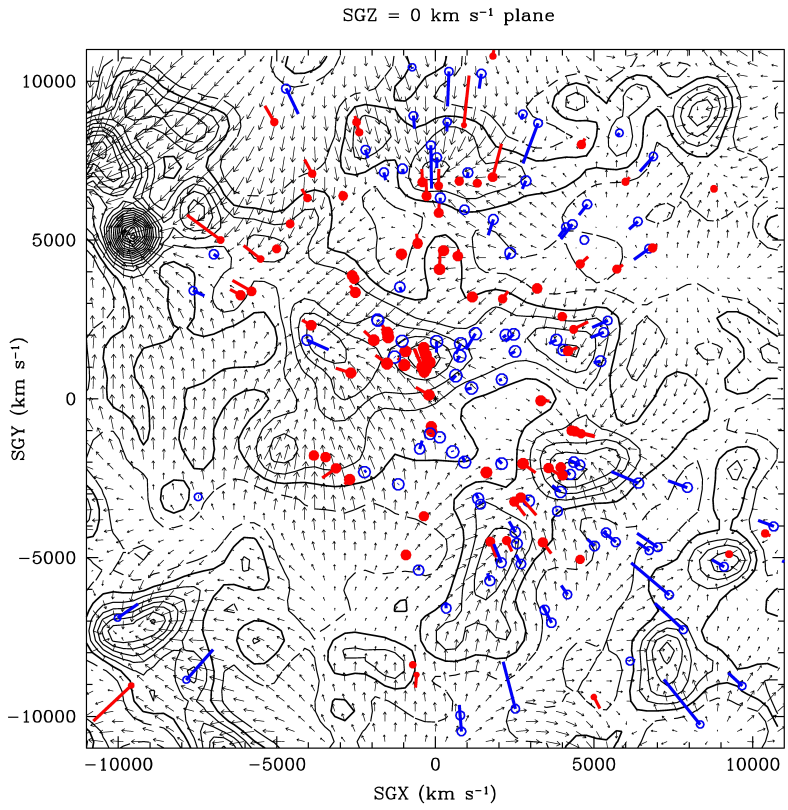

Figure 2.3: The Supergalactic Plane. The PSCz galaxy density field is shown by the contours, predicted peculiar velocities as small black arrows, and measured supernova positions as "tadpoles" with dots showing measured positions and tails showing the magnitude of the measured radial peculiar velocity. The thick black contour corresponds to a $\delta = 0$ (or contours where the density is the mean universal density). The red (filled circles) SNe have peculiar velocities away from the LG and the blue (open circles) SNe have peculiar velocities towards the LG.

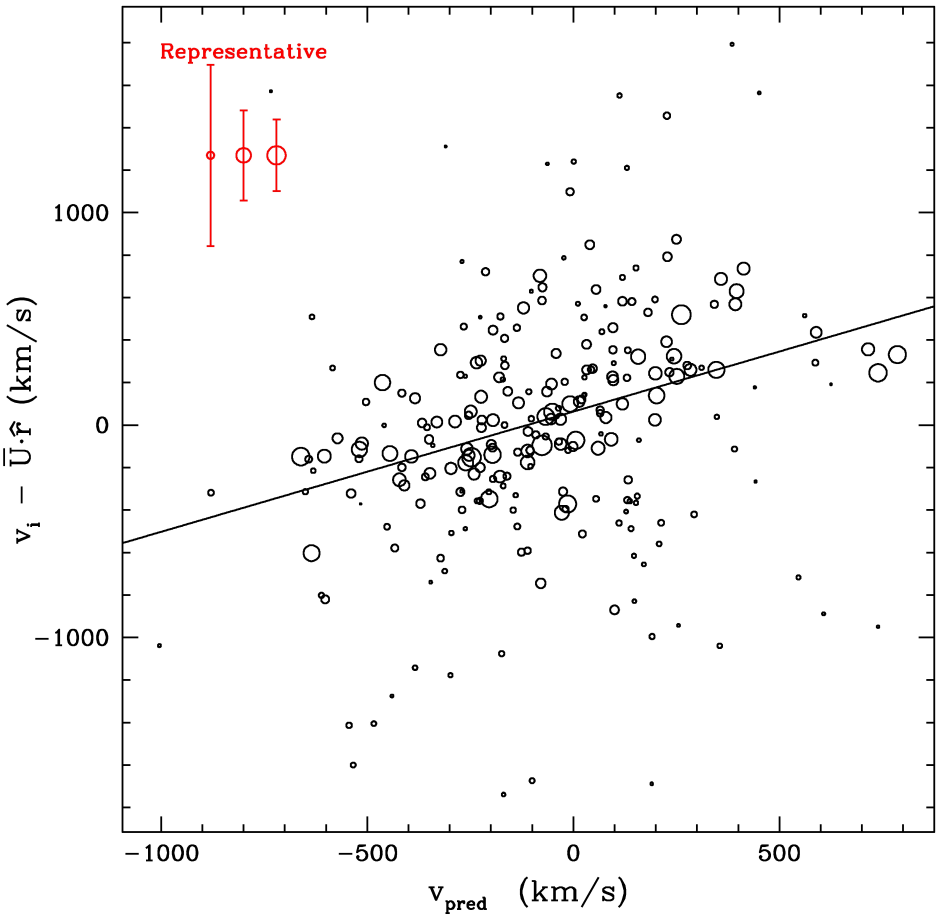

Figure 2.4: The observed peculiar velocity minus the measured bulk flow as a function of the linear-theory-predicted peculiar velocity for each SN, assuming $\beta = 1$. The circular symbol diameter scales with the inverse of the uncertainty (hence symbol area is proportional to weight). Representative error bars are shown in the top left. The slope is the fitted $\beta = 0.53$.

Table 2.4: Results from all three data subsets and the A1 full set with a linear perturbation theory model fit with a known matter distribution to find β and the residual flow U. Fit with β as a free parameter and with a thermal noise of 150 km s^{-1}. Note the uncertainties quoted for the this method are the propagated uncertainties from the measurements.

	# of SN	Mag	l°	b°	U_X	U_Y	U_Z	β	χ^2	Dof
					km s^{-1}	km s^{-1}	km s^{-1}			
Old	106	190±59	349±22	0±14	187±60	-36±73	0±46	.45±.11	139	101
Hicken	113	86±77	347±54	9±41	84±87	-19±83	13±66	.62±.13	102	108
Carnegie	26	290±150	347±41	31±26	240±170	-50±190	151±130	.82±.33	21	21
A1	245	150±43	345±20	8±13	144±44	-38±51	20±35	.53±.08	270	238

that contribute significantly to the total peculiar velocity of the LG. As discussed in detail in [55] these structures could be missing from the PSCz because they are (i) outside the survey volume (ii) in the Zone Of Avoidance, or (iii) present but underrepresented. The latter scenario may arise because the IRAS (far-infrared) selection on which PSCz is based is sensitive to dusty spirals, but less so to the mostly dust-free early types. [56], using the 6dF [57] survey of 2MASS-selected galaxies, showed that the Shapley and Horologium-Reticulum superclusters generate significantly more peculiar velocity than predicted by the PSCz, even allowing for a different β for 2MASS galaxies.

I found that, for IRAS-selected galaxies, $\beta = 0.53 \pm 0.08$. This value of $\beta_{\rm I}$ is in good agreement with the IRAS average of 0.50 ± 0.02 reported by [45],and with the SNIa-based result $\beta_I = 0.55 \pm 0.06$ of [44]. Comparing fitted values of β between redshift surveys of different galaxy types is complicated by the fact that the bias factor b need not be the same because different galaxy types may trace the underlining mass density differently. This problem can be alleviated by noting that in linear theory the r.m.s. fluctuation of the survey galaxies, say in an 8 h^{-1} Mpc top hat sphere ($\sigma_{8,\rm gal}$) is proportional to the true matter r.m.s. fluctuations in a volume of the same size (i.e. $\sigma_{8,\rm gal} = b\sigma_{8,\rm mass}$). Thus with the measured β_I and the known $\sigma_{8,I}$ from the IRAS PSCz of 0.80 ± 0.05 [58], I can calculate

the degenerate parameter pair $f\sigma_8$ (where I dropped the subscript 'mass'). This value of β corresponds to $f\sigma_8 = 0.424 \pm 0.069$.

I can then compare this $f\sigma_8$ to other studies. [5] compared the 2MRS density field and the SFI++ peculiar velocity data, and derived $f\sigma_8 = 0.31 \pm 0.05$. This is lower than the result found in this study, but not significantly so (1.5σ).

The $f\sigma_8$ parameter can also be derived from WMAP7 results. Recall that WMAP is observing fluctuations at an early epoch, when the perturbations were still well in the linear regime. To compare to WMAP7, I can convert the non-linear σ_8 measured in this work into the equivalent linear value using the prescription of [59]. If I assume an Ω_m of 0.272, the resultant $\sigma_{8,\mathrm{lin}}$ becomes 0.814 compared to its non-linear value of 0.867. Using this value of $\sigma_{8,\mathrm{lin}}$, $f\sigma_{8,\mathrm{lin}}$ drops to 0.40 ± 0.07, which is in excellent agreement with the results of WMAP7 [1]: $f\sigma_{8,\mathrm{lin}} = 0.39 \pm 0.04$.

2.6 Discussion

Attempts to determine the sources of the LG's motion amount to determining the factors in Eq. (2.1). While early studies focussed on simple toy infall models, more recent studies have concentrated on models of the density field with the two free parameters β and $\mathbf{U}$. For a single object, such as the LG itself, there is a trade-off between these parameters. Lower values of β lead to larger values of $\mathbf{U}$, which are required in order to match the same $\mathbf{v}$ on the left-hand side of equation 2.7. This degeneracy can be broken with more than one measurement. I have shown that the PCSz does not account for all of the motion of the LG, although it is plausible that some of the missing signal comes from within the survey volume in the form of extra infall into the highest-density superclusters.

An alternative explanation for the bulk flow has been proposed, namely that the CMB temperature dipole, or part thereof, is intrinsic and does not represent the peculiar velocity of the LG [A "tilted" Universe: 60–62]. This would lead to an illusory "bulk flow" which would extend well beyond the local volume, indeed to the horizon. The apparent

1005 ± 267 km s^{-1} bulk flow of $z < 0.25$ clusters claimed by [4], which is well outside the expectations of ΛCDM bulk flows, might be explained by such an effect. In such a scenario, there is an additional "bulk flow" $\mathbf{U}_{\rm tilt}$ which never vanishes no matter how deep a redshift survey $R_{\rm max}$ is used in Eq. (2.7). This measured $\mathbf{U}$ thus provides an upper limit on the $\mathbf{U}_{\rm tilt}$. The amplitude of the bulk flow found by [4] is inconsistent with this new measurement of $\mathbf{U} = 150 \pm 43$ km s^{-1}. However, amplitude of the [4] bulk flow is systematically uncertain. If I compare only the direction of the A1 fit $l = 345° \pm 20°$, $b = 8° \pm 13°$and the [4] direction $l = 296° \pm 29°$, $b = 39° \pm 15°$, the results are marginal: they disagree at approximately the 90% CL. Thus these results do not support the high amplitude bulk flow found by [4].

2.7 Conclusion

The peculiar velocities of a 245 SNe dataset, dubbed the "First Amendment", was analyzed. This new compilation is in marginal agreement with previous bulk flow results and with ΛCDM + WMAP7 predictions. The First Amendment compilation yields a bulk flow of 248 ± 87 km s^{-1} in the direction $l = 319° \pm 25°$, $b = 7° \pm 13°$.

I have compared the peculiar velocities to the predictions from the IRAS PSCz and have found $\Omega_{\rm m}^{0.55}\sigma_{8,\rm lin}$ of 0.40 ± 0.07, which is in excellent agreement with the ΛCDM + WMAP7 predictions and other previous measurements.

A residual flow of 150 ± 43 km s^{-1} $l = 345° \pm 20°$, $b = 8° \pm 13°$ was found for the IRAS Point Source Catalog as normalized with the First Amendment SNe. This may suggest that the IRAS PSCz undersamples massive dense superclusters such as the Shapley Concentration. Nevertheless, the small amplitude of the residual flow is in conflict with "tilted Universe" scenarios such as might be favoured by the kSZ analysis of [4].

As its name suggests, the First Amendment compilation is readily extendible as new SNe are found and their distances are published. Ongoing surveys such as CfA4 (95 SNe, Hicken, private communication), LOSS [63], Palomar Transit Factory [64], and CSP [65,

50 more distances expected soon], and upcoming surveys such as SkyMapper [100 SNe per year with $z < 0.085$, 66], Pan-Starrs, and LSST will eventually provide sufficient SNe to reduce the 20,000 km s^{-1} bulk and residual flow uncertainties to the systematic limits. Future results on $f\sigma_{8,\mathrm{lin}}$ are expected based on predicted peculiar velocities from the 2M++ redshift compilation [56]. Additionally, although individually less precise, Fundamental Plane distances and peculiar velocities can contribute significant precision to bulk flow surveys by sheer numbers. I wish to re-analyze the full 'Composite' data set from [67] after replacing the 103 SNe currently contained in that data set with the 245 SNe of A1, as well as to add the Fundamental Plane peculiar velocities from NFPS [68] and 6dF [69] when they become available. For now the results are data-limited, but the future promises many fruitful results from many promising surveys, and I await them eagerly.

Chapter 3

Measuring γ using $f\sigma_8$ at low and high redshifts

Peculiar velocities are an important probe of the growth rate of mass density fluctuations in the Universe. Most previous studies have focused exclusively on measuring peculiar velocities at intermediate ($0.2 < z < 1$) redshifts using statistical redshift-space distortions. Here I emphasize the power of peculiar velocities obtained directly from distance measurements at low redshift ($z \lesssim 0.05$), and show that it can be used to constrain the growth index γ, with the strongest constraints coming from peculiar velocity measurements in the nearby Universe. I find $\gamma = 0.621 \pm 0.08$, which is consistent with ΛCDM. Current peculiar velocity data already strongly constrain modified gravity models and will be a powerful test as data accumulate.

3.1 Introduction

The leading cosmological model is cold dark matter (CDM) combined with a cosmological constant. While the existence of dark matter is supported by a number of dynamical tests as well as the fluctuations in the CMB, the evidence for a cosmological constant is primarily

geometric (standard candles, standard rulers) and from measures of the expansion history of the Universe [for example 70, hereafter WMAP7+BAO+H_0]. Other modified gravity theories can mimic the expansion history of the ΛCDM model. [17] has emphasized that it is essential to measure the growth of structure as a function of cosmic time as this allows one to break this degeneracy. He also shows that for many models, the logarithmic derivative of the growth of structure can be parametrized as

$$f(z) \equiv \frac{d\ln D}{d\ln a} = \Omega_m(z)^\gamma \tag{3.1}$$

where z is the redshift, D is the linear perturbation growth factor, $a = 1/(1+z)$ is the expansion factor and γ is 0.55 for ΛCDM [71]. In contrast, for example, $\gamma = 0.68$ in the [72, hereafter DGP] braneworld modified gravity model [73].

There are several ways to measure the amplitude of the dark matter power spectrum at redshifts lower than that of the CMB, including cosmic shear from weak gravitational lensing and the abundance of rich clusters. Another promising way to probe the growth *rate* of structure is via peculiar velocities [74, 75]. Peculiar velocities are directly proportional to the derivative of the growth factor, i.e. proportional to f. In this work, f is degenerate with σ_8, so the measured result is the degenerate combination $f(z)\sigma_8(z)$.

There are two ways to measure peculiar velocities. The first method is statistical: given a galaxy redshift survey, the distortion of the power spectrum or correlation function in redshift space depends on $\beta = f/b$, where b is a galaxy bias parameter [15]. On large scales, I assume that linear biasing holds, i.e. $b = \sigma_{8,g}/\sigma_8$, where σ_8 is the root-mean-square density contrast within an 8 Mpc/h sphere, h is the Hubble parameter in units of 100 km/s/Mpc, and the subscript "g" indicates the fluctuations in the galaxy density, whereas no subscript indicates fluctuations in the mass density contrast. Galaxy redshift surveys also allow one to measure $\sigma_{8,g}$ directly, so one can combine the observables to obtain the combination $f\sigma_8 = \beta\sigma_{8,g}$. By combining redshift-space distortion (RSD) measurements of $f\sigma_8$ at different redshifts, one can study the growth of linear structures over a range of redshifts [74, 76–78].

A second method is to measure peculiar velocities directly by measuring distances to individual galaxies (via standard candles or standard rulers), and comparing these distances to their redshifts. I refer to this method as "measured distance" (MD). Combining these MDs with an independently derived density field (such as a redshift survey) and applying linear perturbation theory $f\sigma_8$ can be measured as described in Chapter 2.

The two peculiar velocity probes are complementary: RSDs require large volumes, driving one to surveys at higher redshifts. MDs have errors which are a constant fraction of distance. Hence the error in peculiar velocity in units of km s^{-1} increases linearly with distance and so MD surveys are necessarily restricted to low redshifts. However, as I will show it is the lowest redshift data that have the most "lever arm" for constraining the cosmological parameters considered here. The important point is that by combining high and low redshift measurements of $f(z)\sigma_8(z)$, many degeneracies in the cosmological parameters can be broken.

An outline of this Chapter is as follows. In Section 2, I present the data used in this analysis. In Section 3, I varied γ, but use CMB data to constrain the amplitude of $\sigma_8(z_{\rm CMB})$. I conclude and summarize in Section 4.

3.2 Data

In this study, I combine results for $f\sigma_8$ from two distinct methods. The majority of the data are from redshift-space distortion measurements of growth of structure. The redshift-space distortion technique assumes that if you stack enough galaxies their real-space total shape will be spherical, however the observed stack will not be spherical due to infall of matter into those galaxies. This infall will make the total shape appear flattened in redshift space. The radial width of the observed stack of galaxies is reduced while the transverse width is not the observed flattening can the be measured and converted into $f\sigma_8$. From the WiggleZ survey [77], I got the following data points: (z,$f\sigma_8$) = (0.22,0.390 $\pm$ 0.078),(0.41, 0.428 $\pm$ 0.044), (0.60, 0.403 $\pm$ 0.036), (0.78, 0.493 $\pm$ 0.065). [77] quote three further data points,

also from redshift space distortion measurements: (z,$f\sigma_8$) = (0.77,0.490 $\pm$ 0.180) from the VIMOS-VLT Deep Survey(VVDS), (0.17,0.51 $\pm$ 0.06) from the 2 degree field galaxy red-shift survey (2dFGRS), and lastly (0.35,0.44 $\pm$ 0.05) from the SDSS LRG catalogue. This last SDSS point I replaced with two data points from [78] (0.25, 0.351 $\pm$ 0.058), and (0.37, 0.460 $\pm$ 0.038) to bring the set up to date with more recent measurements with tighter precision.

The final two data points are from direct measurements of peculiar velocities. The first data point is the result from chapter 2 (0.02 , 0.398 $\pm$ 0.065).The second low-z peculiar velocity measurement is from [5], who analyzed 2830 Tully-Fisher peculiar velocities at $z < 0.03$ and compared these to the predictions from the galaxy density field derived from 43,000 galaxy red-shifts from the Two Micron All-Sky Survey Redshift Survey [38, called 2MRS from here on]. Rather than the simple fit used above, [5] applied a sophisticated spherical harmonic decomposition method and found a $f\sigma_8$ of 0.314 $\pm$ 0.048.

I stress the important point that these two peculiar velocity determinations are completely independent: they have different peculiar velocity samples, different density fields and different reconstruction methods. The two peculiar velocity measurements are consistent with each other: the difference is 0.084 ± 0.08.

These data are summarized in Table 3.1. The RSD and MD measurements are shown in Figure 3.1.

3.3 Constraints on γ

In the ΛCDM model, $\gamma = 0.55$ but it is possible that the real value of γ differs from this model value. With high and low-z measurements of $f\sigma_8$ it is possible to measure the growth rate index γ. However, γ is very degenerate with the other two parameters of

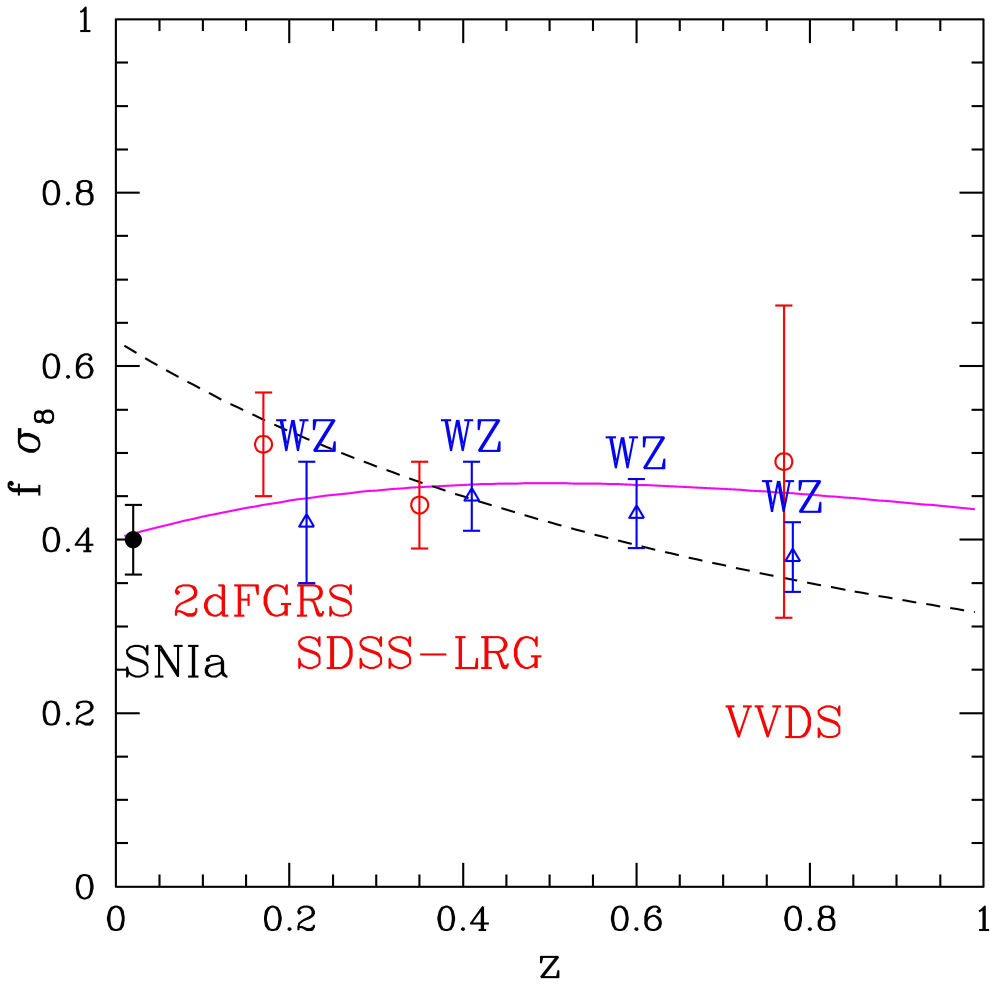

Figure 3.1: Growth parameter $f\sigma_8(z)$ as a function of z. The data and errorbars are labelled as in Table 1. The ΛCDM model with WMAP7+BAO+H_0 parameters $\Omega_{\rm m,0} = 0.275$, $\sigma_{8,0} = 0.816$ is shown by the solid magenta curve. Note that the high-redshift RSD points assume the ΛCDM redshift-distance relation to correct for the AP effect and hence the appropriate value of $f\sigma_8(z)$. The black dashed curve shows a reference result with $\Omega_m = 1$, $\sigma_8 = 0.63$, and h= 0.702. The curve is γ independent, by construction, and fits the redshift-distortion measurements, but not the low-z peculiar velocity measurements (highlighting the importance of low-z measurements).

Table 3.1: Measurements of $f\sigma_8$ from the literature.

Label	Survey name	z	$f\sigma_8$	Ref
THF	The First Amendment SN catalog	0.02	0.398 ± 0.065	1
DNM	SFI++ and 2MASS	0.02	0.314 ± 0.048	2
2dF	2 degree field	0.17	0.510 ± 0.060	3
LRG1	Sloan Digital Sky Survey	0.25	0.351 ± 0.058	4
LRG2	Sloan Digital Sky Survey	0.37	0.460 ± 0.038	4
WZ1	WiggleZ	0.22	0.390 ± 0.078	5
WZ2	WiggleZ	0.41	0.428 ± 0.044	5
WZ3	WiggleZ	0.6	0.403 ± 0.036	5
WZ4	WiggleZ	0.78	0.493 ± 0.065	5
VVDS	VIRMOS-VLT Deep Survey	0.77	0.490 ± 0.180	6

(1) [30]; (2) [5]; (3) [76]; (4) [78]; (5) [79]; (6) [74, 76]

$f\sigma_8$ over short spans of z. These degeneracies can be broken when one notes that at high redshifts ($z \sim 1000$), $\Omega_{\rm m}$ is very close to 1. With $\Omega_{\rm m}$ equal to 1 the growth of perturbations are independent of γ since $1^\gamma = 1$. Thus one fixes the amplitude of fluctuations at high redshift which can then be projected using the ΛCDM model, with γ as a free parameter, to the redshifts measured. As a fixed point at high redshift I used the WMAP7+BAO+H_0 parameters $\Omega_{\rm m,0}$ and $\sigma_{8,0}$, noting that $\Omega_{\rm m,0}$ quoted in WMAP7 assumes that $\gamma = 0.55$. To get the true measured WMAP7 amplitude of fluctuations I used ΛCDM ($\gamma = 0.55$) to calculate $\sigma_8(z_{\rm CMB})$ from which other values of γ could be used to predict later times self consistently[following 78, Section 4.5]. Since the WMAP7 parameters have non trivial uncertainties I then use the WMAP7+BAO+H_0 Monte Carlo Markov chains to marginalize over $\Omega_{\rm m,0}$ and $\sigma_{8,0}$. A representative sampling of growth curves of increasing γ are plotted overlaying the same data from Fig. 3.1 to indicate the effect of increasing γ's with 0.50 as the top most curve increasing by 0.05 with each subsequent curve is shown in Fig. 3.2.

The model allows the prediction the value of $f(z) = \Omega_{\rm m}(z)^\gamma$ and $\sigma_8(z)$ at any redshift,

Table 3.2: Measurements of γ from combinations of the data

Sample	γ	$\sigma_{\rm CMB}$	$\sigma_{\rm tot}$
RSD+THF	$0.589^{+0.043}_{-0.041}$	0.071	0.083
RSD+DNM	$0.65^{+0.042}_{-0.040}$	0.072	0.084
All RSD	$0.605^{+0.048}_{-0.045}$	0.075	0.088
All	$\mathbf{0.621^{+0.039}_{-0.036}}$	**0.070**	**0.080**

assuming their values at any fixed redshift such as $z = z_{CMB}$.

For the fits, I use a simple χ^2 statistic with the following form:

$$\chi^2 = \sum_i \frac{[f\sigma_8(\text{meas})_i - f\sigma_8(\text{pred})_i]^2}{\sigma_i^2} \tag{3.2}$$

where the first term is the measured value and the second term is the model, and σ_i^2 is the uncertainty for each measured value.

In Fig 3.3, I show the fits of γ; The four curves differ only in what data points are fit. The dotted curve shows the constraints without any low-z data with a best fit γ of $0.605^{+0.089}_{-0.087}$. The solid curve with data points shown curve shows the constrains with only the [5] data point at low-z with a best fit of $0.630^{+0.084}_{-0.083}$. The solid curve shows the constraints with only the [30] low-z data point with a best fit of $0.598^{+0.083}_{-0.082}$. The dashed curve shows the constraints with both low-z data point simultaneously with a best fit of $0.621^{+0.080}_{-0.079}$. In all four curves, the colours red, green and blue reflect the 68,95, and 99 per cent confidence intervals. The black arrows indicate the values of γ predicted by ΛCDM and DGP braneworld gravity with brane tension respectively. The curves as drawn do not take into account the WMAP7+BAO+H_0 Monte Carlo Markov chains marginalization over $\Omega_{\rm m,0}$ and $\sigma_{8,0}$.

Table 3.2 gives the derived γ measurements for different combination of the $f\sigma_8$ measurements. Also listed are the uncertainties in γ arising from $f\sigma_8$, from the CMB determinations of $\Omega_{\rm m,0}$ and $\sigma_{8,0}$, and the total error. Note that the errors from WMAP+BAO+H_0

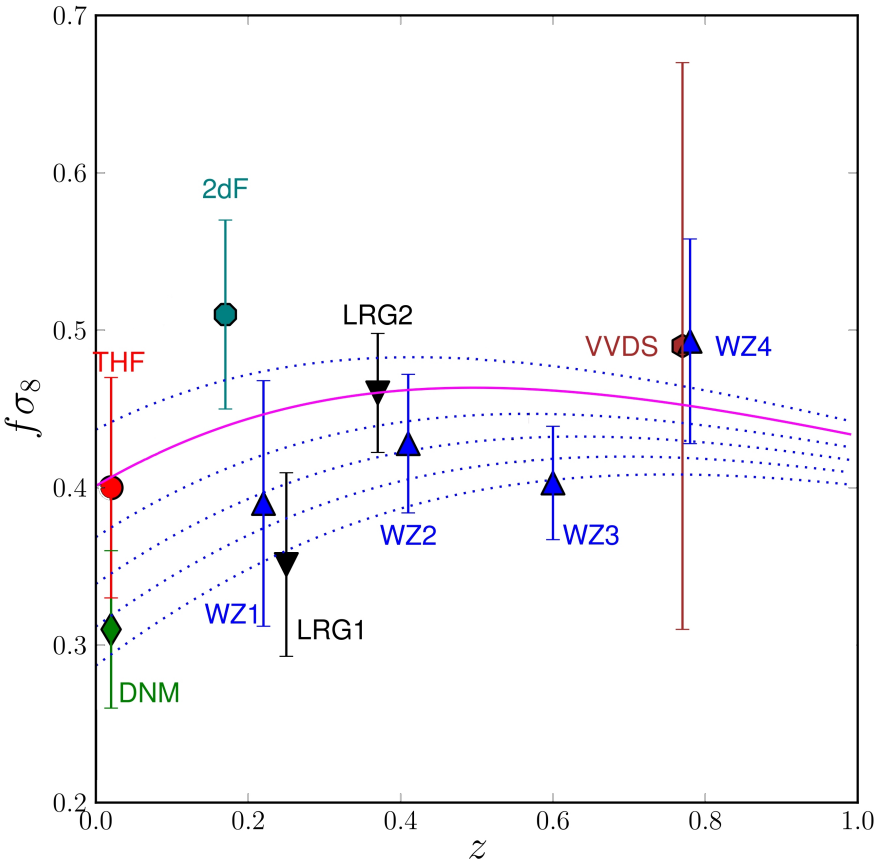

Figure 3.2: Data and symbols are the same as in Fig. 3.1, where the black dashed curve is replaced with dotted curves of different possible γ values. All 5 additional curves are fixed at $\sigma_8(z_{\rm CMB})$ from WMAP7+BAO+H_0 measurements. The topmost of the 6 projections has a γ of 0.50 and each subsequent curve downwards adds 0.05.

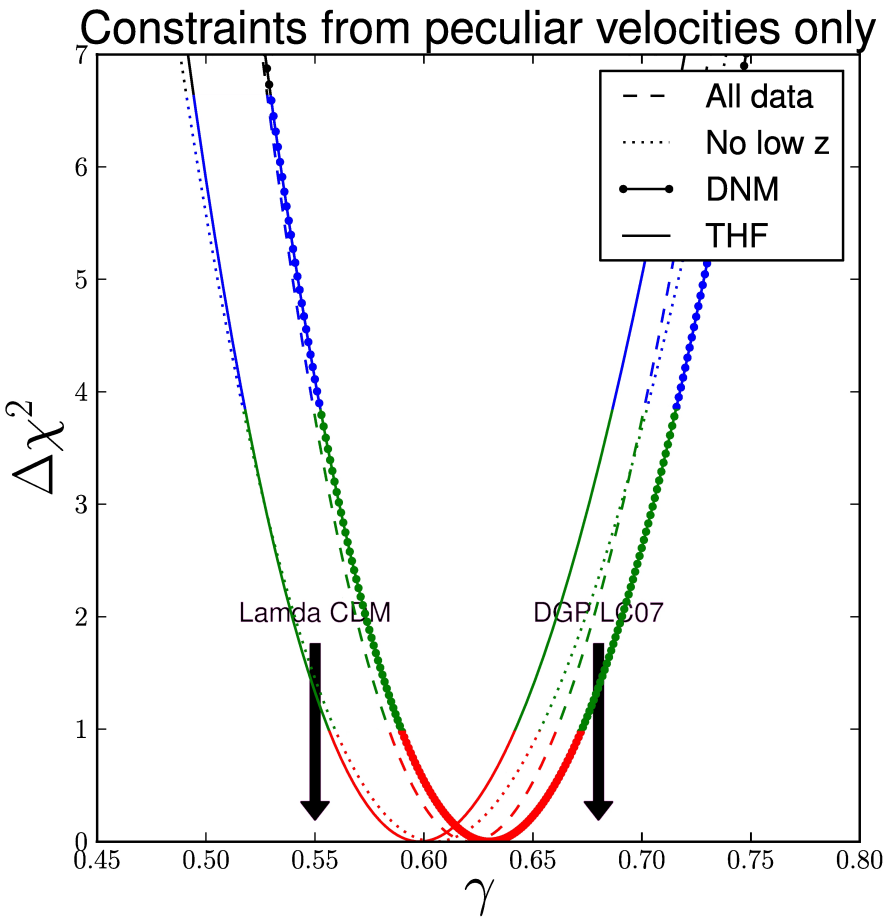

Figure 3.3: 4 χ^2fits for γ for 4 different data subsets. The first data (dashed) set contains all of the data from Table 1.1. The second (dotted) set omits both nearby data points. The third (solid with data points shown) set uses only the [5] low-z data point. The final (solid) fits with only my Chapter 2 results at low -z. The colours represent the different confidence intervals about each minimum solution; the red, green and blue regions corresponding to the 68, 95, and 99 per cent confidences respectively.

are not independent (between one $f\sigma_8$ measurement and another), are weakly dependent on z, and dominate the total error budget when all data are combined. The full combined fit yields 0.621 ± 0.080, consistent with ΛCDM.

Although for purposes of illustration I have focused on a constant scale-independent γ, peculiar velocity data would also allow one to test more complicated modified gravity scenarios [see e.g. the review by 80].

3.4 Conclusion

I have shown that by combining measurements of $f\sigma_8(z)$ at different redshifts, and in particular by including results at $z \sim 0$ from MD surveys, I can break the degeneracy between $\Omega_{\mathrm{m},0}$, $\sigma_{8,0}$ and γ and thus measure γ by comparing measurements of $f\sigma_8(z)$ at low z, after fixing their values at z_{CMB}. The strongest leverage on γ arises from peculiar velocity measurements at the lowest redshifts. By including these measurements, I derive $\gamma = 0.621 \pm 0.080$, consistent with ΛCDM. The Planck mission plus upcoming peculiar velocity and redshift surveys will tighten these constraints further.

Chapter 4

Calibrating and Measuring Systematic Errors in Calculating β

In the next generation of peculiar velocity catalogs the number of tracers is going to grow by a factor of ten or more. Such an increase could reduce the measurement precision due to noise to the level where systematic uncertainties in the methodologies become dominant over random noise. To improve accuracy further, a clear understanding of systematic errors in the methodologies in necessary for calibration and corrections. In this chapter, I therefore systematically explore several avenues by which systematic errors can be introduced by the common tools used in reconstructing β.

4.1 Outline

In Chapter 2, peculiar velocity tracers from SN were compared to predicted peculiar velocities from a pre-existing density reconstruction, mainly the IRAS Point Source Catalog Redshift survey (PSCz) density field reconstructed by [54]. For this Chapter, the goal is to explore and verify the steps taken in measuring β from a peculiar velocity catalog and a redshift-space halo catalog. The limitations of β measuring methods are explored with

N-body simulation where position and velocity are known, and thus reconstructions and predictions can be compared to this 'ideal' sample.

This is not the first time the limits of β reconstruction techniques have been tested with N-body simulations [81, 82], however this work uses a larger simulation box, more particles than previously used and is more comprehensive in the exploration of possible sources of systematic error.

There are many steps in the measurement of β in real data that can accumulate systematic errors. In observations, the redshift catalog used to map the density field is often significantly more densely sampled than the peculiar velocity tracer catalog. One possibility that is commonly overlooked is that the peculiar velocity catalog might introduce systematic error into the measurement of β. Observational redshift catalogs often have a halo mass threshold set by the luminosity limit. To compare N-body results with real observations, it is therefore necessary to extract a group or halo catalog to test for any effects that this observational limitation could have on β measurements. Lastly, the β fitting method itself requires the transformation of a redshift-space halo catalog into a real-space halo catalog, and this 'reconstruction' process may introduce systematic errors of its own.

In this chapter, I first introduce the N-body data set and the basic tools of this analysis: density fields, smoothing, halo catalogs, linear theory predicted peculiar velocity fields, and linear regressions (to quantify agreement between N-body and predicted peculiar velocities); these will be touched upon in subsections 4.2.1, 4.2.2, 4.2.3, and 4.2.4 respectively. In section 4.3, I explore systematic errors that can exist in the ideal case where the real distances to all objects are known. Specifically, I probe whether or not varying subsets of peculiar velocity tracers can introduce systematic error in subsection 4.3.1. In the following subsection, I look at the more direct problem of density tracer systematic error, specifically in the effects of smoothing and halo mass thresholds. I then introduce the distortions caused by switching into redshift space in section 4.4. First, I focus on the raw results in redshift space in subsection 4.4.1, and then I look at the results obtained by iteratively reconstructing real space positions from redshift space positions. Finally I draw

conclusions in section 4.5.

4.2 The N-body Data

To complete this testing I used an N-body simulation, kindly provided by Lavaux, of 512^3 particles in a 500 h^{-1} Mpc periodic box. The simulation is a $\Omega_m = 0.266$, $\Omega_\Lambda = 0.734$, $h = 0.71$, where $H_0/h \equiv 100\,\mathrm{km\ s^{-1}/Mpc}$, and each particle represents $6.83 \times 10^{10}\ h^{-1}$ solar masses. The simulation provided the following: particle position and velocity lists, a halo catalog of 693948 halos between 5.5×10^{11} and $2.2 \times 10^{15}\ h^{-1}$ solar masses (8 and 31809 particles), as well as a 256^3 grid velocity field.

In figure 4.1, I present a slice of the particle density field. This view is useful for visualizing large scale structure. The largest deep red spots are centers of superclusters and the smaller red spots are clusters. A few filaments can also be seen where they happen to travel within the plane rather than directly traversing it. The darkest blue spots are voids.

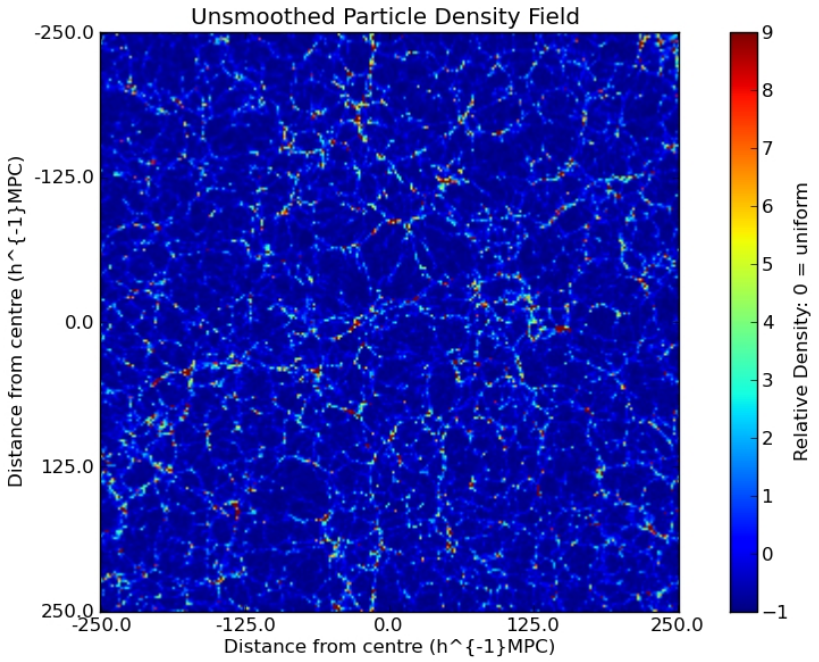

Figure 4.1: A slice from the centre of the particle density field. The density field has been normalized to show density fluctuations: Cells devoid of any particles have the value $\delta = -1$, cells with exactly 8 particles have the value $\delta = 0$, and the whole data set has an overall total of $\delta = 0$. The lack of smoothing permits very high contrast against which large scale structure can be easily identified. Clusters and super-clusters are solid red regions with densities near and above 72 particles per cell ($\delta = 9$) with filaments visible between them.

4.2.1 Smoothed Density Field

There are two problems with figure 4.1. First, the contrast is artificial and the regions which are shown as perfectly void would not be in the real universe[1]. Second, linear perturbation

[1]Consider a center of a large void, and its corresponding peak in the potential energy field. Near the location of the peak, the gradient of the potential field (i.e. the gravitational acceleration or linear theory velocity) will be close to zero. Assuming a near uniform density before the growth of structure, such a

theory breaks down at small scales ($\sigma_r \sim \langle\delta^2\rangle \gtrsim 1$, where σ_r is a generalization of σ_8 for spherical top hat radii other than 8 h^{-1} Mpc). Both problems can be addressed with Gaussian smoothing. In figure 4.2, I show the same slice of this particle density field after it has been smoothed with a 4 h^{-1} Mpc Gaussian[2]. This figure represents all of the mass in the simulation and is the base density field against which all others are compared. As with figure 4.1, the density field has been re-normalized in units of mean density $\bar{\rho}$.

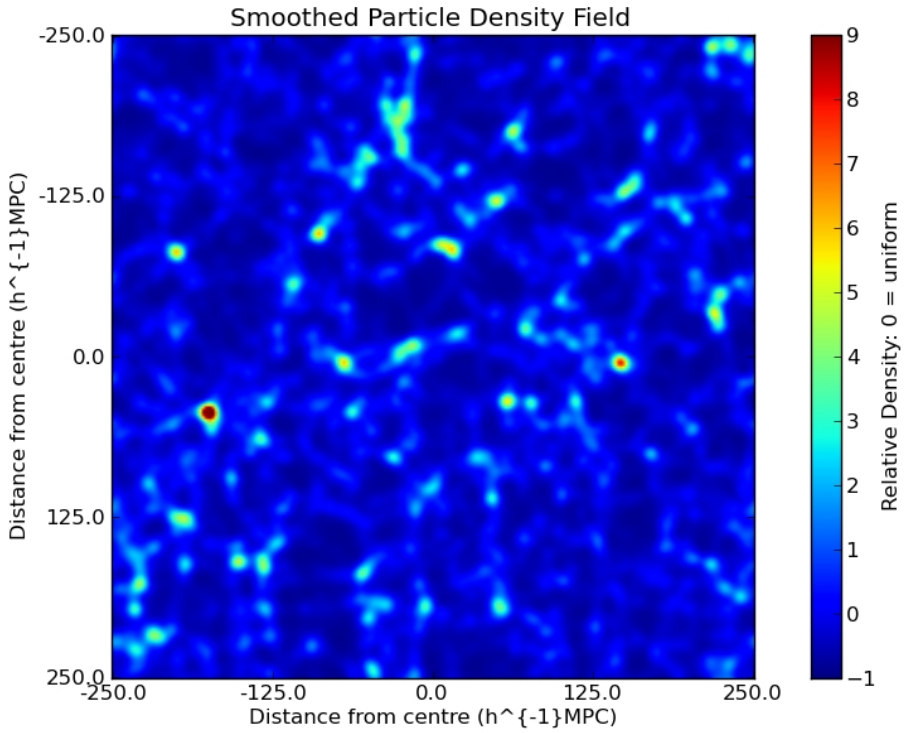

Figure 4.2: The particle density field smoothed with a 4 h^{-1} Mpc Gaussian filter and re-normalized to have an average density contrast, $\delta = \frac{\rho - \bar{\rho}}{\bar{\rho}}$, of 0.

region would have its density decreased only by the expansion of the universe (plus higher order effects from initial momentum and subsequent heating, which would cause individual molecules to be pushed in and out of the region under consideration).

[2]The reason for choosing 4 h^{-1} Mpc is explained in subsection 4.3.2

4.2.2 Halos: Number and Mass Weighting

In real observational data, individual particles are not observable. Rather, galaxies are observed, and these are usually grouped into groups and clusters (referred to collectively as halos). Halos are important in considering density fields because halos contain the additional dark matter of the halo in which the observable galaxies(and associated dark matter halos) are embedded, thus halo are believed to be better tracers of the underlying total matter distribution than galaxies alone. This grouping into halos has an additional feature of removing the 'finger of god' effect of massive structures which is caused by redshift distances being susceptible to line of sight smearing.

The N-body halo catalog contains a mass for each halo. The smallest halos are of 8 particles or masses of $5.5 \times 10^{11} h^{-1} M_{\odot}$[3]. In real data halos will be larger then some threshold but not necessarily $5.5 \times 10^{11} h^{-1} M_{\odot}$ so I introduce a threshold in this work which I can vary and explore the results as a function of. A halo mass threshold can be applied in two subtly different ways: it can be applied to those halos used as velocity tracers (for which I will use the symbol $\mathbb{M}_{\rm TH}^{\rm V}$) or it can be set independently when choosing halos to include for constructing the density field (for which I will use the symbol $\mathbb{M}_{\rm TH}^{\delta}$). Once $\mathbb{M}_{\rm TH}^{\delta}$ is chosen I also have to choose between two possible weighting schemes: using the mass and weighting each halo proportionately (mass weighting) or ignoring the mass and weighting by number density of halos (number weighting).

In Figure 4.3, I present side-by-side the full particle density field (left) and the halo density field where each halo is weighted according to its mass. For ease of interpretation I set $\mathbb{M}_{\rm TH}^{\delta}$to $10^{13}\ h^{-1} M_{\odot}$ in this figure, so only halos with masses larger than $10^{13}\ h^{-1} M_{\odot}$ are included. The halo density field shown is also smoothed with a 4 h^{-1} Mpc Gaussian filter and normalized in the same way as the particle field. The single most dense cell of the mass-weighted density field has a $\delta = 136$, which is 4.3 times larger than the highest relative density cell in the particle density field. Figure 4.4 is identical in construction to

[3]That is $1.8 \times 10^{17} h^{-1}$ times the mass of the earth for each halo. Each particle is $6.83 \times 10^{10}\ h^{-1} M_{\odot}$ ($2.2 \times 10^{16} h^{-1}$ earths, $1.4 \times 10^{41} h^{-1}$ kg, or $7.6 \times 10^{67}\ h^{-1} Gev/c^2$ (VERY cold dark matter indeed)

figure 4.3 except that the halos are number weighted rather than mass weighted. The single highest relative density cell of the mass weighted density field has a $\delta = 20.8$, which is 0.65 times that of the highest relative density cell in the particle density field[4]. It can clearly be seen that the mass weighting scheme makes the peaks much more prominent than in the particle density field, and that both halo models underpopulated voids as expected.

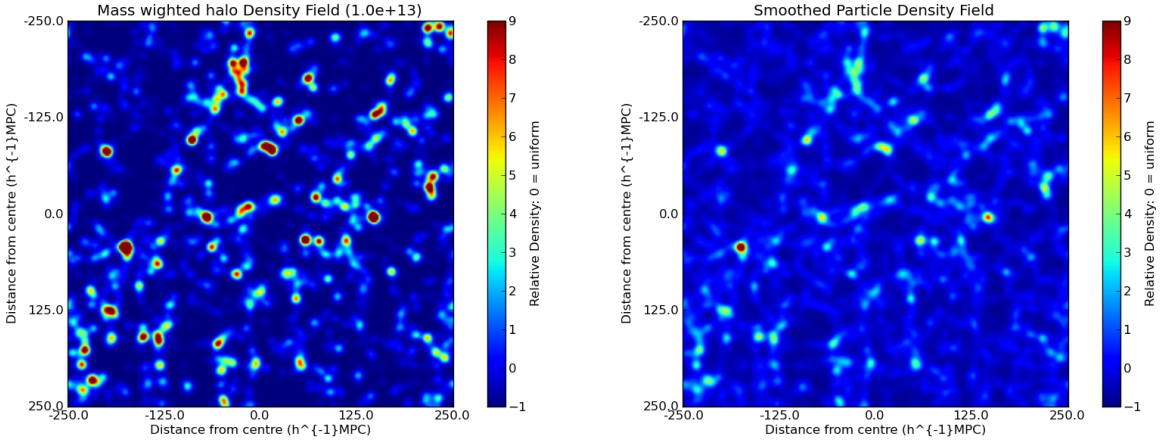

Figure 4.3: On the left: a slice of density field derived with $\mathbb{M}^{\delta}_{\rm TH} = 10^{13}\ h^{-1}M_{\odot}$ where each halo is weighted with a mass proportional to the number of particles in the halo (mass weighted). This is to be compared to figure 4.2 (reproduced on the right). Both fields have been smoothed with a 4 h^{-1} Mpc Gaussian filter and are plotted in density contrast.

[4]The number weighted density field and the all particle density field was not maximized in the same cell (i.e. the cell index for the cell with the largest density fluctuation was different for the two density fields). Comparing the cell index by the highest number weighted density field gives a factor of 1.40. Comparing at the cell index by the highest particle density field gives a factor of 0.26.

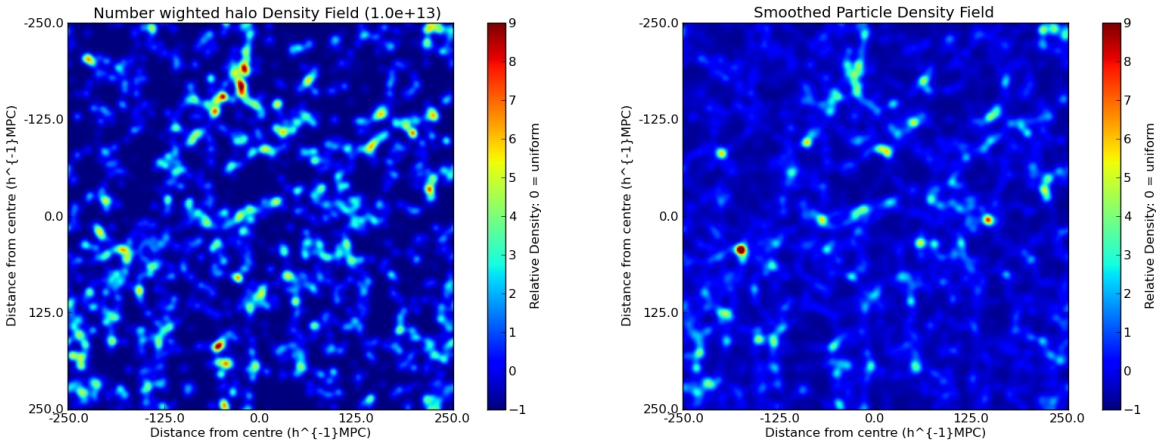

Figure 4.4: Based on the same halos as the figure 4.3 and using the same process. The only difference is that the halos are number weighted rather than mass weighted. $\mathbb{M}^{\delta}_{\rm TH}$ remains at 10^{13} $h^{-1}M_{\odot}$ in this figure.

4.2.3 N-body and Predicted Peculiar Velocity Fields

Once the density fields are derived, linear theory can be applied to produce the corresponding velocity fields using equation 1.5. In Figure 4.5, I show two slices of velocity fields. The left field is the N-body velocity field[5]. The field has been binned but not smoothed after binning. The right field is one of the linear perturbation theory velocity fields. This figure is derived from the full particle density field and smoothed with a 4 h^{-1} Mpc Gaussian. The slices show the y-component of the velocity of a slice taken at constant x, the y-index increasing down the figure, and is transition from positive y-velocity (red, above dense patches from 4.2) to negative y-velocity (blue below), and is consistent with the expectations of gravitational collapse onto the most dense patches. Again many velocity fields were generated for x-, y-, and z-components, different smoothing lengths, and for both mass weighting and number weighting; however the resulting figures do not differ

[5]This figure is included purely for ease of visualization and qualitative comparisons, it is not used in any fits or quantitative analysis

significantly.

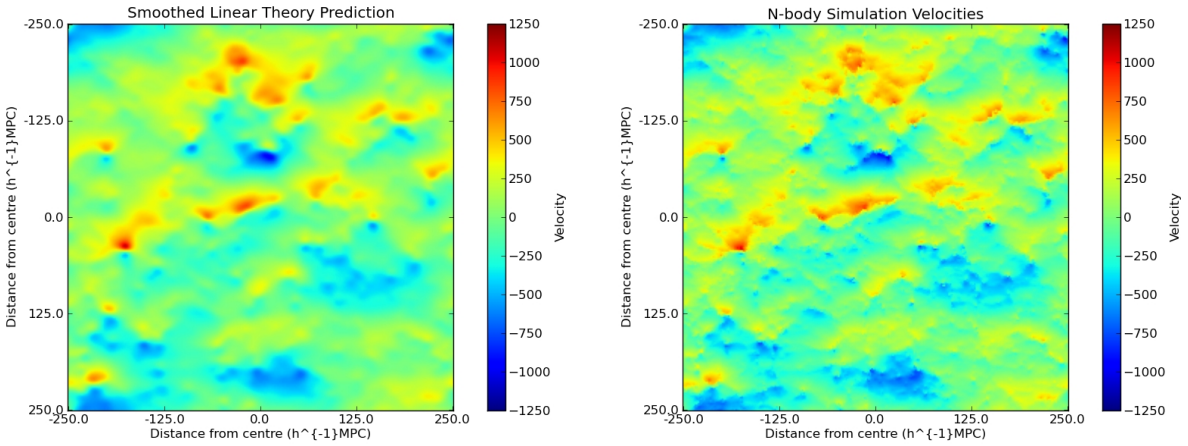

Figure 4.5: Two selected slices of velocity fields for visual comparison. On the left: the velocity field calculated with linear perturbation theory applied to the full particle density field and smoothed with a 4 h^{-1} Mpc Gaussian. On the right: the velocity field directly from the N-body simulation without smoothing after binning. The slice is extracted from the cube at the same x as 4.3 for easy comparison. Both figures are coloured with positive y-velocity shown in red and negative y-velocity shown in blue. Note: the y-index increases from top to bottom in the figure thus the velocities are converging to the high density patches shown in 4.2.

4.2.4 Quantifying the Differences

It is clear that the linear theory and N-body velocity maps in figure 4.5 do not agree perfectly. Specifically, it can be seen that the linear theory map is reaching deeper colours than the N-body velocity map and that the N-body velocity map is not smoothed (thus it is more structured than the linear theory prediction). In order to draw any conclusions, I need to quantify the differences between N-body known velocities and prediction. As mentioned above the N-body velocity map from 4.5 is a visual aid; however in general measured peculiar velocities are not smoothed onto a grid when measuring β or reconstructing density

fields. Instead, N-body 'measured' peculiar velocities are compared to the cloud-in-cell predicted peculiar velocity for the corresponding particle location. In these comparisons, I am interested in two quantities: the slope of the linear regression of 'measured' velocity onto predicted velocity (a β estimator), and the scatter around that linear regression. The interpretation of the slope depends on the density field used to predict the velocity field.

In figure 4.6, I present a direct comparison between the N-body particle velocities and the linear theory predictions for the full particle density field smoothed with a 4 h^{-1} Mpc Gaussian. If linear theory were perfect then the best fit line would be unity with no scatter. The red line is a best fit to this data and has a regression slope of 0.950. When the slope of the best fit line differs from unity the deviation, this is attributed to systematic errors in the method stemming from differing smoothing lengths. Similarly, in figure 4.7,

I present the comparison using halos instead of particles. Specifically in this second comparison, the underlying density field is the density field derived with $\mathbb{M}^{\delta}_{\rm TH} = 5.5 \times 10^{11}$ $h^{-1}M_{\odot}$[6] and the comparison is made with $\mathbb{M}^{\rm V}_{\rm TH}$ also equal to 5.5×10^{11} $h^{-1}M_{\odot}$[7]. When halo density tracers are used, the slope is interpreted slightly differently as being $\frac{1}{b_{tr}}$, where b_{tr} is the linear bias factor between the tracers used to predict the velocity and the true density (as discussed in the comparisons section of Chapter 2 and the introduction of Chapter 3). In this case the slope was 0.9686, which corresponds to a b_{tr} of 1.03[8].

It is worth noting that the scatter for the peculiar velocity tracers sampled at halo locations is significantly smaller than the tracers sampled at all particle locations. The particle peculiar velocity tracers scatter is greater by approximately 180 km s^{-1}added in quadrature.

[6]This choice of $\mathbb{M}^{\delta}_{\rm TH}$ corresponds to all halos in the halo catalog

[7]This means that the velocities of all the N-body halos are compared to the predictions

[8]It should be noted that when all particles are used it is equivalent to using a $\mathbb{M}^{\delta}_{\rm TH}$ of 6.8×10^{10} $h^{-1}M_{\odot}$. At this lower $\mathbb{M}^{\delta}_{\rm TH}$ the slope was 0.950. If one considers the full particle field to be unbiased by definition ($\mathbb{M}^{\delta}_{\rm TH} = 6.8 \times 10^{10}$ $h^{-1}M_{\odot} \sim \mathbb{M}^{\delta}_{\rm TH}$ =0) then the bias is $\frac{0.9686}{0.950}$ or 1.020. For simplicity I shall neglect the factor of $\frac{1}{0.950}$, to compensate increase all quoted biases by 5.3%

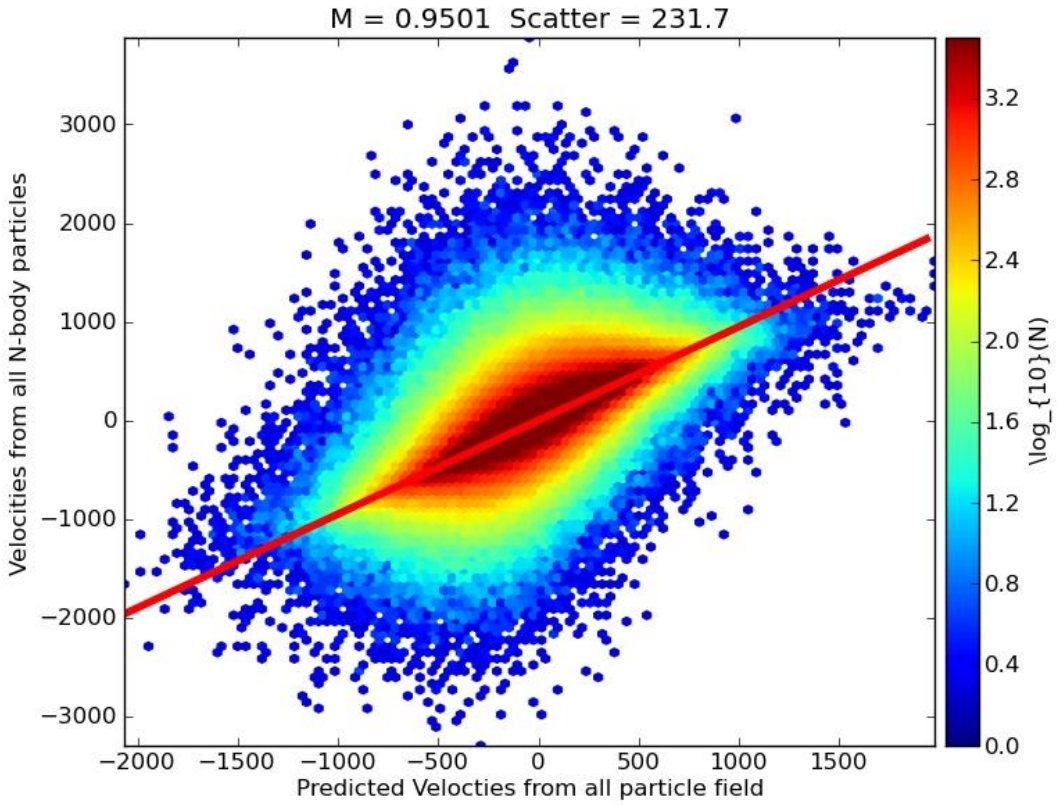

Figure 4.6: A regression of the N-body particle velocities onto predicted velocities derived from linear theory and the complete particle density map, smoothed with a 4 h^{-1} Mpc Gaussian. The least squared line of best fit is plotted and in this figure the slope was found to be 0.9501. In similar figures where the full particle density field is used but the smoothing length is varied, the deviation from unity is attributed to the systematic errors due to linear theory and smoothing.

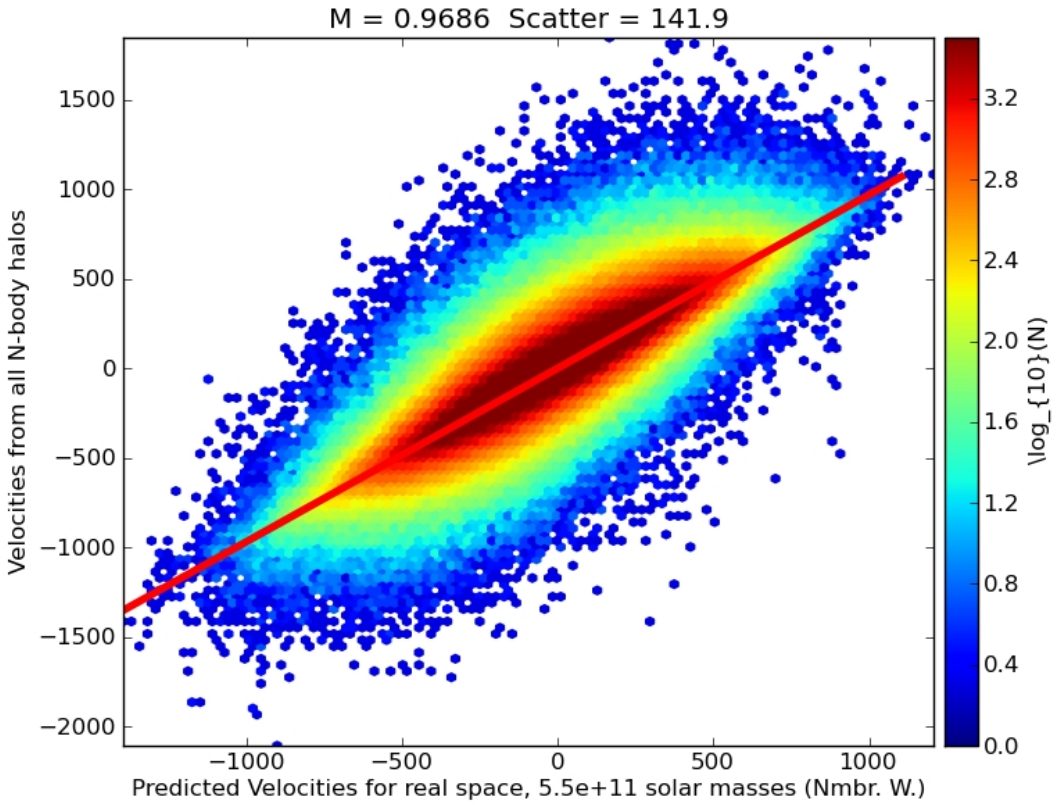

Figure 4.7: Same as 4.6 above except here both $\mathbb{M}_{\rm TH}^{\delta}$ and $\mathbb{M}_{\rm TH}^{\rm V}$ have been changed to $5.5 \times 10^{11}\ h^{-1}M_{\odot}$. The observed N-body velocities are plotted on the y-axis and the predictions for the same halos are predicted from the halo density field shown in figure 4.3 (which is smoothed with a $4\ h^{-1}$ Mpc Gaussian, and the halos are number weighted). Here the resulting regression slope was found to be 0.9686. The interpretation of the slope is different from 4.6 because a halo catalog is being used to generate the predictions. In this situation the slope is equal to $\frac{1}{b_{th}}$, meaning that $b = 1.03$ for this density tracer.

4.3 Real Space Systematic Error Sources

With N-body simulations the real distances to particles and halos are known which means that the density field is accurate, unlike in observational data where the real distances must be reconstructed from redshift distances. As a first step, it is important to identify what sources of systematic error can exist even when the true distances to objects are known. In this section, I test for systematic errors in the peculiar velocity tracers (by changing mass $\mathbb{M}^{\mathrm{V}}_{\mathrm{TH}}$ while keeping $\mathbb{M}^{\delta}_{\mathrm{TH}}$ fixed), error due to different smoothing lengths (keeping $\mathbb{M}^{\delta}_{\mathrm{TH}}$ fixed), and error due to changing $\mathbb{M}^{\delta}_{\mathrm{TH}}$ (keeping the $\mathbb{M}^{\mathrm{V}}_{\mathrm{TH}}$ fixed).

4.3.1 Peculiar Velocity Tracers

In real data, the halos used to trace the peculiar velocity field will all be above a given $\mathbb{M}^{\mathrm{V}}_{\mathrm{TH}}$. A higher $\mathbb{M}^{\mathrm{V}}_{\mathrm{TH}}$ means fewer sampling tracer points for comparisons. One might expect that a lower mass $\mathbb{M}^{\mathrm{V}}_{\mathrm{TH}}$ (for a fixed $\mathbb{M}^{\delta}_{\mathrm{TH}}$) would allow for more peculiar velocity sampling points, which in turn should reduce the uncertainty of the final measured slopes by a factor of $\sqrt{N}$. This is only true when the sampling points are uncorrelated, which is untrue for predictions for pairs of tracer points that are in close proximity. Further, the N-body velocities from the same close proximity particles may have very different values if the particles in question are in a halo where non-linear effects dominate[9]. The fact that the predictions can be correlated while the N-body results are uncorrelated, for given pair of particles or halos, leaves room for systematic errors which change as a function of $\mathbb{M}^{\mathrm{V}}_{\mathrm{TH}}$.

Clearly this peculiar velocity tracer sensitivity to correlations will affect the scatter around a regression fit, but it is less clear what effect it would have on the slope of the regression fit. There are two possibilities that I would like to present. Firstly, if one assumed that the largest halos were precisely at the centre of their respective potential

[9]See Figures 4.6 and 4.7 where the scatter changes significantly with the change of tracer, noting that the underlying density field is also changed so not all the scatter change is necessarily due to a change in chosen tracers

wells then one would conclude that such a collection of tracers would have no scatter or systematic deviation from linear theory since they would not experience the effects of small-scale power where linear theory breaks down. Peculiar velocity halos chosen over a given $\mathbb{M}_{\rm TH}^{\rm V}$ will not be precisely at the bottom of their respective wells and thus they are somewhat susceptible to the tendency for linear theory to over-prediction of velocities in high density regions, although one would expect this effect to be quite small. Secondly, for large halos there is a second implicit smoothing length given by the halo mass which should be considered. A halo of a given mass can be thought of as having collapsed from a much larger volume of uniform density. Thus halos have a smoothing length associated with this volume of uniform density material before it collapsed. If this implicit smoothing length is larger than the smoothing length applied to the density field used in the predictions of the velocity field, then systematic errors in measuring the slope and scatter can result. Theses two possible sources of systematic error would be difficult to differentiate and to do so would require changing both the $\mathbb{M}_{\rm TH}^{\rm V}$ and the density field smoothing length; a test which was not performed.

In Figure 4.8, I test the effect of peculiar velocity halo sampling on the scatter about the linear regression fits of N-body halo velocities onto predicted velocities derived from the all particle density field smoothed with a 4 h^{-1} Mpc Gaussian. A clear trend of decreasing scatter with higher $\mathbb{M}_{\rm TH}^{\rm V}$ can be seen except at the very highest $\mathbb{M}_{\rm TH}^{\rm V}$ where it starts to rise again. In Figure 4.9, I present the corresponding slopes as a function of mass calculated from the same regressions as the results in Figure 4.8. There is a slight trend at $\mathbb{M}_{\rm TH}^{\rm V}$ 10^{12} $h^{-1}M_{\odot}$, which gets quite steep beyond 10^{13} $h^{-1}M_{\odot}$, towards lower measured slopes. It is unclear what the dominant cause for this steepening is, see the previous paragraph for discussion of possibilities.

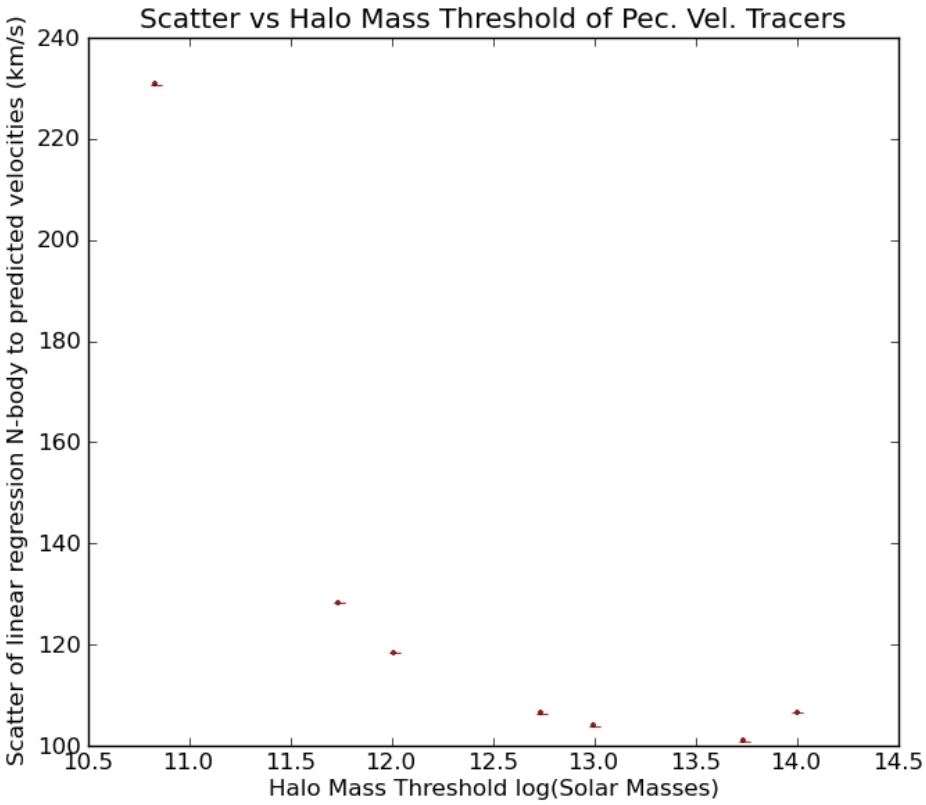

Figure 4.8: The scatter in velocity about the regression between N-body observed peculiar velocities sampled at locations of halos (above an increasing $\mathbb{M}_{\rm TH}^{\rm V}$) and the linear theory predictions based on the all particle density field smoothed with a 4 h^{-1} Mpc Gaussian.

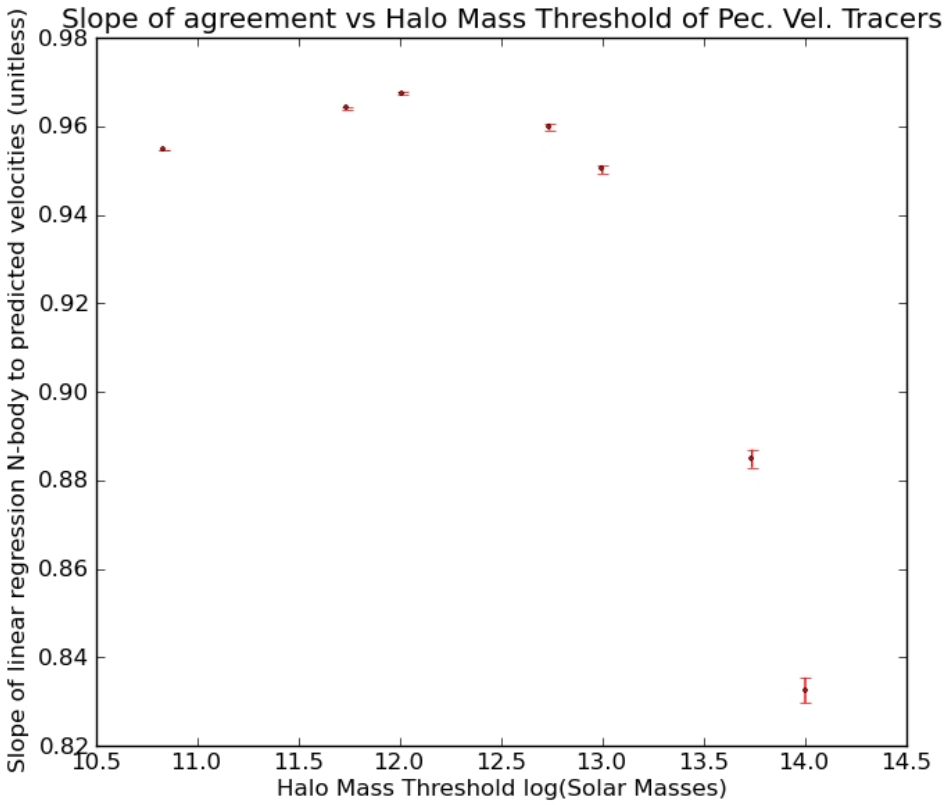

Figure 4.9: Using the same process as figure 4.8 above, I present the slope of the same regressions shown in figure 4.8.

4.3.2 Density Tracers

In this section, I will explore the result of changing the density field from which the predicted peculiar velocities are derived.

In subsection 4.2.1, I introduced smoothing and explained why it was necessary. In this section, I will define what smoothing length is best for β studies by charting the change in the resulting slopes and scatters from the comparison of N-body velocities against linear theory predictions as a function of the smoothing length. Too small a smoothing length

permits excess non-linear "noise" and sensitivity to the breakdown of linear theory at small scales, while too long a smoothing length and the smoothed density field becomes much more uniform (lower δ) than the real data and predicted velocities become suppressed.

The other possible source of systematic error is to change $\mathbb{M}^{\delta}_{\rm TH}$ (rather than $\mathbb{M}^{\rm V}_{\rm TH}$, which was explored above). I extract slopes and scatters for density fields derived for $\mathbb{M}^{\delta}_{\rm TH}$ between 5.5×10^{11} and 10^{14} $h^{-1}M_{\odot}$. I also check for the side effects of under-sampling a density field by holding $\mathbb{M}^{\delta}_{\rm TH}$ constant but re-sampling the field randomly and keeping only some of the halos. If $\mathbb{M}^{\delta}_{\rm TH}$ is too high, then the density field becomes randomly sampled, and this can increase scatter and noise.

Effect of Smoothing

The next goal is to confirm Berlind's work on comparing smoothed peculiar velocity predictions to unsmoothed measurements [82]. To do so, I generate a velocity field from the particle data and then smooth it with a progressively larger Gaussian smoothing kernel. In figure 4.10, I plot the recovered linear regression slopes from plots similar to Fig. 4.6 (the N-body velocities on the vertical axis and the theory predicted velocities from the full particle field on the horizontal axis) as a function of smoothing length. The square symbols are derived by comparing N-body velocity to predicted velocity at every particle position and the circular symbols are compared at N-body halo velocities and locations ($\mathbb{M}^{\rm V}_{\rm TH}$ of 5.5×10^{11} $h^{-1}M_{\odot}$). Both curves reach a slope of 1, ie. unbiased, at a smoothing length of $\sim$4.5 - 4.750 h^{-1}Mpc.

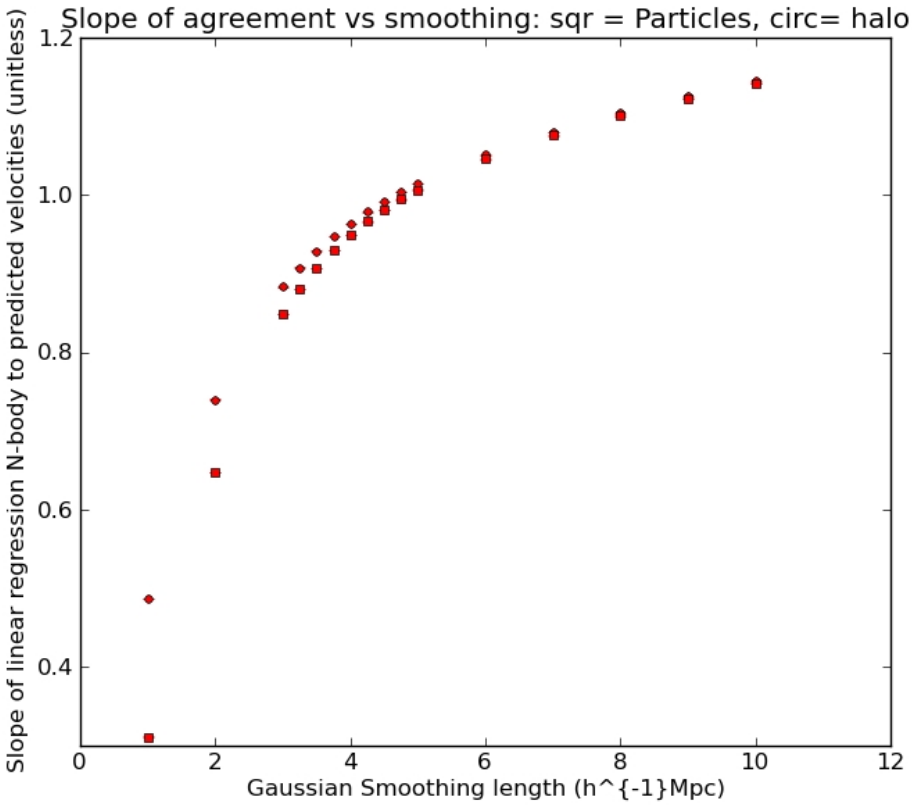

Figure 4.10: The slopes of the regression between N-body observed peculiar velocities and the linear theory predictions based on the full particle field smoothed at increasing Gaussian smoothing lengths. The square symbols are derived by comparing results for every particle and the circular symbols are comparing results for each halo from the halo catalog ($\mathbb{M}^{\rm V}_{\rm TH}$ of $5.5 \times 10^{11}\ h^{-1}M_{\odot}$).

In figure 4.11, I plot the recovered scatter about the linear regression line from the plot similar to 4.6 as a function of smoothing length. The circular symbols compare results for each halo from the halo catalog ($\mathbb{M}^{\rm V}_{\rm TH}$ of $5.5 \times 10^{11}\ h^{-1}M_{\odot}$) and the square symbols compare results at the location of all particles ($\mathbb{M}^{\rm V}_{\rm TH}$ of $6.8 \times 10^{10}\ h^{-1}M_{\odot}$ or 1 particle). The resulting curves have a minimal scatter between 3.5 and 4.0 h^{-1}Mpc (halo results nearer to 3.5, particle results nearer to 4.0).

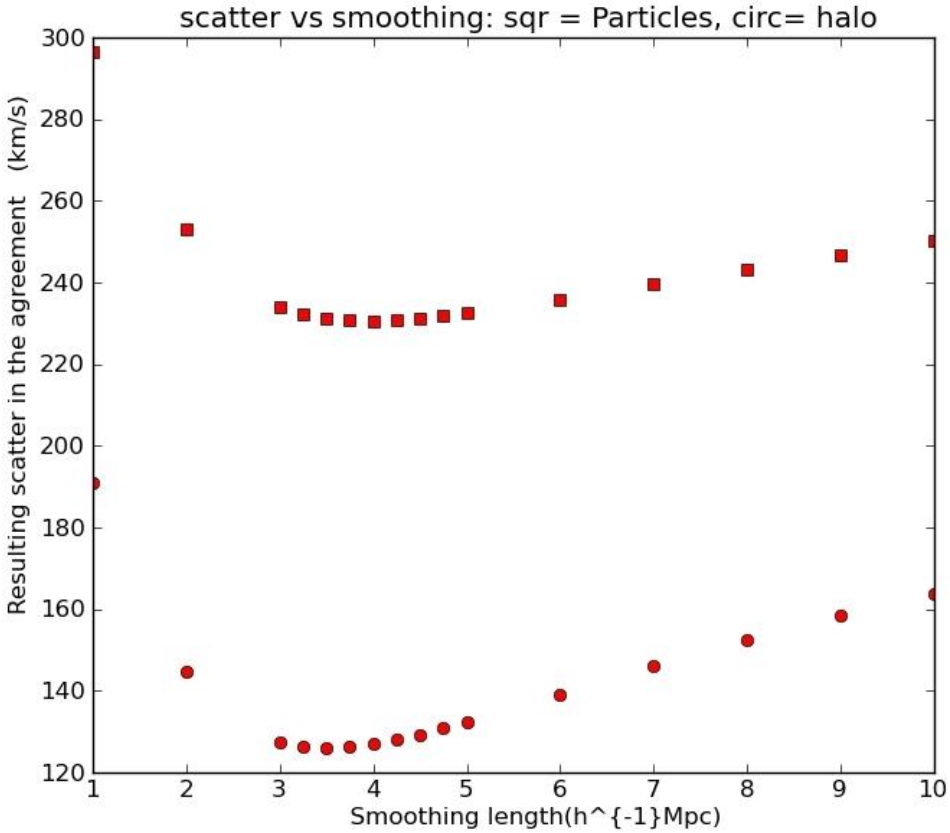

Figure 4.11: Using the same process, symbols, and colours as figure 4.10 above; I present the scatter in velocity about the best fit line as a function of Gaussian smoothing length.

In summary, I find that for both halo and particle position peculiar velocity tracers, the recovered slope is unity between ∼4.5 and 4.75 h^{-1} Mpc and that the scatter also minimizes between ∼3.5 and 4.0 h^{-1} Mpc. To accommodate both an unbiased slope and a slow scatter I use a smoothing length of 4.0 h^{-1} Mpc as the "default" smoothing length in all figures unless otherwise stated.

Table 4.1: Confirming the effect of $\mathbb{M}^{\delta}_{\rm TH}$ on the linear bias

Mass ($h^{-1}M_{\odot}$)	Slope	Bias	Scatter	Halo Count
6.8 $\times 10^{10}$, all Particles	0.950	1.05	232	512^3
5.5 $\times 10^{11}$, Nmbr. weighting	0.969	1.03	142	693948
1.0 $\times 10^{12}$, Nmbr. weighting	0.963	1.04	152	359557
5.5 $\times 10^{12}$, Nmbr. weighting	0.738	1.36	159	92508
1.0 $\times 10^{13}$, Nmbr. weighting	0.629	1.59	160	53066
5.5 $\times 10^{13}$, Nmbr. weighting	0.329	3.04	176	8147
1.0 $\times 10^{14}$, Nmbr. weighting	0.223	4.49	192	3576
5.5 $\times 10^{11}$, mass weighting	0.510	1.96	140	693948
1.0 $\times 10^{12}$, mass weighting	0.489	2.04	141	359557
5.5 $\times 10^{12}$, mass weighting	0.418	2.39	146	92508
1.0 $\times 10^{13}$, mass weighting	0.379	2.64	150	53066
5.5 $\times 10^{13}$, mass weighting	0.229	4.36	177	8147
1.0 $\times 10^{14}$, mass weighting	0.166	6.02	196	3576

Effect of $\mathbb{M}^{\delta}_{\rm TH}$

In subsection 4.3.1 above, I discuss the first of two possible effects of a halo mass thresholds. The second possible effect of a mass threshold comes from applying the halo mass threshold cut when generating the density field (adjusting $\mathbb{M}^{\delta}_{\rm TH}$). Here the different $\mathbb{M}^{\delta}_{\rm TH}$ reflect the different tracers being used, thus the change in slope is actually a change in the effective linear biasing parameter b_{th} since the tracers are being changed. To judge the effect that $\mathbb{M}^{\delta}_{\rm TH}$ has on the recovered slope, I calculate the density field and predicted velocity fields with several different $\mathbb{M}^{\delta}_{\rm TH}$s. I also repeat this with halos weighted with number weighting and with mass weighting. In all results in this section and all following sections $\mathbb{M}^{\rm V}_{\rm TH}$ is held fixed at $5.5 \times 10^{11}\ h^{-1}M_{\odot}$. The results are summarized in table 4.1.

In table 4.1, three properties are changing at once, despite the fact that changes are only

made to two properties: the $\mathbb{M}^{\delta}_{\rm TH}$ parameter and the weighting scheme (number weighting or mass weighting). Changing $\mathbb{M}^{\delta}_{\rm TH}$ actually changes two properties of the density field: the underlying linear bias and the halo tracer number density. Consider the extreme case where $\mathbb{M}^{\delta}_{\rm TH}$ is raised until only one halo remains. In that case, the resulting 'density field' would have some 'true' bias from the full particle density field but the regression would be incapable of measuring that bias due to the noise induced by insufficient spacial sampling. To explore the halo tracer number density problem independently of $\mathbb{M}^{\delta}_{\rm TH}$, I re-sampled each halo catalog, and randomly remove at each $\mathbb{M}^{\delta}_{\rm TH}$ some of the halos from the catalog. At each re-sampling I retain the same number of halos as the next higher $\mathbb{M}^{\delta}_{\rm TH}$. The net effect is that the underlying bias does not change, since the $\mathbb{M}^{\delta}_{\rm TH}$ has been held fixed, and the effect of the increased noise from decreased sampling can be explored directly[10].

In table 4.2, I summarize these results; note that no re-sampling of the $1.0\times10^{14}\ h^{-1}M_{\odot}$ was performed as no higher $\mathbb{M}^{\delta}_{\rm TH}$ existed and the re-sampling of the particle field was also not performed. Each line of table 4.2 has the same underlying bias as the equivalent line in table 4.1 but with only as many density tracers as the subsequent line. To see what fraction of the increase between two mass $\mathbb{M}^{\delta}_{\rm TH}$ lines of table 4.1 is due to insufficient tracers, compare the slope to the slope of the next lower $\mathbb{M}^{\delta}_{\rm TH}$ of table 4.2 [11].

For both tables 4.1 and 4.2 the tests were performed with $\mathbb{M}^{\rm V}_{\rm TH}$ fixed to isolate the effect of changing the density tracers.

[10]Note this re-sampling is to be taken as an approximation. Ideally the re-sampling process would be repeated several times and averaged in a form of bootstrapping, especially in the mass weighting cases where dropping the heaviest halos could significantly alter the resulting density field given the low halo count

[11]For example: at $\mathbb{M}^{\delta}_{\rm TH}$ of $10^{13}\ h^{-1}M_{\odot}$ the bias has increased from 1.35 to 1.58 in table 4.1. but in table 4.2, the $\mathbb{M}^{\delta}_{\rm TH}$ of $5.5\times10^{12}h^{-1}M_{\odot}$ has a similar number of tracers as table 4.1's line for 10^{13} which has a bias of 1.48. Thus of the 0.23 change in slope, $\sim$0.13 is due to loss of resolution, and the remainder is due to the underlying change in bias

Table 4.2: Exploring the effect of reduced sampling at a fixed $\mathbb{M}^{\delta}_{\rm TH}$.

Mass ($h^{-1}M_{\odot}$)	Slope	Bias	$\frac{Bias_{sparse}}{Bias_{full}}$	$\frac{Bias_{Hi.Thres.}}{Bias_{SameThres.}}$	Scatter	Halo Count
5.5 $\times 10^{11}$, Nmbr. W.	0.945	1.06	1.03	1.01	147	359539
1.0 $\times 10^{12}$, Nmbr. W.	0.813	1.23	1.18	1.31	177	92374
5.5 $\times 10^{12}$, Nmbr. W.	0.677	1.49	1.10	1.17	177	53106
1.0 $\times 10^{13}$, Nmbr. W.	0.303	3.30	2.08	1.92	237	8199
5.5 $\times 10^{13}$, Nmbr. W.	0.215	4.65	1.53	1.48	221	3555
5.5 $\times 10^{11}$, mass W.	0.403	2.48	1.27	1.04	182	$\sim$359557
1.0 $\times 10^{12}$, mass W.	0.248	4.04	1.98	1.17	224	$\sim$92508
5.5 $\times 10^{12}$, mass W.	0.329	3.04	1.27	1.10	183	$\sim$53066
1.0 $\times 10^{13}$, mass W.	0.125	8.00	3.03	1.65	250	$\sim$8147
5.5 $\times 10^{13}$, mass W.	0.130	7.69	1.76	1.38	230	$\sim$3576

4.4 Redshift Space and its Systematic Errors

These tests are necessary because peculiar velocities are added with real-space positions which results in redshift positions, and from these redshift positions real-space positions must be reconstructed. To test the reconstruction method I constructed a redshift catalog. The redshift catalog was generated by assuming a fixed observer with no co-moving velocity at the center of the simulated volume. In Figure 4.12, I present the real space and redshift space densities of halos extracted from the center plane of the data cube (all the distortions are radial and thus most visible along the central axis). The halos here are number weighted rather than mass weighted and the field has been smoothed with a 4 h^{-1} Mpc Gaussian filter. Since the differences are subtle, for clarity I include figure 4.13 which shows the difference between the two figures in 4.12.

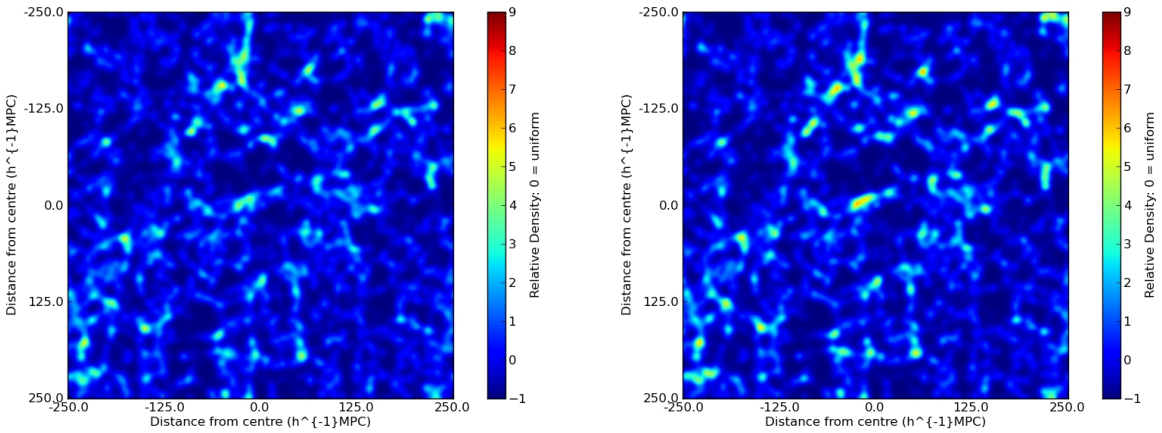

Figure 4.12: A side-by-side halo density comparison of co-moving locations and resulting redshifts. On the left is the co-moving density field using number weighting (i.e. with all halos at their correct distances $H_0 r$). On the right are the same halos and weights after being moved to their respective redshift positions as observed by a stationary observer (zero co-moving velocity) at the center of the simulation(i.e. with all halos at their redshift distances cz).

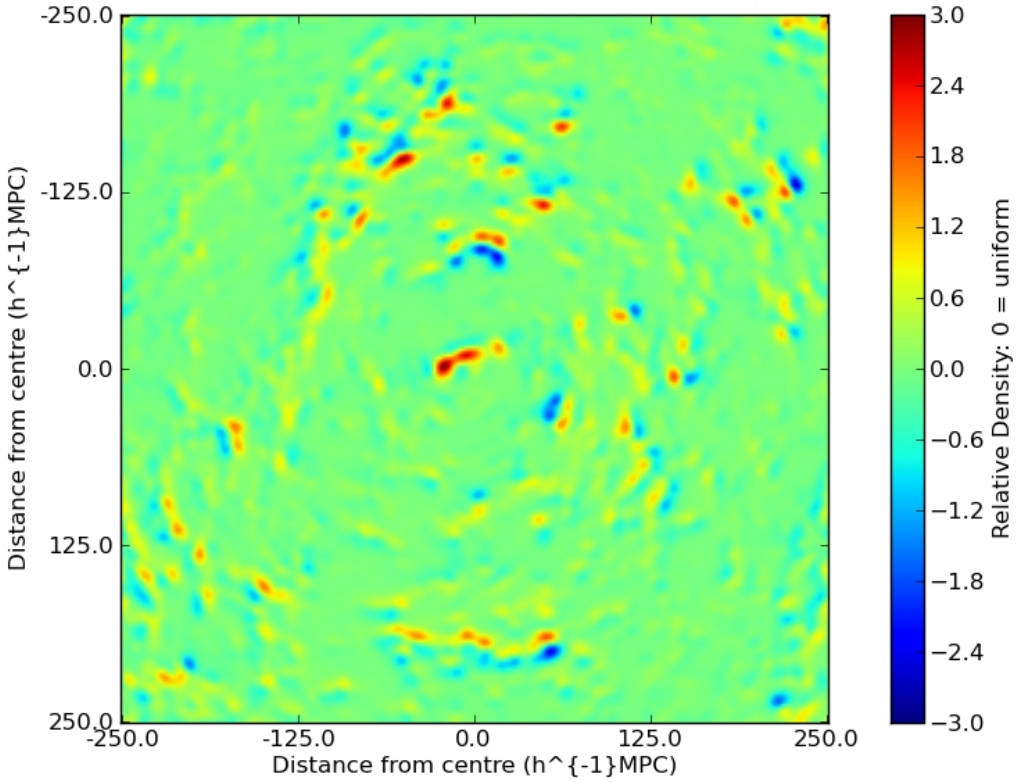

Figure 4.13: The difference between the left and right images of figure 4.12 is presented here for more easy identification. Note: The scale has been reduced to the range -3 to 3.

4.4.1 Fits in Redshift Space

In Figure 4.14, I present the real space and redshift space linear regression fits derived from a density field of all halos over $5.5 \times 10^{10}\ h^{-1}M_{\odot}$ with number weighting. On the left is the fit in real space positions and on the right is the same fit in 'redshift space' where the location of each halo is updated with the projection of its N-body velocity. In real space, the slope is very close to unity ($\frac{1}{b_{th}} = 0.975$ or $b_{th} = 1.03$), but in redshift space the slope decreases significantly ($\frac{1}{b_{th}} = 0.762$ or $b_{th} = 1.31$). The scatter changes from 141 km s^{-1}in real space to 172 km s^{-1} in redshift space. The slope increases when objects move into

'redshift space' because the velocity of halos is falling towards nearby structure, which puts those halos closer to the structure when moved into redshift space. This shift closer to large structure increases the density of those large structures and increases the contrast, which in turn increases the predicted velocities and corresponding bias. The scatter increases firstly because halos have been displaced from their proper locations, but even more so when halos are near enough to a large structure to have a velocity high enough that in redshift space they appear to be on the other side of the attracting body.

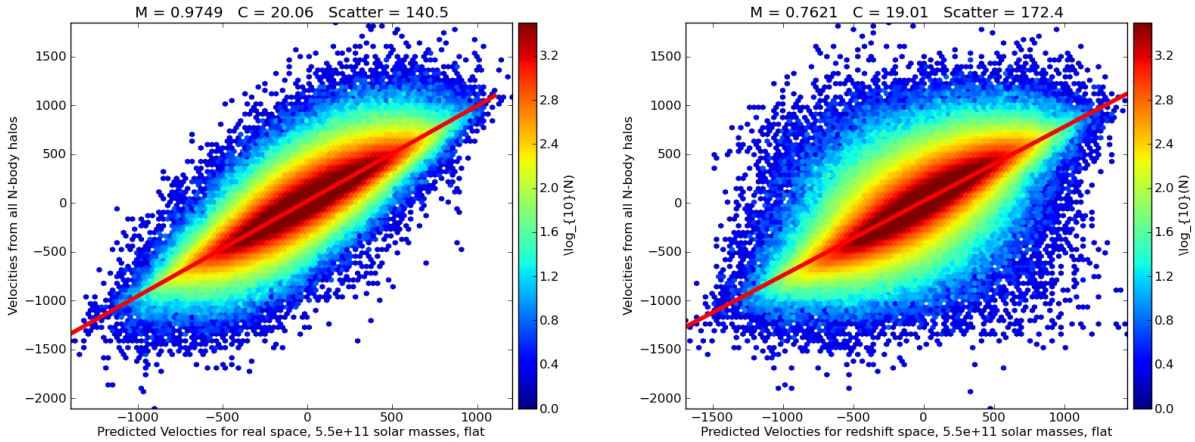

Figure 4.14: A side-by-side comparison of a regression from N-body halo velocities onto predicted peculiar velocities before and after the density field tracers are moved into redshift space. On the left is the fit derived from the co-moving density field with a $\mathbb{M}^{\delta}_{\rm TH}$ of 5.5×10^{10} $h^{-1}M_{\odot}$ and number weighting. On the right are the same halos and weights after being moved to their respective redshift positions as observed by a stationary observer (zero co-moving velocity) at the center of the simulation.

4.4.2 Systematic Error in Iterative Reconstructions

In this section, I will first introduce and explain the iterative method for reconstructing a real density field from the redshift space density field. I will then briefly present the motions which halos undergo during the reconstruction process. I will draw attention

to the evolution of scatter and slope of linear regression fits with a $\mathbb{M}^{\delta}_{\rm TH}$ of 5.5×10^{10} $h^{-1}M_{\odot}$ and number weighting density field as it is reconstructed, and explore the sources of systematic error that result. I will conclude this section explaining why the first three points of the reconstructions have to be done with a higher resolution, and discuss briefly the resolution requirements of the reconstruction method.

Method of Reconstruction

The heart of this reconstruction process is the iterative position correction introduced first by Yahil *et. al.*[83]. Looking at equation 1.9, it is easy to see that it can be re-arranged to

$$H_0 r = cz - v_{pec}(r) \tag{4.1}$$

where cz is the redshift distance, r is the real distance which I would like to recover, and $v_{\rm pec}(r)$ is the predicted velocity at a given location and for a given density field. If the location of the halo in question changes or the density field changes, then $v_{\rm pec}(r)$ also changes. However, as shown in figure 4.14 and 4.12, the density and bias rise when shifting into redshift space, so the result is that the predicted $\mathbf{v}_{\rm pec}(\mathbf{r})$ term will be too large and the halos overshoot their original locations. One could re-apply equation 4.1 repeatedly but there is no guarantee that the solutions will converge. Instead one can alter equation 1.6 from Chapter 1 to

$$\mathbf{v}(\mathbf{r}, T)_{\rm tns} = \frac{T H_o f}{4\pi} \int_0^{\infty} d^3\mathbf{r}' \frac{\delta_{tr}(\mathbf{r}')(\mathbf{r}' - \mathbf{r})}{|\mathbf{r}' - \mathbf{r}|^3} \tag{4.2}$$

where T is a 'transition factor' between redshift space position and reconstructed real space position (which starts at 0 and increases adiabatically to $\frac{f}{b_{th}}$ over subsequent iterations[12]). Then alter equation 4.1 to

$$H_0 r_n = cz - v_{\rm pec}(r_{n-1}) \tag{4.3}$$

[12]In observational experiments, $\beta = \frac{f}{b_{th}}$, is unknown so $\mathbf{v}(\mathbf{r}, \beta)_{\rm tns}$ is iterated instead of $\mathbf{v}(r, T)_{\rm tns}$, and the resulting predicted velocity maps for each iteration step are compared to a peculiar velocity catalog

where at each iterative step n the new positions are calculated from the observed redshift $c\mathbf{z}$ and the predictions derived from the density field resulting from the $n-1$ iteration. I introduce the 'transition factor' T so that any systematic error introduced by the iterative process can be explored and calibrated. I also extend T to beyond $\frac{1}{b_{th}}$ in my plots to observe any pathologies that could affect observational experiments where $\frac{f}{b_{th}}$ is not known from a N-body simulation. The iterations are performed by calculating predicted peculiar velocities from the redshift catalog, projecting those velocities onto the lines of sight for each halo, and then applying equation 4.3 to get a new redshift catalog. At each step, the value of T is increased slightly. This new redshift catalog has different distances ($\mathbf{r}$) for each halo, thus $\mathbf{v}_{\rm pec}(\mathbf{r}_{n-1})$ will be slightly different and need recalculating. At each iteration step, I calculate the slope, $\frac{1}{b_{th}}$, and the scatter by linear regression onto the predicted velocities given the adjusted density field at that iteration step. It is worth noting here that I hold f fixed at its true N-body value when calculating $\mathbf{v}_{pec}$, and use the measured real space value of b_{th} to define the 'stopping point' for T.

I have explored two ways the iterative procedure could introduce systematic error. Since observational experiments determine β by finding which value of $\beta_{transition}$ minimize the fit scatter, a sharply varying or noisy regression (near $T = \frac{1}{b_{th}}$)could cause $\beta_{transition}$ to minimizes at the wrong value. Additionally, the measured slope of the regression fit may differ from $\frac{f}{b_{th}}$ when $T = \frac{1}{b_{th}}$. If the measured 'stopping point' slope systematically differed from $\frac{f}{b_{th}}$, studies which apply this methodology would have to compensate by correcting their measured slope of best agreement.

Motion of Halos During Reconstruction

In this brief aside, I present the radial positions of halos as a function of the iteration steps of the reconstruction. This may help the reader visualize the slow motion of halos from their redshift space positions to their real space positions. In figure 4.15, I introduce the three basic cases which individual galaxies can follow during the reconstruction iterations. All three curves of figure 4.15 were generated by calculating the radial distance from the

origin to the halo in question at each iteration. The horizontal line for each panel shows the real-space location of the halo, for easy visual reference. The red vertical line is included for interest only and indicates which iteration had the smallest squared difference between initial position and calculated position for that iteration summed over all halos[13]. The blue vertical line is at $T = \frac{1}{b_{th}}$ where properly reconstructed halos have returned to their true N-body simulation distances. The iterations extend from $T = 0$ to $T = \frac{1}{b_{th}}$ in 150 steps.

A halo which is distant from any significant neighbors will not move substantially when put into redshift space. For halos which are close to large scale structure, however, peculiar velocities can be significant, and large jumps between real and redshift location can occur. If the shift into redshift space leaves a halo on the correct side of a massive structure, it will follow a curve like the top left panel of figure 4.15, approaching its original position as the iterations increase ('T' increases) and beyond as 'T' exceeds $\frac{f}{b_{th}}$ (where b_{th} is measured using the N-body known distances and the appropriate halo catalog).

If a given halo is close to a very large structure, the gravitational attraction to that deep potential well can accelerate the halo to such high velocities that the halo can appear (in redshift space) to be on the opposite side. For example, a halo between the observer and a large mass is accelerating away from the observer towards the mass, adding additional radial peculiar velocity. When you add that additional peculiar velocity to its real distance, the halo appears more distant than the large mass. The large mass is relatively fixed in redshift space because it is at the bottom of its own potential well (thus not significantly accelerating itself) which permits nearby objects to "overshoot" it. In such a case, where the initial redshift space distortion puts a halo on the "far side" of a larger structure, it will diverge away from the true solution, such as in the second curve of figure 4.15. Unfortunately there is no known way to detect this correction error in real (non-simulated)

[13]It should be noted that this is a halo-by-halo position displacement which is being minimized here. This is substantively different from observational experiment minimization where real space locations are unknown. When finding β, predicted velocities are compared to observed peculiar velocities and the difference between the two are minimized. In that situation, halos of similar mass can switch locations without affecting predictions.

data.

It is also possible to end up in a situation where the iterations are unstable, jumping back and forth between two or more "solutions", as shown in the third curve of figure 4.15. As T gets larger, the areas around massive structures (which cause this unstable jumping) expand. As a result, many halos will move smoothly in T up to a limit and then become unstable.

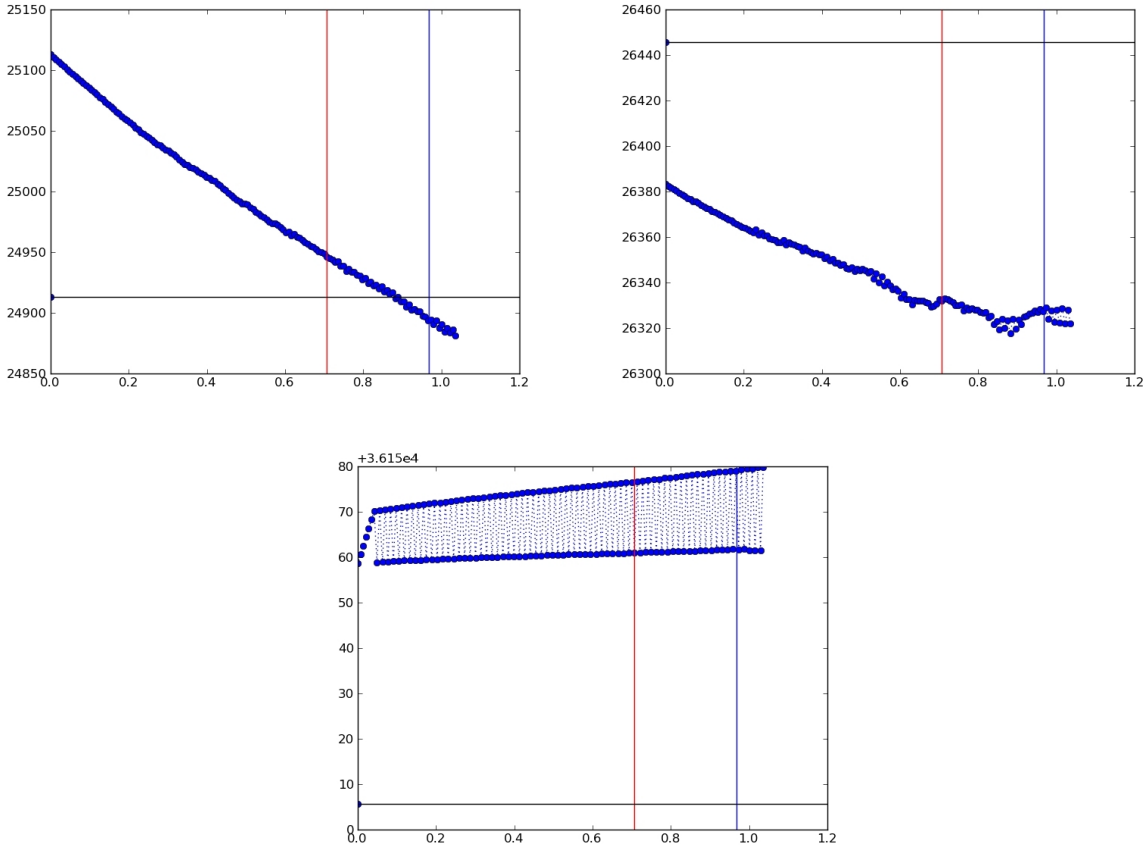

Figure 4.15: Three curves following the radial distance to three different halos during the iteration process. The curves trace the radial distance from the origin to the halo at each iteration. The horizontal line is for easy visual reference; it extends from the real-space location of the halo. The red vertical line shows where the squared difference between initial positions and reconstructed positions summed over all halos is minimal. Note that this is not the "fit" value for the reconstruction since the real reconstruction methods minimize peculiar velocities not distances. The blue vertical line at $T = \frac{1}{b_{th}}$ is the value of T at which, if the reconstruction worked perfectly, each halo would return to its initial position. The iterations extend from $T = 0$ to $T = \frac{1}{b_{th}}$ in 150 steps.

Regression Scatter as a Function of Transition Factor.

In figure 4.16, I present the effect of the transition from redshift space to reconstructed real space on the scatter about the linear regression fit for a density field of all halos over $5.5 \times 10^{10}\ h^{-1}M_{\odot}$ with number weighting. Additionally two lines have been included for clarity: the first vertical line highlighting $T = \frac{1}{b_{th}}$, and the horizontal line that is fixed to the real space value of the scatter. Note that the scatter is still decreasing slowly beyond the final data point, however its rate of decline is quite small and negligible compared to the change in scatter which occurs when $\mathbf{v}(\mathbf{r}, \beta)_{transition}$ is iterated instead of $\mathbf{v}(r, T)_{transition}$, which is what is usually done when β is unknown.

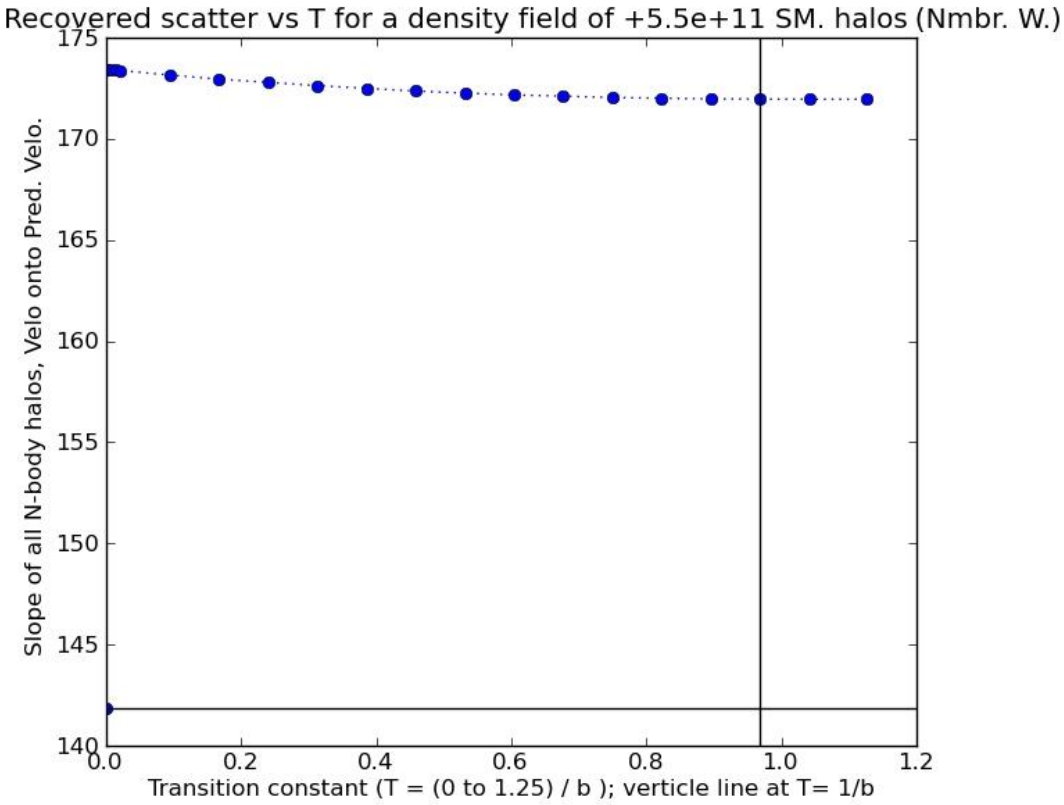

Figure 4.16: Scatter about the linear regression of N-body halo velocities onto predicted velocities, assuming f to be fixed and using all halos ($5.5 \times 10^{11}\ h^{-1} M_{\odot}$) to form the density field (number weighting) as a function of the transition factor T. The horizontal line shows the scatter in real space and the vertical line indicates where $T = \frac{1}{b_{th}}$.

Slope as a Function of Transition Factor.

In figure 4.17, I present the effect of the transition from redshift space to reconstructed real space on the slope from the same iteration process as 4.16. Note that this is a regression of N-body velocity to predicted velocity rather than the position-position comparison of the brief aside in the previous section. Again, two lines have been included for clarity: the first vertical line highlighting $T = \frac{1}{b_{th}}$ and the horizontal line is fixed to the real space

value of the slope. Note that the reconstructed slope differs significantly from its known real space value. This difference corresponds to a real slope to fit slope ratio of 1.07 for halos over $5.5 \times 10^{10}\ h^{-1}M_{\odot}$ with number weighting and 16 steps to the iteration between $T = 0$ and $T = \frac{1}{b_{th}}$. Note however that 20 iterations between $T = 0$ and $T = \frac{1.25}{b}$ were calculated to show the trend beyond the 'stopping point' and that the first three points are sampled closer together than the remaining 17. The necessity of this is explained in the final subsection of this section.

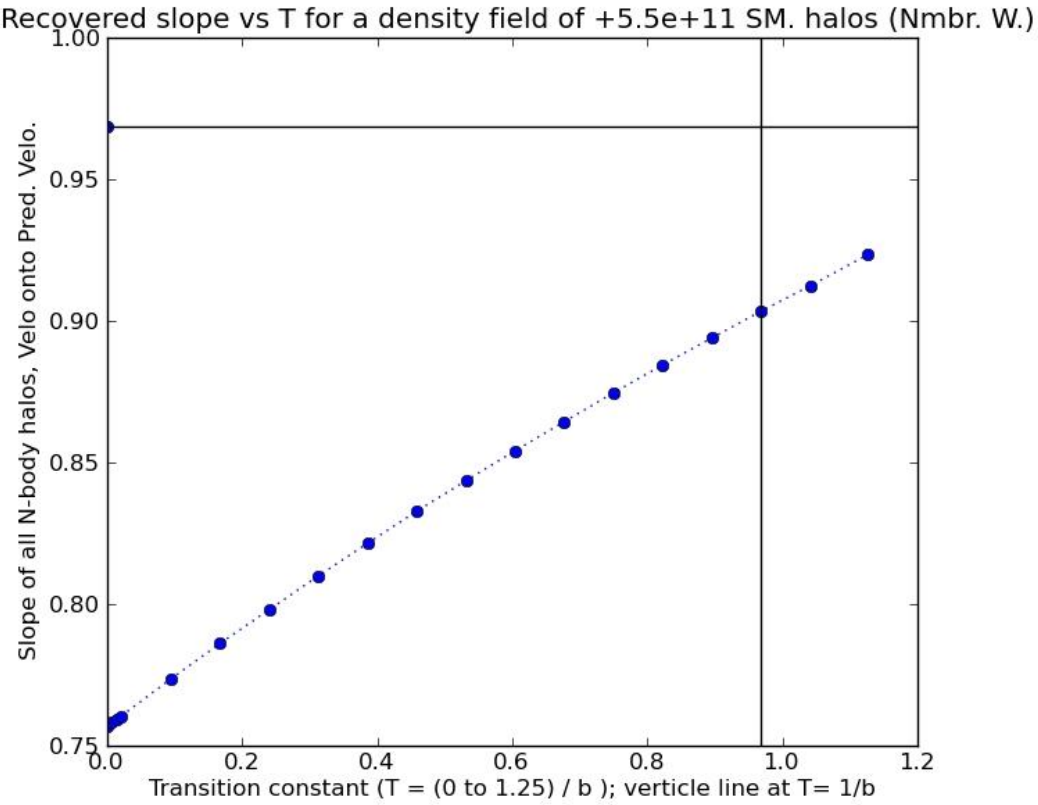

Figure 4.17: Slope of the linear regression of N-body halo velocities onto predicted velocities, assuming f to be fixed and using all halos ($5.5 \times 10^{11}\ h^{-1}M_{\odot}$) to form the density field (number weighting) as a function of the transition factor T. The horizontal line shows the slope in real space and the vertical line indicates where $T = \frac{1}{b_{th}}$.

Table 4.3: Summery of systematic error at different $\mathbb{M}^{\delta}_{\rm TH}$. Note however that most redshift catalogs have a $\mathbb{M}^{\delta}_{\rm TH}$ of between $5.5 \times 10^{11} h^{-1} M_{\odot}$ and $1.0 \times 10^{13} h^{-1} M_{\odot}$

Mass ($h^{-1}M_{\odot}$)	Slope Real	Slope Reconstructed	Ratio
5.5×10^{11}	0.969	0.904	1.07
1.0×10^{12}	0.963	0.900	1.07
5.5×10^{12}	0.738	0.688	1.07
1.0×10^{13}	0.629	0.582	1.08
5.5×10^{13}	0.329	0.293	1.12
1.0×10^{14}	0.222	0.194	1.15

Iteration Regression Slope as a Function of $\mathbb{M}^{\delta}_{\rm TH}$

In table 4.3, I present the results of measuring the bias of the reconstruction method at different values of $\mathbb{M}^{\delta}_{\rm TH}$. The first column is is the mass, the second is the same slopes from table 4.1, the third is the recovered slope at $T = \frac{1}{b_{th}}$, and the final column is the resulting systematic error that must be corrected for in observations reconstructions / measurements of β.

Different Values of 'n'; How Many Steps is Enough?

As with most iterative processes there is the potential for a trade-off between accuracy of the results and the time necessary to calculate the results. One can save time by applying only one step to the iteration by jumping directly from redshift space to 'reconstructed' space in one calculation of predicted velocities. This iterative method was developed because the one step solution was too prone to systematic error. When I initially fit with $n = 16$ I observed a modest drop in the fit slope in the first steps. I ran a second reconstruction of halos over $5.5 \times 10^{11}\ h^{-1} M_{\odot}$ with number weighting using 150 steps between $T = 0$ and $T = 1.05$ [14]. Again the first step decreased the fit slope, but due

[14]The same run was used in the aside segment on the motion of halos during reconstruction

to the smaller step in T the overall decrease was much less significant. If this occurs, the subsequent iterations do not fully correct the overestimated first step decrease and additional systematic error is introduced. In subsequent runs, I reverted to $n = 16$, but with higher sampling frequency at low T to prevent this problem. It is unclear if this is a general feature or an artefact of this realization of N-body simulation[15]. The net effect is that a more coarsely graduated reconstruction can be slightly inaccurate due to an overestimation of the slope decrease from that first step. However after that first step, both curves evolve quite similarly. This indicates that although a coarse reconstruction is acceptable in general, a more fine reconstruction is advised at very low T. In figure 4.18, I show two slope curves as a function of T: on the left is the $n = 16$ curve with the first three points having a smaller step-size than the remaining points, and on the right $n = 150$ and a constant step-size throughout. Even with the first three steps in T reconstructed with a finer resolution, it is notable that the final ratio for the 150 point fit is 1.077, whereas the 16 point reconstruction ratio is 1.072. This slight difference suggests that there may be further room for optimizing the choice of n.

[15]In principle, such a decrease should not occur since the reconstruction pushes all halos out of gravitational wells, thus making the wells more shallow. However, a rapidly varying gravitational field could introduce some artefacts

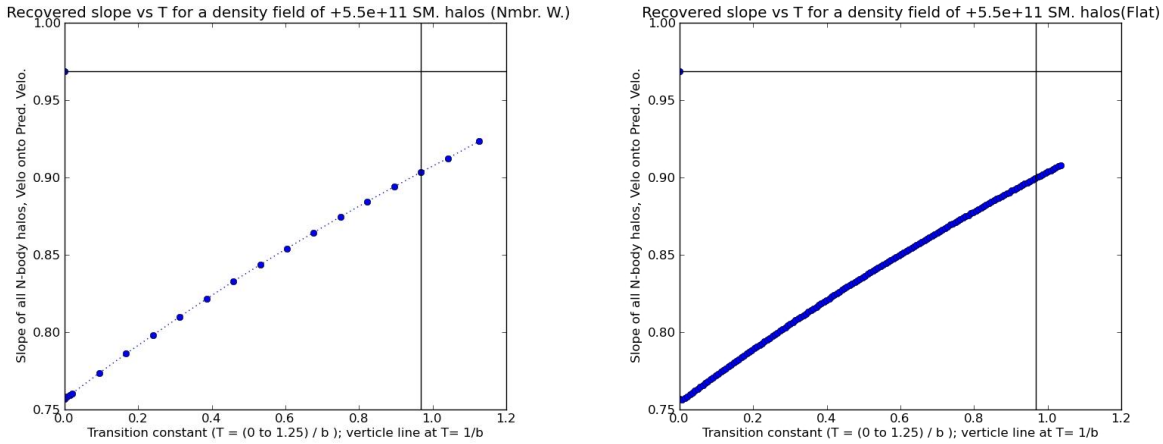

Figure 4.18: A side by-side-comparison of a 16 step reconstruction and a 150 step reconstruction. The resulting reconstruction curves are very similar in part because the 16 step reconstruction has a higher initial sampling density to prevent a low T large slope decrease. However, the final reconstructed b_{th} ratios do differ slightly with the 16 point reconstruction having a final ratio of 1.072 and the 150 step reconstruction having a ratio of 1.077.

4.5 Discussion and Conclusions

The goal of this chapter was to shed light upon the reconstruction process by which redshift space catalogs are converted into proper distance catalogs and to point out where systematic errors could enter into the observational measurements of β (β can be measured by comparing linear theory predictions derived from the proper distance density tracer catalog to observed peculiar velocity tracers). An N-body simulation was used to provide the known distances and peculiar velocities of a particle while a halo catalog was used for reconstructions as the results could be compared to this 'ideal' sample.

With the N-body simulation I have access to a peculiar velocity catalog and a density tracer catalog of equal size; this is not the case in observational measurements. This large

peculiar velocity catalog gave me the opportunity to explore whether there was any systematic error in measuring bias from the peculiar velocity tracers in subsection 4.3.1. I found that there is a slight trend at high and low $\mathbb{M}_{\mathrm{TH}}^{\mathrm{V}}$ towards underestimating the regression slope. At low halo $\mathbb{M}_{\mathrm{TH}}^{\mathrm{V}}$ the systematic slope suppression is likely a by-product of excess noise, as many halos in large structures are physically quite close together but have their velocities randomized by non-linear effects. At high $\mathbb{M}_{\mathrm{TH}}^{\mathrm{V}}$ the systematic slope suppression could be due to slight displacements of the largest halos from the very bottom of their respective potential wells where linear theory is least accurate, thus assigning velocities higher than are seen in more accurate non-linear models. The suppression could also be due to the implicit smoothing associated with large halos, where these large halos are compressed remnants of considerably larger primordial co-moving volumes. If this is the case, then this is simply the reverse effect of smoothing error discussed in the next paragraph (the velocity field is being smoothed, rather than the density field being smoothed).

In 4.3.2, I looked for systematic errors which could be attributed to the effects of smoothing and $\mathbb{M}_{\mathrm{TH}}^{\delta}$. First, I confirmed Berlind *et. al.*'s result on the necessity of carefully choosing smoothing lengths when comparing peculiar velocity predictions to unsmoothed measurements [82]. I concluded that a 4 h^{-1}Mpc Gaussian smoothing kernel is the best size to use to minimize noise and systematic error in linear regressions between N-body results and predicted peculiar velocities. In the following section, I varied $\mathbb{M}_{\mathrm{TH}}^{\delta}$ and was surprised to see the fit bias, slope $= \frac{1}{b_{th}}$, increase faster than expected. From theory, I would expect the b_{th} to be just over 1 at $\mathbb{M}_{\mathrm{TH}}^{\delta} = 10^{13}\ h^{-1}M_{\odot}$ and should not be over 2 until $\mathbb{M}_{\mathrm{TH}}^{\delta}$ exceeds $10^{14}\ h^{-1}M_{\odot}$ [84]. To understand this excess over theory, I recalculated the density fields after artificially reducing their number density. By statistically reducing the data set at each $\mathbb{M}_{\mathrm{TH}}^{\delta}$, I estimated what fraction of the increase in measured bias between two $\mathbb{M}_{\mathrm{TH}}^{\delta}$ was due to changes in spacial number density.

In section 4.4, I focused upon the iterative reconstruction method by converting the N-body observed distances and velocities into a N-body redshift catalog and then applying the reconstruction method to attempt to "return back" to the true distances. Since I am concerned with systematic errors of the methodology, rather than varying β, I introduced a

new factor T which I varied from 1 to $\frac{1}{b_{th}}$. This was to show whether or not the measured scatter and slope are susceptible to systematic error from the reconstruction process, even when β is known.

In conclusion, I found that the scatter around the regression fit (from N-body peculiar velocities onto the step-by-step reconstructed predicted velocities) varied smoothly. In real observational measurements of β, it is important that the scatter from the reconstruction vary smoothly since the scatter in varying T would also be present when varying β directly, If the scatter as a function of T had a strong minimum near $T = \frac{1}{b_{th}}$, then this could lead to systematic inaccuracies. In the T reconstruction, I did find a significant systematic error: the measured value of the linear regression slope was less than $\frac{f}{b_{th}}$ when $T = \frac{1}{b_{th}}$ (the 'stopping point' where the reconstruction is complete). This implies that when $\beta = \frac{f}{b_{th}}$ is measured in real observational experiments the value is being underestimated by 7 (to 15)% by this reconstruction method. This source of systematic error was not taken into account in Chapter 2 when fitting β. Taking it into account would boost the measured value of β by around 7%, depending on the halo mass $\mathbb{M}^{\delta}_{\rm TH}$ of the PSCz catalog.

Chapter 5

Discussion and Conclusion

Each of the central chapters (2, 3, and 4) have discussions and concluding remarks which I will not repeat here. Instead in this brief concluding chapter I will focus on how the results between the chapters are interrelated and what could have been improved in each chapter. I will then outline direct next steps which could follow up on this work, and conclude with prospects for the future of measurements of ΛCDM, gravity, and the growth of structure as illuminated by further studies of peculiar velocities and large scale flows.

5.1 Summary of Overall Results: Interplay Between Chapters

In the first subsection of 4.4.2, I explain how the redshift equation (equation 1.9) can be inverted to reconstruct proper distances to objects in a redshift catalog. This reconstruction process has a free parameter $\beta = \frac{f}{b_{tr}} = \frac{\Omega_m^\gamma \sigma_8}{\sigma_{8,tr}}$ upon which most of this thesis is focused. Three of the four parameters which make up β are fundamental parameters of cosmology (Ω_m, γ, and σ_8; see the introductory section 1.4) and the fourth is a measurable property of the chosen tracer field. It is by this connection to cosmological parameters that redshift

surveys and peculiar velocity measurements (distance indicator surveys) can help form a better understanding of the Universe.

Chapter 4 is dedicated to quantifying the limitations of redshift to real space reconstruction. I applied the processes of reconstruction on an N-body simulation to test for biases and other sources of systematic error. I concluded that the peculiar velocity tracers themselves can introduce some (less than 10%) systematic error as they become more and more associated with larger and larger halos (see 4.3.1). I also found a stronger than anticipated dependency on the halo mass threshold$_{density}$. In eight out of the ten cases where I recalculated the slope with fewer points, the resulting slope was shallower (the measured bias greater) than the higher threshold$_{density}$ result with the same number of data points (see the last subsection of 4.3.2). This strong dependency on the number of halos sampled as density tracers suggests that much of the observed increase in bias from one threshold$_{density}$ level to the next can be attributed to the decrease in the number density of density tracers. It is likely that this amounts to a smoothing problem, where the peculiar velocity tracers are very densely sampled and being compared to a very sparse density field with an average inter-tracer distance considerably larger than the smoothing length. Finally, I also found that the reconstruction method itself fails to properly reconstruct a known β again at the 7-15 % level (see table 4.3 for this bias as a function of mass threshold$_{density}$). The biases uncovered in this section should be taken into account when measuring β using real space reconstruction from redshift catalogs such as was done in Chapter 2. Doing so would raise the measured β.

Chapter 2 was divided into two parts. The first was a direct test of large scale power in ΛCDM, exploiting the fact that peculiar velocities are more sensitive to large scale power than density fluctuations (see 1.4.1 an explanation). Unfortunately for those who might desire to find flaws in ΛCDM, the result was consistent with expectations with a 70 % probability that the data set is consistent with ΛCDM (see 2.4.4). The second component of Chapter 2 was a fit of β which was found to be 0.53 ± 0.08. More importantly, for the work continued in Chapter 3, the $\sigma_{8,tr}$ for the IRAS survey is known, so the β measurement could be converted to a $f\sigma_8$ of 0.424 ± 0.069. For comparisons of these results to other

results in the field, see 2.5.4. Taking into account the results of Chapter 4, the measured value of the residual flow would drop slightly[1] and be in better agreement with ΛCDM. The measured values of $f\sigma_8$ would also increase which would slightly change the results of chapter 3.

In Chapter 3, I combined the $f\sigma_8$ measurement from Chapter 2 with other $f\sigma_8$ measurements at different redshifts to unravel γ from the triple degeneracy. In 1.8, I showed that $f\sigma_8 = \frac{\Omega_m^\gamma \sigma_8}{\sigma_{8,tr}}$. The equality $f \propto \Omega_m^\gamma$ is only an approximation to the growth function of the universe; however, it is very sensitive to deviations from standard gravity and concordance cosmology which makes it an important tool. The results of this fit were consistent with ΛCDM's prediction of $\gamma = 0.55$ with the measured γ being 0.621 ± 0.080. Taking into account the increased value of $f\sigma_8$ due to the results of Chapter 4 would bring the fit results into better agreement with ΛCDM. As discussed in Chapter 4, it is the lowest redshift data points which place the most constraining power on γ. Thus even the slight motion upwards would bring my datum point closer to the 0.55 prediction, and bring it away from the other low-z datum point[5], which would also add more uncertainty in the final result. Both of these changes would cause the overall agreement to improve.

5.2 What Could be Improved on for Future Work

As with any large work there are further steps that may be taken as well as room for improvement. In this section, I shall briefly explore some of these options for my work presented here. I will then touch on the extension of the work to applying the reconstruction code to a real observed data set, thus re-creating a prediction catalog to use with the code developed for Chapter 2.

[1] The residual flow can be thought of as the bulk flow minus an amount calculated with local density $\times$ β, thus a larger β results in less bulk flow to be detected as residual.

5.2.1 Improvements to Chapter 2

In performing the analysis for the bulk flow motions and β measurements, I generated an analysis code capable of handling new data subsets with little additional work. This is important because more and more supernovae data is being collected and new peculiar velocity catalogs will be published. It would be useful to couple that already-prepared software to an online accessible database so that new peculiar velocity catalogs could be remotely uploaded and processed. It would also be useful to extend the current code which only performs maximum likelihood analysis to include the minimum variance weighting and ΛCDM prediction procedures. The code for this exists but was not integrated into the analysis code that I wrote. Finally, now that the systematic error analysis for the redshift-to-real-space reconstruction method has been performed, it would be good to apply what was learned to these measurements by including a redshift catalog in the online database and performing the redshift reconstruction on site rather than using a published reconstruction.

5.2.2 Improvements to Chapter 3

As mentioned in the Statement of Contributions section of the Introduction, Chapter 3 is a segment of a larger published work. The published work fit for γ and also independently fit σ_8 and Ω_m based on the same data set. However, in that paper the σ_8 and Ω_m fits were performed holding γ fixed at 0.55. It is unlikely that a triple free parameter fit would have been significantly constraining on any of the three parameters, however performing such a fit would have been interesting and I would like to attempt it in the future.

5.2.3 Improvements to Chapter 4

The task of identifying all of the possible sources of systematic error for a given procedure is a large one. In Chapter 4, I focused on the more prominent and obvious sources of

systematic errors in the reconstruction method for measuring β. However, with a large N-body simulation there are many additional options that could still be explored. In this section, I will very briefly touch upon some of these options. In all cases, the linear regressions I performed were based on all three velocity components, x y and z, however, in observational data only velocity projections onto the line of sight are measurable. This projection could be a source of error or excess noise. In the shift to redshift space of the N-body catalog, I assumed that the observer was stationary with respect to the CMB, which is not the case for the Local Group. Calculating the velocity of the observer with respect to the CMB at each iteration step and adjusting the redshift catalogs to match would be a simple improvement for the future to further match observational experiments. In the conclusions regarding subsection 4.3.2, I concluded that the high halo mass thresholds$_{density}$ were likely suffering from a smoothing problem due to a mean inter-tracer distance which was larger than the smoothing length. Redoing the analysis with a Gaussian smoothing length that is the larger of 4 h^{-1} Mpc and the mean inter-density tracer distance may partially correct this source of error. The N-body simulation peculiar velocities were known exactly, but this is never the case in observational data (which can be susceptible to Malmquist and similar bias); adding noise to the N-body catalogs would help estimate this source of error. Additionally, the conclusions of chapter 4 were drawn from only one N-body simulation which makes it difficult to assess if any of the observed features were artifacts of this N-body field rather than generally true for all N-body simulations. Here I specifically remind the reader of the slight decrease of $\frac{1}{b_{tr}}$ at low values of T which required the first reconstruction steps to be at a higher frequency. Running multiple N-body simulations, or multiple lines of sight (specifically origins consistent with the Local Group in local density) would allow an assessment of the stability of these observed conclusions.

5.2.4 Application to Real Data

In chapter 2, I used the PSCz density field reconstructed by Branchini et al.[54] as the density field from which peculiar velocities were derived. In testing for sources of systematic

errors of reconstruction methods, I have generated much of the code necessary to perform a real reconstruction on real data. In the near future I would like to apply these methods to the recently released 2M++ catalog [56]. Such a conversion to real data processing would require a significant number of changes to my code and its currently available functionality, however Guilhem Lavaux has already developed a standalone package of codes for doing many of the key conversions and pre-processing that is necessary for working with real data rather than 'perfect' N-body data. I look forward to integrating this existing software into my algorithms and updating my results from Chapters 2 and 3 with a 2M++ reconstructed data field of my own in the near future.

5.3 Future Prospects in the Field of Bulk Flows and Large Scale Structures.

Predicting the future progress in any field is a challenge. There will always be more and better data, such as data from the 6df Galaxy survey [25] (125,000 galaxies, 10,000 Fundamental Plane measurements), the Wallaby survey (600,000 galaxies) [25], the TAIPAN survey (400,000 galaxies) [25], and ongoing SN searches, such as Pan-STARRS, Skymapper, CFA, and several others. All of these surveys combined could contribute as many as an additional 100,000 peculiar velocity measurements and redshift surveys approaching a million objects. Additionally, kinetic Sunyaev−Zel'dovich surveys (which are directly sensitive to peculiar velocities) are improving; G. Lavaux *et. al.* predicts that the next generation of kinetic Sunyaev−Zel'dovich surveys will have sensitivity to bulk flows at the 5.4 σ level[21]. Such a substantial increase over the 1000s of available tracers to analyse today would substantially decrease the stochastic component of the uncertainties budget for measurements of β and related cosmological parameters. In this section, I would like to focus on changes that could occur which would improve how this abundant data is treated.

5.3.1 Improved supernovae

One important benefit would be to find a second feature of Type Ia supernovae that also correlates well with maximum luminosity. Modern SN surveys are now more often multi-spectral, and this additional spectral information, especially for nearby SN for which distances can be determined with other methods, may reveal another calibration parameter (in addition to the light curve decay time, relativistic stretching, and host galaxy reddening). This would reduce the inherent scatter of Type Ia supernovae. Improving the intrinsic scatter is important for Type Ia supernovae distance indicators because the scatter is in magnitudes. This translates to a fixed relative uncertainty on the final measured distance (i. e. the measured distance uncertainty increases linearly with the distance to the supernovae). Such a reduction of inherent scatter would improve resolutions at all depths and push the maximum SN observation depth deeper.

5.3.2 Solving the Triple Value Problem

As mentioned above, one of the larger problems with the reconstruction method is that it is not always possible from redshift information alone to determine which side of a large structure a given observed galaxy is on. However, if a characteristic feature could be identified for observed galaxies behind massive structures rather then in front of them (for example from gravitational lensing or absorption), then that information could be incorporated into the redshift catalogs. A redshift catalog constructed with known ordering of galaxies could significantly improve reconstruction methods.

5.3.3 Improving the Reconstruction Technique

There are also two systematic weaknesses of the reconstruction methodology used in this paper: firstly the assumption of linear bias is likely overly simplified. Halo mass abundance matching algorithms are a good option for adding extra sophistication and accuracy to the

density fields from which the peculiar velocities are derived. Secondly, there are nonlinear reconstruction techniques, such as the Lagrangian approach pioneered in part by [85–87] that is currently being worked on by Lavaux and many others.

References

[1] D. Larson, J. Dunkley, G. Hinshaw, E. Komatsu, M. R. Nolta, C. L. Bennett, B. Gold, M. Halpern, R. S. Hill, N. Jarosik, A. Kogut, M. Limon, S. S. Meyer, N. Odegard, L. Page, K. M. Smith, D. N. Spergel, G. S. Tucker, J. L. Weiland, E. Wollack, and E. L. Wright. Seven-year Wilkinson Microwave Anisotropy Probe (WMAP) Observations: Power Spectra and WMAP-derived Parameters. *ApJ Supp*, 192:16–+, feb 2011.

[2] Malcolm Hicken, W. Michael Wood-Vasey, Stephane Blondin, Peter Challis, Saurabh Jha, Patrick L. Kelly, Armin Rest, and Robert P. Kirshner. Improved dark energy constraints from 100 new cfa supernova type ia light curves. *ApJ*, 700(2):1097, 2009.

[3] R. Watkins, H. A. Feldman, and M. J. Hudson. Consistently large cosmic flows on scales of $100h^{-1}$Mpc: a challenge for the standard ΛCDM cosmology. *MNRAS*, 392:743–756, jan 2009.

[4] A. Kashlinsky, F. Atrio-Barandela, H. Ebeling, A. Edge, and D. Kocevski. A New Measurement of the Bulk Flow of X-Ray Luminous Clusters of Galaxies. *ApJL*, 712:L81–L85, mar 2010.

[5] M. Davis, A. Nusser, K. L. Masters, C. Springob, J. P. Huchra, and G. Lemson. Local gravity versus local velocity: solutions for β and non-linear bias. *MNRAS*, 413:2906–2922, jun 2011.

[6] S. G. Patiri, J. Betancort-Rijo, and F. Prada. On an analytical framework for voids:

their abundances, density profiles and local mass functions. *MNRAS*, 368:1132–1144, May 2006.

[7] F. Zwicky. On the Masses of Nebulae and of Clusters of Nebulae. *ApJ*, 86:217, October 1937.

[8] J. Dunkley, E. Komatsu, M. R. Nolta, D. N. Spergel, D. Larson, G. Hinshaw, L. Page, C. L. Bennett, B. Gold, N. Jarosik, J. L. Weiland, M. Halpern, R. S. Hill, A. Kogut, M. Limon, S. S. Meyer, G. S. Tucker, E. Wollack, and E. L. Wright. Five-Year Wilkinson Microwave Anisotropy Probe (WMAP) Observations: Likelihoods and Parameters from the WMAP data. *ArXiv e-prints*, 803, mar 2008.

[9] J. H. Oort. Some Problems Concerning the Structure and Dynamics of the Galactic System and the Elliptical Nebulae NGC 3115 and 4494. *ApJ*, 91:273, April 1940.

[10] M. S. Roberts. A High-Resolution 21-CM Hydrogen-Line Survey of the Andromeda Nebula. *ApJ*, 144:639, May 1966.

[11] M. S. Roberts and A. H. Rots. Comparison of Rotation Curves of Different Galaxy Types. *A&A*, 26:483–485, August 1973.

[12] V. C. Rubin, W. K. J. Ford, and N. . Thonnard. Rotational properties of 21 SC galaxies with a large range of luminosities and radii, from NGC 4605 /R = 4kpc/ to UGC 2885 /R = 122 kpc/. *ApJ*, 238:471–487, June 1980.

[13] P. Fischer and J. A. Tyson. The Mass Distribution of the Most Luminous X-Ray Cluster RXJ 1347.5-1145 From Gravitational Lensing. *AJ*, 114:14–24, July 1997.

[14] P. Fischer, G. Bernstein, G. Rhee, and J. A. Tyson. The Mass Distribution of the Cluster 0957+561 From Gravitational Lensing. *AJ*, 113:521, February 1997.

[15] N. Kaiser. Clustering in real space and in redshift space. *MNRAS*, 227:1–21, jul 1987.

[16] A. G. Riess, A. V. Filippenko, P. Challis, A. Clocchiatti, A. Diercks, P. M. Garnavich, R. L. Gilliland, C. J. Hogan, S. Jha, R. P. Kirshner, B. Leibundgut, M. M. Phillips, D. Reiss, B. P. Schmidt, R. A. Schommer, R. C. Smith, J. Spyromilio, C. Stubbs, N. B. Suntzeff, and J. Tonry. Observational Evidence from Supernovae for an Accelerating Universe and a Cosmological Constant. *AJ*, 116:1009–1038, September 1998.

[17] E. V. Linder. Cosmic growth history and expansion history. *Phys Rev D*, 72(4):043529, aug 2005.

[18] Barbara Ryden. *Introduction to Cosmology*. Addison-Wesley, 2003.

[19] G. Folatelli, M. M. Phillips, C. R. Burns, C. Contreras, M. Hamuy, W. L. Freedman, S. E. Persson, M. Stritzinger, N. B. Suntzeff, K. Krisciunas, L. Boldt, S. González, W. Krzeminski, N. Morrell, M. Roth, F. Salgado, B. F. Madore, D. Murphy, P. Wyatt, W. Li, A. V. Filippenko, and N. Miller. The Carnegie Supernova Project: Analysis of the First Sample of Low-Redshift Type-Ia Supernovae. *AJ*, 139:120–144, jan 2010.

[20] M. A. Strauss and J. A. Willick. The density and peculiar velocity fields of nearby galaxies. *Physics Reports*, 261:271–431, 1995.

[21] G. Lavaux, N. Afshordi, and M. J. Hudson. First measurement of the bulk flow of nearby galaxies using the cosmic microwave background. *ArXiv e-prints*, July 2012.

[22] H. A. Feldman, R. Watkins, and M. J. Hudson. Cosmic flows on 100 h^{-1} Mpc scales: standardized minimum variance bulk flow, shear and octupole moments. *MNRAS*, 407:2328, jul 2010.

[23] H. Wang, H. J. Mo, X. Yang, and F. C. van den Bosch. Reconstructing the cosmic velocity and tidal fields with galaxy groups selected from the Sloan Digital Sky Survey. *MNRAS*, 420:1809–1824, February 2012.

[24] D.-C. Dai, W. H. Kinney, and D. Stojkovic. Measuring the cosmological bulk flow using the peculiar velocities of supernovae. *JCAP*, 4:15–+, apr 2011.

[25] F. Beutler, C. Blake, M. Colless, D. H. Jones, L. Staveley-Smith, G. B. Poole, L. Campbell, Q. Parker, W. Saunders, and F. Watson. The 6dF Galaxy Survey: z \approx 0 measurement of the growth rate and sigma_8. *ArXiv e-prints*, apr 2012.

[26] F. Y. Wang. Current constraints on early dark energy and growth index using latest observations. *A&A*, 543:A91, July 2012.

[27] L. Samushia, B. A. Reid, M. White, W. J. Percival, A. J. Cuesta, L. Lombriser, M. Manera, R. C. Nichol, D. P. Schneider, D. Bizyaev, H. Brewington, E. Malanushenko, V. Malanushenko, D. Oravetz, K. Pan, A. Simmons, A. Shelden, S. Snedden, J. L. Tinker, B. A. Weaver, D. G. York, and G.-B. Zhao. The Clustering of Galaxies in the SDSS-III DR9 Baryon Oscillation Spectroscopic Survey: Testing Deviations from Λ and General Relativity using anisotropic clustering of galaxies. *ArXiv e-prints*, June 2012.

[28] D. Rapetti, C. Blake, S. W. Allen, A. Mantz, D. Parkinson, and F. Beutler. A combined measurement of cosmic growth and expansion from clusters of galaxies, the CMB and galaxy clustering. *ArXiv e-prints*, May 2012.

[29] S. Basilakos. The ΛCDM growth rate of structure revisited. *ArXiv e-prints*, February 2012.

[30] S. J. Turnbull, M. J. Hudson, H. A. Feldman, M. Hicken, R. P. Kirshner, and R. Watkins. Cosmic flows in the nearby universe from Type Ia supernovae. *MNRAS*, 420:447–454, feb 2012.

[31] M. J. Hudson and S. J. Turnbull. The Growth Rate of Cosmic Structure from Peculiar Velocities at Low and High Redshifts. *ApJL*, 751:L30, June 2012.

[32] P. J. E. Peebles. *Principles of Physical Cosmology*. Princeton University Press, 1993.

[33] R. Juszkiewicz, N. Vittorio, and R. F. G. Wyse. Local gravity and large-scale structure. *ApJ*, 349:408–414, feb 1990.

[34] A. Kogut, C. Lineweaver, G. F. Smoot, C. L. Bennett, A. Banday, N. W. Boggess, E. S. Cheng, G. de Amici, D. J. Fixsen, G. Hinshaw, P. D. Jackson, M. Janssen, P. Keegstra, K. Loewenstein, P. Lubin, J. C. Mather, L. Tenorio, R. Weiss, D. T. Wilkinson, and E. L. Wright. Dipole Anisotropy in the COBE Differential Microwave Radiometers First-Year Sky Maps. *ApJ*, 419:1–+, dec 1993.

[35] M. Rowan-Robinson, J. Sharpe, S. J. Oliver, O. Keeble, A. Canavezes, W. Saunders, A. N. Taylor, H. Valentine, C. S. Frenk, G. P. Efstathiou, R. G. McMahon, S. D. M. White, W. Sutherland, H. Tadros, and S. Maddox. The IRAS PSCz dipole. *MNRAS*, 314:375–397, may 2000.

[36] W. Saunders, W. J. Sutherland, S. J. Maddox, O. Keeble, S. J. Oliver, M. Rowan-Robinson, R. G. McMahon, G. P. Efstathiou, H. Tadros, S. D. M. White, C. S. Frenk, A. Carramiñana, and M. R. S. Hawkins. The PSCz catalogue. *MNRAS*, 317:55–64, sep 2000.

[37] S. Basilakos and M. Plionis. The PSCz dipole revisited. *MNRAS*, 373:1112–1116, dec 2006.

[38] J. P. Huchra, L. M. Macri, K. L. Masters, T. H. Jarrett, P. Berlind, M. Calkins, A. C. Crook, R. Cutri, P. Erdoğdu, E. Falco, T. George, C. M. Hutcheson, O. Lahav, J. Mader, J. D. Mink, N. Martimbeau, S. Schneider, M. Skrutskie, S. Tokarz, and M. Westover. The 2MASS Redshift Survey −− Description and Data Release. *ApJ Supp*, 199:26, apr 2012.

[39] P. Erdoğdu, J. P. Huchra, O. Lahav, M. Colless, R. M. Cutri, E. Falco, T. George, T. Jarrett, D. H. Jones, C. S. Kochanek, L. Macri, J. Mader, N. Martimbeau, M. Pahre, Q. Parker, A. Rassat, and W. Saunders. The dipole anisotropy of the 2 Micron All-Sky Redshift Survey. *MNRAS*, 368:1515–1526, jun 2006.

[40] G. Lavaux, R. B. Tully, R. Mohayaee, and S. Colombi. Cosmic Flow From Two

Micron All-Sky Redshift Survey: the Origin of Cosmic Microwave Background Dipole and Implications for ΛCDM Cosmology. *ApJ*, 709:483–498, jan 2010.

[41] Maciej Bilicki, Michal Chodorowski, Gary A. Mamon, and Thomas Jarrett. Is the 2MASS clustering dipole convergent? *ApJ*, 741:31, feb 2011.

[42] A. G. Riess, W. H. Press, and R. P. Kirshner. Determining the motion of the local group using type IA supernovae light curve shapes. *ApJL*, 445:L91–L94, jun 1995.

[43] A. G. Riess, M. Davis, J. Baker, and R. P. Kirshner. The Velocity Field from Type IA Supernovae Matches the Gravity Field from Galaxy Surveys. *ApJL*, 488:L1+, oct 1997.

[44] D. J. Radburn-Smith, J. R. Lucey, and M. J. Hudson. A comparison of local Type Ia supernovae with the IRAS PSCz gravity field. *MNRAS*, 355:1378, 11 2004.

[45] R. W. Pike and M. J. Hudson. Cosmological Parameters from the Comparison of the 2MASS Gravity Field with Peculiar Velocity Surveys. *ApJ*, 635:11–21, dec 2005.

[46] J. Lucey, D. Radburn-Smith, and M. Hudson. Beta, Local SNIa data and the Great Attractor. In *ASP Conf. Ser. 329: Nearby Large-Scale Structures and the Zone of Avoidance*, pages 21–26, jan 2005.

[47] T. Haugboelle, S. Hannestad, B. Thomsen, J. Fynbo, J. Sollerman, and S. Jha. The Velocity Field of the Local Universe from Measurements of Type Ia Supernovae. *ArXiv Astrophysics e-prints*, dec 2006.

[48] J. Colin, R. Mohayaee, S. Sarkar, and A. Shafieloo. Probing the anisotropic local Universe and beyond with SNe Ia data. *MNRAS*, 414:264–271, jun 2011.

[49] A. Weyant, M. Wood-Vasey, L. Wasserman, and P. Freeman. An Unbiased Method of Modeling the Local Peculiar Velocity Field with Type Ia Supernovae. *ApJ*, 732:65–+, may 2011.

[50] Saurabh Jha, Adam G. Riess, and Robert P. Kirshner. Improved distances to type ia supernovae with multicolor light curve shapes: Mlcs2k2. *ApJ*, 659:122–148, 2007.

[51] R. Amanullah, C. Lidman, D. Rubin, G. Aldering, P. Astier, K. Barbary, M. S. Burns, A. Conley, K. S. Dawson, S. E. Deustua, M. Doi, S. Fabbro, L. Faccioli, H. K. Fakhouri, G. Folatelli, A. S. Fruchter, H. Furusawa, G. Garavini, G. Goldhaber, A. Goobar, D. E. Groom, I. Hook, D. A. Howell, N. Kashikawa, A. G. Kim, R. A. Knop, M. Kowalski, E. Linder, J. Meyers, T. Morokuma, S. Nobili, J. Nordin, P. E. Nugent, L. Östman, R. Pain, N. Panagia, S. Perlmutter, J. Raux, P. Ruiz-Lapuente, A. L. Spadafora, M. Strovink, N. Suzuki, L. Wang, W. M. Wood-Vasey, N. Yasuda, and T. Supernova Cosmology Project. Spectra and Hubble Space Telescope Light Curves of Six Type Ia Supernovae at $0.511 < z < 1.12$ and the Union2 Compilation. *ApJ*, 716:712–738, jun 2010.

[52] T. R. Lauer and M. Postman. The motion of the Local Group with respect to the 15,000 kilometer per second Abell cluster inertial frame. *ApJ*, 425:418–438, apr 1994.

[53] J. L. Tonry, B. P. Schmidt, B. Barris, P. Candia, P. Challis, A. Clocchiatti, A. L. Coil, A. V. Filippenko, P. Garnavich, C. Hogan, S. T. Holland, S. Jha, R. P. Kirshner, K. Krisciunas, B. Leibundgut, W. Li, T. Matheson, M. M. Phillips, A. G. Riess, R. Schommer, R. C. Smith, J. Sollerman, J. Spyromilio, C. W. Stubbs, and N. B. Suntzeff. Cosmological Results from High-z Supernovae. *ApJ*, 594:1–24, sep 2003.

[54] E. Branchini, L. Teodoro, C. S. Frenk, I. Schmoldt, G. Efstathiou, S. D. M. White, W. Saunders, W. Sutherland, M. Rowan-Robinson, O. Keeble, H. Tadros, S. Maddox, and S. Oliver. A non-parametric model for the cosmic velocity field. *MNRAS*, 308:1–28, sep 1999.

[55] M. J. Hudson, R. J. Smith, J. R. Lucey, and E. Branchini. Streaming motions of galaxy clusters within 12 000 km s^{-1} – V. The peculiar velocity field. *MNRAS*, 352:61–75, jul 2004.

[56] G. Lavaux and M. J. Hudson. The 2M++ galaxy redshift catalogue. *MNRAS*, 416:2840–2856, oct 2011.

[57] D. H. Jones, M. A. Read, W. Saunders, M. Colless, T. Jarrett, Q. A. Parker, A. P. Fairall, T. Mauch, E. M. Sadler, F. G. Watson, D. Burton, L. A. Campbell, P. Cass, S. M. Croom, J. Dawe, K. Fiegert, L. Frankcombe, M. Hartley, J. Huchra, D. James, E. Kirby, O. Lahav, J. Lucey, G. A. Mamon, L. Moore, B. A. Peterson, S. Prior, D. Proust, K. Russell, V. Safouris, K.-I. Wakamatsu, E. Westra, and M. Williams. The 6dF Galaxy Survey: final redshift release (DR3) and southern large-scale structures. *MNRAS*, 399:683–698, oct 2009.

[58] A. J. S. Hamilton and M. Tegmark. The real-space power spectrum of the PSCz survey from 0.01 to 300h Mpc^{-1} . *MNRAS*, 330:506–530, mar 2002.

[59] R. Juszkiewicz, H. A. Feldman, J. N. Fry, and A. H. Jaffe. Weakly nonlinear dynamics and the σ_8 parameter. *JCAP*, 2:21–+, feb 2010.

[60] M. S. Turner. Tilted Universe and other remnants of the preinflationary Universe. *Phys Rev D*, 44:3737–3748, dec 1991.

[61] A. Kashlinsky, F. Atrio-Barandela, D. Kocevski, and H. Ebeling. A Measurement of Large-Scale Peculiar Velocities of Clusters of Galaxies: Results and Cosmological Implications. *ApJL*, 686:L49–L52, oct 2008.

[62] Y.-Z. Ma, C. Gordon, and H. A. Feldman. Peculiar velocity field: Constraining the tilt of the Universe. *Phys Rev D*, 83(10):103002–+, may 2011.

[63] Mohan Ganeshalingam, Weidong Li, and Alexei V. Filippenko. The Rise-Time Distribution of Nearby Type Ia Supernovae. *ArXiv e-prints*, jul 2011.

[64] N. M. Law, S. R. Kulkarni, R. G. Dekany, E. O. Ofek, R. M. Quimby, P. E. Nugent, J. Surace, C. C. Grillmair, J. S. Bloom, M. M. Kasliwal, L. Bildsten, T. Brown, S. B. Cenko, D. Ciardi, E. Croner, S. G. Djorgovski, J. van Eyken, A. V. Filippenko, D. B.

Fox, A. Gal-Yam, D. Hale, N. Hamam, G. Helou, J. Henning, D. A. Howell, J. Jacobsen, R. Laher, S. Mattingly, D. McKenna, A. Pickles, D. Poznanski, G. Rahmer, A. Rau, W. Rosing, M. Shara, R. Smith, D. Starr, M. Sullivan, V. Velur, R. Walters, and J. Zolkower. The Palomar Transient Factory: System Overview, Performance, and First Results. *PASP*, 121:1395–1408, dec 2009.

[65] M. Stritzinger, M. M. Phillips, L. Boldt S., C. Burns, A. Campillay, C. Contreras, S. Gonzalez, G. Folatelli, N. Morrell, W. Krzeminski, M. Roth, F. Salgado, D. L. Depoy, M. Hamuy, W. L. Freedman, B. Madore, J. L. Marshall, S. E. Persson, J.-P. Rheault, N. Suntzeff, S. Villanueva, W. Li, and A. V. Filippenko. The Carnegie Supernova Project: Second Photometry Data Release of Low-Redshift Type Ia Supernovae. *ArXiv e-prints*, aug 2011.

[66] S. C. Keller, B. P. Schmidt, M. S. Bessell, P. G. Conroy, P. Francis, A. Granlund, E. Kowald, A. P. Oates, T. Martin-Jones, T. Preston, P. Tisserand, A. Vaccarella, and M. F. Waterson. The SkyMapper Telescope and The Southern Sky Survey. *Publications of the Astronomical Society of Australia*, 24:1–12, may 2007.

[67] H. A. Feldman and R. Watkins. Bulk flow and shear moments of the SFI++ survey. *MNRAS*, 387:825–829, jun 2008.

[68] R. J. Smith, M. J. Hudson, J. R. Lucey, J. E. Nelan, and G. A. Wegner. The NOAO Fundamental Plane Survey - III. Variations in the stellar populations of red-sequence galaxies from the cluster core to the virial radius. *MNRAS*, 369:1419–1436, jul 2006.

[69] D. H. Jones, W. Saunders, M. Colless, M. A. Read, Q. A. Parker, F. G. Watson, L. A. Campbell, D. Burkey, T. Mauch, L. Moore, M. Hartley, P. Cass, D. James, K. Russell, K. Fiegert, J. Dawe, J. Huchra, T. Jarrett, O. Lahav, J. Lucey, G. A. Mamon, D. Proust, E. M. Sadler, and K.-i. Wakamatsu. The 6dF Galaxy Survey: samples, observational techniques and the first data release. *MNRAS*, 355:747–763, dec 2004.

[70] E. Komatsu, K. M. Smith, J. Dunkley, C. L. Bennett, B. Gold, G. Hinshaw, N. Jarosik, D. Larson, M. R. Nolta, L. Page, D. N. Spergel, M. Halpern, R. S. Hill, A. Kogut, M. Limon, S. S. Meyer, N. Odegard, G. S. Tucker, J. L. Weiland, E. Wollack, and E. L. Wright. Seven-year Wilkinson Microwave Anisotropy Probe (WMAP) Observations: Cosmological Interpretation. *ApJ Supp*, 192:18, feb 2011.

[71] L. Wang and P. J. Steinhardt. Cluster Abundance Constraints for Cosmological Models with a Time-varying, Spatially Inhomogeneous Energy Component with Negative Pressure. *ApJ*, 508:483–490, dec 1998.

[72] G. Dvali, G. Gabadadze, and M. Porrati. 4D gravity on a brane in 5D Minkowski space. *Physics Letters B*, 485:208–214, jul 2000.

[73] E. V. Linder and R. N. Cahn. Parameterized beyond-Einstein growth. *Astroparticle Physics*, 28:481–488, dec 2007.

[74] L. Guzzo, M. Pierleoni, B. Meneux, E. Branchini, O. Le Fèvre, C. Marinoni, B. Garilli, J. Blaizot, G. De Lucia, A. Pollo, H. J. McCracken, D. Bottini, V. Le Brun, D. Maccagni, J. P. Picat, R. Scaramella, M. Scodeggio, L. Tresse, G. Vettolani, A. Zanichelli, C. Adami, S. Arnouts, S. Bardelli, M. Bolzonella, A. Bongiorno, A. Cappi, S. Charlot, P. Ciliegi, T. Contini, O. Cucciati, S. de la Torre, K. Dolag, S. Foucaud, P. Franzetti, I. Gavignaud, O. Ilbert, A. Iovino, F. Lamareille, B. Marano, A. Mazure, P. Memeo, R. Merighi, L. Moscardini, S. Paltani, R. Pellò, E. Perez-Montero, L. Pozzetti, M. Radovich, D. Vergani, G. Zamorani, and E. Zucca. A test of the nature of cosmic acceleration using galaxy redshift distortions. *Nature*, 451:541–544, jan 2008.

[75] A. Kosowsky and S. Bhattacharya. A future test of gravitation using galaxy cluster velocities. *Phys Rev D*, 80(6):062003, sep 2009.

[76] Y.-S. Song and W. J. Percival. Reconstructing the history of structure formation using redshift distortions. *JCAP*, 10:4–+, oct 2009.

[77] C. Blake, S. Brough, M. Colless, C. Contreras, W. Couch, S. Croom, T. Davis, M. J. Drinkwater, K. Forster, D. Gilbank, M. Gladders, K. Glazebrook, B. Jelliffe, R. J. Jurek, I.-H. Li, B. Madore, D. C. Martin, K. Pimbblet, G. B. Poole, M. Pracy, R. Sharp, E. Wisnioski, D. Woods, T. K. Wyder, and H. K. C. Yee. The WiggleZ Dark Energy Survey: the growth rate of cosmic structure since redshift z=0.9. *MNRAS*, 415:2876–2891, aug 2011.

[78] L. Samushia, W. J. Percival, and A. Raccanelli. Interpreting large-scale redshift-space distortion measurements. *MNRAS*, 420:2102–2119, mar 2012.

[79] C. Blake, K. Glazebrook, T. M. Davis, S. Brough, M. Colless, C. Contreras, W. Couch, S. Croom, M. J. Drinkwater, K. Forster, D. Gilbank, M. Gladders, B. Jelliffe, R. J. Jurek, I.-H. Li, B. Madore, D. C. Martin, K. Pimbblet, G. B. Poole, M. Pracy, R. Sharp, E. Wisnioski, D. Woods, T. K. Wyder, and H. K. C. Yee. The WiggleZ Dark Energy Survey: measuring the cosmic expansion history using the Alcock-Paczynski test and distant supernovae. *MNRAS*, 418:1725–1735, dec 2011.

[80] Timothy Clifton, Pedro G. Ferreira, Antonio Padilla, and Constantinos Skordis. Modified Gravity and Cosmology. *Phys. Rept.*, 513:1–189, jun 2012.

[81] M. Davis, M. A. Strauss, and A. Yahil. A redshift survey of IRAS galaxies. III - Reconstruction of the velocity and density fields in N-body model universes. *ApJ*, 372:394–409, may 1991.

[82] A. A. Berlind, V. K. Narayanan, and D. H. Weinberg. Biased Estimates of Ω_m from Comparing Smoothed Predicted Velocity Fields to Unsmoothed Peculiar-Velocity Measurements. *ApJ*, 537:537–541, jul 2000.

[83] A. Yahil, M. A. Strauss, M. Davis, and J. P. Huchra. A redshift survey of IRAS galaxies. II - Methods for determining self-consistent velocity and density fields. *ApJ*, 372:380–393, may 1991.

[84] W. Hu and A. V. Kravtsov. Sample Variance Considerations for Cluster Surveys. *ApJ*, 584:702–715, February 2003.

[85] P. J. E. Peebles. Tracing galaxy orbits back in time. *ApJL*, 344:L53–L56, September 1989.

[86] E. J. Shaya, P. J. E. Peebles, and R. B. Tully. Action Principle Solutions for Galaxy Motions within 3000 Kilometers per Second. *ApJ*, 454:15, November 1995.

[87] A. Nusser and E. Branchini. On the least action principle in cosmology. *MNRAS*, 313:587–595, apr 2000.